High-Temperature Oxidation of Steels Investigating the Kinetics of High-Temperature Oxidation of Steels Through Experimental, Numerical, and Data-Driven Approaches

Aghaeian, S.

DOI
10.4233/uuid:e5b2f672-9dd2-498f-828f-f587b509e298

Publication date
2024

Document Version
Final published version

Citation (APA)
Aghaeian, S. (2024). *High-Temperature Oxidation of Steels Investigating the Kinetics of High-Temperature Oxidation of Steels Through Experimental, Numerical, and Data-Driven Approaches*. [Dissertation (TU Delft), Delft University of Technology]. https://doi.org/10.4233/uuid:e5b2f672-9dd2-498f-828f-f587b509e298

High-Temperature Oxidation of Steels

Investigating the Kinetics of High-Temperature Oxidation of Steels Through Experimental, Numerical, and Data-Driven Approaches

High-Temperature Oxidation of Steels

Investigating the Kinetics of High-Temperature Oxidation of Steels Through Experimental, Numerical, and Data-Driven Approaches

Dissertation

for the purpose of obtaining the degree of doctor
at Delft University of Technology,
by the authority of the Rector Magnificus Prof. dr. ir. T.H.J.J. van der Hagen,
chair of the board for doctorates,
to be defended publicly on
Tuesday 19th of March 2024 at 12:30

by

Soroush AGHAEIAN

Master of Science in Materials Engineering,
Sharif University of Technology, Tehran, Iran
born in Shahrood, Iran

This dissertation has been approved by the promotors

Composition of the doctoral committee:

Rector Magnificus,	chairperson
Dr. A. J. Böttger,	Delft University of Technology, promotor
Prof. dr. ir. J.M.C. Mol	Delft University of Technology, promotor
Dr. W. Melfo	Tata Steel IJmuuiden
Independent members:	
Prof. dr. ir. J. Sietsma	Delft University of Technology
Prof. dr. ir. R. Benedictus	Delft University of Technology
Prof. dr. ir. B.J. Kooi	University of Groningen
Dr. M. Auinger	University of Warwick
Other members:	
Prof. dr. M.J. Santofimia Navarro	Delft University of Technology, reserve member

Keywords: High-Temperature Oxidation, Diffusion-Based Models, Oxidation Kinetics, Machine Learning Models, Oxidation of Steels

Printed by: Ridderprint | www.ridderprint.nl

Cover by: D.C. van Dolderen and T. Komlóssy

Photo by: A. Shirazi

ISBN 978-94-6483-837-4

An electronic version of this dissertation is available at
http://repository.tudelft.nl

"Make thyself pure from the attributes of self, that thou mayst behold thine own pure untarnished essence."

Rumi

To all my lovely families...

Contents

Summary

High-temperature (HT) oxidation plays a significant role in various stages of the steelmaking process, including hot rolling. When exposed to high temperatures and oxygen partial pressure, the steel composition near the surface can be altered as alloying elements deplete. Additionally, the characteristics of the oxide scale, such as thickness and phase composition, vary depending on the oxidation conditions. Due to the experimental challenges of studying such rapid processes under extreme conditions, predictive models are necessary to estimate the substrate surface and oxide scale composition as well as the general oxidation rate of the alloy.

Chapter 1 serves as a general introduction to the high-temperature oxidation of metals, highlighting its significance, and includes an outline of the thesis.

Chapter 2 entails a background chapter focused on predictive models for HT oxidation in steels and iron-based alloys. It presents the classic models proposed by Carl Wagner and highlights the key advancements derived from his theories. These models were primarily utilized to examine various aspects of HT oxidation, such as oxidation modes, oxidation rate, oxide composition, and changes in the substrate alloy composition, with a focus on pure metals and simple binary alloys. The chapter then presents the limitations of diffusion-based models and proceeds to discuss the subsequent generation of HT oxidation studies, incorporating data-driven methodologies. It demonstrates the capability of various Machine Learning (ML) algorithms, including KNN, ANN, RF, and others, to predict the growth rate of oxides during HT oxidation in different alloy compositions.

In **Chapter 3**, we conducted comprehensive high-temperature oxidation experiments on iron binary alloys with varying Mn content, relevant to Advanced High Strength Steels (AHSS), employing a Thermogravimetric analyzer (TGA). Oxidation kinetics showed an initial linear growth rate under most conditions, transitioning to parabolic growth only in specific scenarios. Notably, the research revealed that oxygen partial pressure and gas linear flow rate were the primary factors affecting oxidation kinetics, with temperature and Mn content exhibiting minimal influence. An activation energy of around 2 $kJ \cdot mol^{-1}$ was obtained from the experiments. In addition to the kinetics, a detailed analysis of the oxide scale, facilitated by SEM, EDS, XRD, and in-situ XRD techniques, unveiled the oxidation mechanism to be gas-phase mass transfer through a laminar boundary layer, leading to variations in scale thickness along the sample's length. The experimental results presented in this chapter served as the basis for developing the predictive model described in **Chapter 4**.

In **Chapter 4**, a diffusion-based model is developed to simulate the HT oxidation process of Fe-Mn alloys. The model accounts for both the chemical composition of the oxide scale and the depletion of Mn in the substrate alloy. The

input required for this model is the growth rate constants of the oxide scale. To obtain these constants, a series of HT oxidation experiments using a TGA were conducted. During these experiments, iron-manganese alloys were exposed to gas mixtures with varying oxygen partial pressures (10-30 kPa) and gas flow rates (26.6 to 250 mL min^{-1}) at different temperatures (950-1150 °C). It is observed that temperature variations play a pivotal role, influencing the composition profile of Mn within the alloys during oxidation. Additionally, increased oxygen partial pressure within the oxidizing gas mixture results in faster linear growth of the oxide scale, predominantly composed of iron oxide (FeO) and manganese oxide (MnO). This accelerated oxidation process leads to a higher O/M recession and, consequently, a thinner Mn depleted zone. Finally, the study introduces numerical simulations capable of predicting the Mn to Fe ratio within the oxide layer, enabling the calculation of the amount of Mn lost from the alloy during HT oxidation. These findings offer valuable insights for controlling the surface behavior of steels during HT processing and highlight the need for further research on different iron alloys to understand the role of various alloying elements and their interactions in oxidation behavior.

Finally, in **Chapter 5**, kinetic data for high-temperature oxidation was extracted from published sources for various steel grades in dry air. To predict k_p, four machine-learning models—ANN, RF, KNN, and SVR—were employed using Python libraries like Scikit-learn and TensorFlow. Performance evaluation was based on metrics like MAE, MSE, RMSE, and R-squared, with accuracy being enhanced through hyperparameter optimization. The most influential factors were found to be the composition (e.g., Cr, Fe, Ni) and temperature. Effective relationships between input features (composition and temperature) and target value (k_p) were established by the models. The inclusion of more than three features did not result in significant improvements in predictions. RF outperformed others when trained on the top four features. KNN and ANN showed similar prediction accuracy, while SVR displayed larger errors. This research informs the prediction of oxidation behavior in new steel grades during the steel-making process, and the methodology is adaptable to other datasets and variables. Lastly, machine learning integrated with the automated design of experiments can be utilized to identify gaps in experimental datasets and suggest experiments for further improving model predictions.

Samenvatting

Hoge-temperatuur (HT) oxidatie speelt een belangrijke rol in verschillende stappen van het staalproductieproces, waaronder warmwalsen. De samenstelling van het staal kan bij het oppervlak veranderen doordat het blootgesteld wordt aan hoge temperaturen en zuurstofdruk, hetgeen legeringselementen uitput. Bovendien variëren de kenmerken van de oxide-laag, zoals dikte en fase samenstelling, afhankelijk van de oxidatieomstandigheden. Vanwege de experimentele uitdagingen bij het bestuderen van dergelijke snelle processen onder extreme omstandigheden zijn voorspellende modellen noodzakelijk. Deze kunnen worden gebruikt om de samenstelling van het substraatoppervlak, de oxidelaag en de algemene oxidatiesnelheid van de legering in te schatten.

Hoofdstuk 1 dient als een algemene inleiding tot de hoge-temperatuur oxidatie van metalen. Het benadrukt de relevantie ervan en omvat een overzicht van het proefschrift.

Hoofdstuk 2 omvat een hoofdstuk gericht op de achtergrond van voorspellende modellen voor HT-oxidatie in stalen en ijzer legeringen. Het presenteert de klassieke modellen voorgesteld door Carl Wagner en benadrukt de belangrijkste vooruitgang die is voortgekomen uit zijn theorieën. Deze modellen werden voornamelijk gebruikt om verschillende aspecten van HT-oxidatie te onderzoeken, zoals oxidatiemodi, oxidatiesnelheid, oxide samenstelling en veranderingen in de samenstelling van het substraatmetaal, met de nadruk op zuivere metalen en eenvoudige binaire legeringen. Het hoofdstuk behandelt vervolgens de beperkingen van modellen die op diffusie zijn gebaseerd en gaat verder met de bespreking van de daaropvolgende generatie van HT-oxidatiestudies. Hierbij worden ook data-gedreven methodologieën meegenomen. Het toont de mogelijkheid van verschillende Machine Learning (ML) algoritmen, waaronder KNN, ANN, RF, om de groeisnelheid van oxiden tijdens HT-oxidatie in verschillende legeringssamenstellingen te voorspellen.

In **Hoofdstuk 3** behandelt uitgebreide oxidatie-experimenten bij hoge temperaturen op ijzer legeringen met variërende Mn-inhoud, relevant voor Advanced High Strength Steels (AHSS), met behulp van een Thermogravimetrische analyse (TGA). Onder de meeste omstandigheden toonde de oxidelaag een initiële lineaire groei, overgaand naar parabolische groei onder specifieke omstandigheden. Het onderzoek toonde aan dat zuurstofdruk en gasstroom de primaire factoren zijn die de oxidatiekinetiek beïnvloeden, waarbij temperatuur en Mn-gehalte een minimale invloed hebben. Er werd een activeringsenergie van ongeveer 2 kJ · mol^{-1} verkregen. Naast de kinetiek onthulde een gedetailleerde analyse van de oxide-laag, met behulp van SEM, EDS en (in-situ) XRD-technieken dat het oxidatiemechanisme bestaat uit massatransport door een laminaire grenslaag in het gas. Dit resulteert in variaties in laagdikte langs de lengte van het

proefstuk. De experimentele resultaten die in dit hoofdstuk worden gepresenteerd, dienden als basis voor de ontwikkeling van het voorspellende model beschreven in **Hoofdstuk 4**.

In **Hoofdstuk 4** wordt een op diffusie gebaseerd model ontwikkeld om het HT-oxidatieproces van Fe-Mn legeringen te simuleren. Het model houdt rekening met zowel de chemische samenstelling van de oxide-laag als het uitputten van Mn in de substraatlegering. De groeisnelheidsconstanten van de oxide-laag vormen de invoer die nodig is voor dit model. Om deze constanten te verkrijgen, werden een reeks HT-oxidatie-experimenten uitgevoerd met behulp van een TGA. Tijdens deze experimenten werden ijzer-mangaan legeringen blootgesteld aan gasmengsels met variërende zuurstofdrukken (10-30 kPa) en gasstroom snelheden (26.6 tot 250 mL min^{-1}) bij verschillende temperaturen (950-1150 °C). Hierbij werd waargenomen dat temperatuurvariaties een cruciale rol spelen en de verdeling van Mn binnen de legeringen beïnvloeden tijdens oxidatie. Bovendien resulteert een verhoogde zuurstofdruk binnen het oxiderende gasmengsel in een snellere lineaire groei van de oxide-laag, die voornamelijk bestaat uit ijzeroxide (FeO) en mangaanoxide (MnO). Dit versnelde oxidatieproces leidt tot een hogere oxide-metaalgrensvlak recessie met als gevolg een dunnere Mn uitgeputte zone. Tot slot introduceert de studie numerieke simulaties die in staat zijn om de Mn – Fe verhouding binnen de oxide-laag te voorspellen, waardoor de berekening van de hoeveelheid Mn die verloren gaat uit de legering tijdens HT-oxidatie mogelijk is. Dit biedt waardevolle inzichten voor het beheersen van het oppervlaktegedrag van staalsoorten tijdens HT-verwerking. Ook benadrukt het de noodzaak van verder onderzoek naar verschillende ijzerlegeringen om de rol van verschillende legeringselementen en hun interacties in oxidatiegedrag te begrijpen.

Tot slot, in **Hoofdstuk 5**, werden kinetische gegevens voor oxidatie in droge lucht bij hoge temperatuur voor verschillende staalkwaliteiten verzameld uit de literatuur. Om kp te voorspellen, werden vier ML-modellen—ANN, RF, KNN en SVR—gebruikt met behulp van Python-bibliotheken zoals Scikit-learn en TensorFlow. De prestatie-evaluatie was gebaseerd op indicatoren zoals MAE, MSE, RMSE en R-kwadraat, waarbij de nauwkeurigheid werd verbeterd via hyperparameteroptimalisatie. De meest invloedrijke factoren bleken de samenstelling (bijv., Cr, Fe, Ni) en temperatuur te zijn. Effectieve relaties tussen ingevoerde variabelen (samenstelling en temperatuur) en de doelwaarde (k_p) werden door de modellen vastgesteld. Het opnemen van meer dan drie variabelen resulteerde niet in significante verbeteringen van de voorspellingen. RF presteerde beter dan de andere modellen wanneer het getraind wordt op de top vier variabelen. KNN en ANN toonden een vergelijkbare voorspellingsnauwkeurigheid, terwijl SVR grotere fouten vertoonde. Dit onderzoek draagt bij aan de voorspelling van oxidatiegedrag bij nieuwe staalkwaliteiten tijdens het staalproductieproces. Tevens is de methodologie aanpasbaar voor andere datasets en variabelen. Ten slotte kan Machine Learning, geïntegreerd met geautomatiseerd ontwerp van experimenten, worden gebruikt om lacunes in experimentele datasets te identificeren en experimenten voor te stellen ter verbetering van modelvoorspellingen.

1

Introduction

The term 'oxidation' in metals, is commonly defined as a chemical reaction that elevates the metal oxidation state, forming a compound such as oxide, sulfide, carbide, etc [181]. A traditional illustration of oxidation is the process of rusting. Rusting occurs when iron reacts with oxygen in the presence of water or moisture in the air to form iron(III) oxide. The chemical reaction is:

$$4Fe + 3O_2 \rightarrow 2Fe_2O_3 \tag{1.1}$$

Iron(III) oxide, commonly known as 'rust', gives the surface of the iron a reddish-brown appearance. Investigating the oxidation processes is crucial, as it enables the prevention or slowing down of undesirable oxidation reactions, such as iron rusting. Furthermore, understanding and predicting the mechanisms of oxidation reactions can aid in reducing material degradation.

In the study of oxidation reactions, a key consideration is the rate at which the reaction advances, known as the kinetics of oxidation. During oxidation experiments conducted in laboratories, researchers typically assess the oxidation rate by quantifying the weight of absorbed oxygen reacting with the metal. This technique is called thermogravimetric analysis and allows continuous monitoring of mass gain over time, providing valuable insights into the oxidation mechanism. Furthermore, this approach aids in identifying the controlling step of the oxidation reaction, which may involve either the diffusion of reactants to the reaction site or the chemical reaction among the present reactants.

One of the main parameters when studying the kinetics of oxidation is temperature. The effect of temperature on oxidation reactions is significant and is generally described by the Arrhenius equation. The Arrhenius equation relates the rate constant (k) of a reaction to the temperature (T) and includes an activation energy (E_a) term. The equation is given by:

$$k = A.e^{-\frac{E_a}{RT}} \tag{1.2}$$

1

The impact of temperature on oxidation reactions becomes evident also through laboratory experiments. While the oxidation of iron may require days at room temperature (rusting process), this timeframe significantly reduces to mere seconds at elevated temperatures [5]. This indicates a substantial alteration in the kinetics of oxidation with an increase in temperature. Consequently, the increased oxidation rates lead to more material loss and degradation, emphasizing the critical importance of studying the high-temperature (HT) oxidation of metals.

The steel-making process serves as an illustrative case highlighting the significance of HT oxidation. In numerous stages of this process, metals—predominantly iron—are subjected to elevated temperatures while being exposed to oxygen and water vapor, leading to oxidation. Although oxidation is undesirable, it is an inevitable aspect of these conditions. Hence, it becomes crucial to investigate HT oxidation effectively in both kinetic and thermodynamic aspects. This allows a thorough understanding of the oxidation behavior of steels, encompassing aspects such as material loss, consequent alterations in properties, surface degradation, and more.

Moreover, the exploration of HT oxidation extends beyond attempts to solely prevent or decelerate the process. The ability to predict oxidation properties is equally crucial. This thesis primarily focuses on predictive methodologies for HT oxidation of steel slabs during and after the hot rolling process (as illustrated in Figure 1.1), occurring before coiling. In this phase, the temperature ranges between 900 and 1100 °C, and the slabs are exposed to air and water vapor, creating an intensely oxidizing gas environment. Accurate predictions regarding the thickness and composition of the oxide scale are of great importance. They assist experts in designing preceding factors, such as the content of alloying elements and temperature, as well as subsequent steps, like optimizing descaling parameters, more effectively. Modifications to the preceding steps can be made to ensure an additional amount of material compensates for oxidation-related losses. Subsequent steps can then be designed based on the oxide thickness and adhesion to thoroughly descale the slabs and prevent surface defects in subsequent stages.

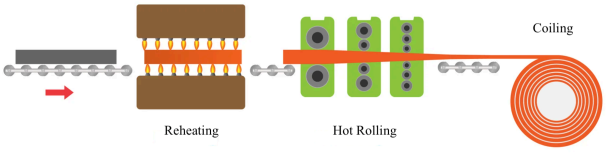

Figure 1.1: Schematic illustration of reheating, hot rolling, and coiling steps within steel-making process.

Considering the extensive global steel production, it is imperative to study HT oxidation in steels. However, the significance of HT oxidation knowledge extends beyond the realm of steel production. Understanding the HT oxidation of metals is crucial in various industrial applications where materials are exposed to elevated temperatures in oxidizing environments. Examples of such applica-

tions include jet engines in aerospace, heat-resistant alloys in power plants, and components in industrial furnaces. In all these processes, alloys are subjected to extreme temperatures, and their ability to withstand oxidation is essential.

Outline of the Thesis

Chapter 2 provides a thorough literature review of kinetic models predicting the HT oxidation behavior of steels and iron-based alloys. This review encompasses analytical, numerical, and data-driven approaches, shedding light on substrate alloy characteristics, internal/external oxidation, growth rate, and oxide composition. Chapter 3 focuses on short-time oxidation experiments, with the goal of elucidating the oxidation mechanism, pinpointing influential parameters, and analyzing the linear to parabolic growth transition across diverse Fe-Mn alloys. This study spans varying oxygen partial pressures (10-30 kPa) and gas flow rates (26.6 and 53.3 sccm) within a temperature range of 950-1150 °C. A comprehensive examination of the oxidized samples was conducted through SEM, XRD, and EDS characterizations. In chapter 4, a numerical model is developed to predict the formation of oxide phases and the composition profile of a steel alloy during short-term external oxidation. This model is applied to investigate the HT oxidation of Fe-Mn alloys under various conditions. To obtain input parameters for the model, oxidizing experiments are conducted using a thermogravimetric analyzer (TGA) on Fe-Mn alloys with varying Mn contents (below 10 wt%). These experiments helped to determine kinetic parameters critical for the model's accuracy. Finally, in chapter 5, a data analytics approach is employed to predict the parabolic growth rate constant (k_p) for the HT oxidation of steels. It stands as the most generic model developed for predicting the HT oxidation kinetics of various steel alloys and represents the culmination of this thesis.

2

Literature Review: Predictive Modelling in High-Temperature Oxidation of Steels

High-temperature oxidation of steel is a critical phenomenon influencing the performance and durability of products in various industrial applications. This work presents a comprehensive literature review on kinetic models forecasting the high-temperature oxidation behavior of steels and iron-based alloys. The review covers analytical, numerical, and data-driven approaches and offers insights into the substrate alloy characteristics, internal/external oxidation, growth rate, and oxide composition. The review highlights the strengths and limitations of each model, aiming to improve understanding of oxidation kinetics and guide future research and practical applications.

2

2.1. Introduction

Steel is being produced in large quantities around the world. In 2022 more than 1800 Mt of steel has been produced worldwide [174]. Nearly all of it is cast into massive slabs or other pieces, which are then heat treated between 1000 and 1200 °C for different purposes. Then a thick layer of oxide scale develops due to the presence of oxidizing gases at high temperatures during long heating times. This type of oxidation accounts for 1-2% of all steel consumption, which means around 18-36 Mt in 2022 [174]. Despite the fact that the oxide scale is mostly recycled in steel production, the cost of removing and reusing it is quite significant. Although steel scaling cannot be fully prevented, the identification of critical factors that impact its emergence, including steel composition, temperature, and oxygen partial pressure, plays a vital role in enhancing the effectiveness of steel production methods.

There are various reasons why studying the HT oxidation of steels is vital:

- To understand the degradation of steels in service.
- To improve the performance and lifetime of steels in HT environments.
- To develop new coatings and surface treatments.
- To develop new manufacturing processes.
- To comply with safety and environmental regulations.

Experimental investigation and characterization of the oxidation behavior of steels/alloys for a particular application are necessary because various factors such as composition, geometry, and the working environment affect scale growth. However, performing lab tests for numerous alloys/compositions requires significant time and effort. Therefore, computational methods along with thermodynamic/kinetics databases are developed to predict the HT oxidation behavior. This could reduce the need for experiments to the ones necessary for validating the predictions.

In the present work, a review of the physical and computational models used in the literature to forecast the kinetics of HT oxidation will be provided, with an emphasis on the oxidation of iron-based alloys and steels. The review starts with the historical development of such models and ends with an eye on the future of the field and prospective new developments.

2.2. The Theory of Kinetics of Oxide Scale growth

Oxidation is a chemical reaction that involves the removal of electrons from an atom, ion, or molecule, leading to an increase in its oxidation state. The oxidized species loses electrons, while the oxidizing agent gains them. In metal oxidation, oxygen is incorporated into the oxide scale, while the reactive metal is transferred to the alloy-scale interface, where it combines with the oxide scale. The various steps in the oxidation reaction of metals are shown in Figure 2.1.

Calculating the kinetics of an HT oxidation reaction requires identifying the oxidation mechanism and the rate-controlling step. As shown in Figure 2.1, there are three steps that can control the oxidation rate: (a) The diffusion of the oxidizing molecules through the gas layer, (b) the diffusion of the metal through the oxide layer, and (c) the adsorption of the gas and the reaction between the oxygen and the metal. The oxidation rate can be calculated through methods of fluid dynamics, diffusion theory, and surface chemistry. Therefore, as a function of the alloy composition, temperature, and gas environment, it is desirable to theoretically study an HT oxidation reaction in order to predict the oxidation rate, reaction product, and mechanical stability, as well as determine whether oxidation occurs internally or externally. However, experimental research may still be necessary for complicated systems. Theoretical predictions can offer qualitative cues for experimental design and effective laboratory research planning.

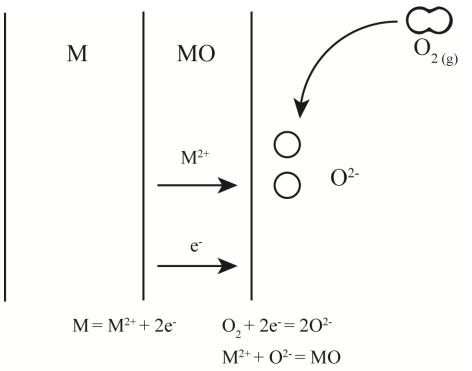

Figure 2.1: A schematic of the processes that contribute to the growth of an oxide scale through reactions and transport.

2.3. Measuring the Kinetics

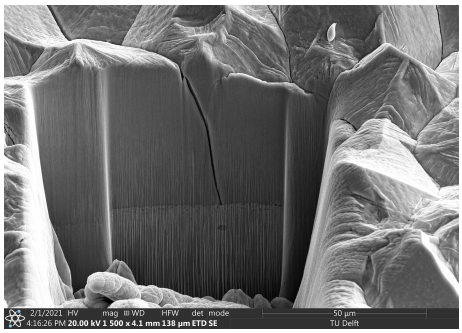

Figure 2.2: Cross-section of a Fe-7Mn alloy oxidized in air at 1000 °C for 20 minutes (the cross-section is made via FIB Helios).

The weight change of a metal or oxide accumulation over time is generally used to analyze the kinetics of oxidation reactions. Gravimetric measurement, done continuously with a microbalance or discontinuously by weighing multiple samples, is a practical method for this analysis. The weight change per surface area ($\Delta W/A$) can be translated to other parameters like metal consumption, surface recession, and oxide scale thickness [181]. The thickness of the oxide scale can also be directly measured using cross-sectional microscopic images (see Figure 2.2). For use in diffusion equations, the scale growth rate is expressed in terms of thickness rather than weight change. The general oxidation rate is written as Equation (2.1).

$$\frac{dX}{dt} = f(t) \tag{2.1}$$

The mechanism of oxidation determines f(t). The reaction steps can be divided into two main categories: (a) those that take place within the scale (parabolic growth), and (b) those occurring outside of it (linear growth).

2.3.1. Linear growth kinetics

Linear growth is observed when the oxidation is governed by reactions outside the oxide scale, therefore the scale thickness has no effect on the oxidation rate. As a result Equation (2.1) would be written as

$$\frac{dX}{dt} = k_l \tag{2.2}$$

Such a situation can occur when a metal is oxidizing at high temperatures in a gas environment with low oxygen partial pressure, where the diffusion through the oxide scale is so fast that it is not controlling the overall oxidation rate. Then the rate-determining steps could be the transfer of oxidizing molecules through the bulk gas to the scale surface, which is governed by the parameters of the gas mixture such as flow rate, oxygen partial pressure, and temperature. Also, surface reactions such as the dissociation of the gas molecules can be rate-controlling and lead to a linear growth rate.

2.3.2. Parabolic kinetics

When a compact oxide scale is growing, the growth rate is usually governed by the diffusion of the species within the scale. Then the growth rate is parabolic and it can be written as Equation (2.3).

$$\frac{dX}{dt} = \frac{k_p}{X} \tag{2.3}$$

The existence of parabolic oxidation kinetics was originally demonstrated experimentally by Tammann [152], and independently by Pilling and Bedworth [18]. Since diffusion is the controlling step, Fick's first law in one dimension could describe it [22]:

$$J = -D\frac{\partial C}{\partial x} \tag{2.4}$$

By considering the diffusion of species through the oxide scale as rate controlling it can be concluded that the processes at both metal/oxide and oxide/gas are rapid. These interfaces are then assumed to be in local equilibrium. Therefore, as shown in the Figure 2.3, the concentrations of the diffusing species at the interfaces (C_1 and C_2) are constant in time. The above assumptions were first implemented by Wagner [181]. He also established the relationship between the growth rate and the properties of the oxide scale such as diffusion coefficient, deficiencies, etc. His theories on oxide scale growth are further described in Section 2.4.

In the HT oxidation of metals, the parabolic growth rate can be influenced by a number of factors including temperature [137], oxygen partial pressure [180],

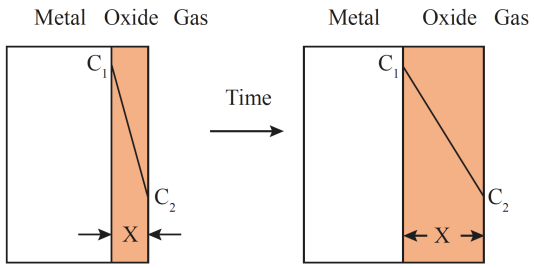

Figure 2.3: The schematic of a growing oxide scale. The concentrations of the diffusion species at metal/oxide and oxide gas interfaces are indicated as C_1 and C_2.

and alloy composition [102]. Since diffusion is the rate-determining step, k_p can be described with the Arrhenius relationship [181]

$$k_p = k_o \exp\left(\frac{-Q}{RT}\right) \tag{2.5}$$

Where Q and k_o are the activation energy and a constant, respectively, both of which are alloy-dependent.

2.4. Oxidation Kinetics of Pure Metals

2.4.1. Classical Wagner's theory of scale formation

The Classic theory of Wagner [181] focuses on steady-state kinetics, which is controlled by the lattice diffusion of ions or the transport of electrons/holes within the oxide scale with fixed boundary conditions. As mentioned in Section 2.3.2, this implies that the chemical potentials of the diffusing species at the interfaces are time-invariant (local equilibrium). Therefore, the boundary condition is governed by thermodynamics, i.e. the metal-oxidant phase diagram. Taking the first-formed iron oxide (wustite FeO) as an example, it is well known that the composition can significantly deviate from stoichiometry ($Fe_{1-\delta}O$). Accordingly, the oxygen potential gradient across the oxide scale (from the metal/oxide to oxide/gas interface) results in a defect (δ) gradient in the oxide [93]. Such deviations lead to different chemical potentials at the interfaces that depend on parameters such as temperature and oxygen partial pressure.

Wagner's model states that the lattice diffusion of species is rate-controlling, meaning that other diffusion processes play a negligible role in mass transfer [161]. Thus, it is assumed that grain boundaries and dislocations are present at relatively low densities in the oxide scale. Additionally, as it is anticipated that the gas-phase mass transfer within the scale will be negligible: the scale is assumed to be nonporous and adherent to the metal. Finally, by solving the transport equations and relating the diffusive flux to scale thickening, Wagner developed the Equation (2.6) for predicting the metal oxidation rate [181].

$$k_p = \int_{a_O'}^{a_O''} D_M \frac{1}{1-\delta} d \ln a_O \tag{2.6}$$

where a_O' and a_O'' are the boundary values for the activity of oxygen at the metal/oxide and oxide/gas interfaces, respectively. D_M is the diffusion coefficient and δ is the deviation from stoichiometry in the oxide. It can be seen that temperature can affect the k_p (Equation (2.6)) significantly because the diffusion coefficient [74], the deviation from stoichiometry [93], and the oxygen activities at the interfaces are all temperature dependent [181].

2.4.2. Validation of Wagner's model

To illustrate the accuracy of Wagner's model, the oxidation of iron as the main element in steel can be considered. When oxidized at temperatures above 570°C, iron can form an oxide scale composed of inner, intermediate, and outer layers of wustite, magnetite, and hematite, respectively. At temperatures at which diffusion is controlling the scale growth, the wustite layer is usually much thicker than the other two layers. That is because the iron diffusion coefficient in wustite is an order of magnitude higher than that in the other two oxide phases [67].

In work by Himmel [74], HT oxidation of iron was investigated using the radioactive tracer technique to determine D_{Fe} in wustite, magnetite, and hematite. Then the measured scale growth rates were compared with Wagner's findings. A good agreement was found between the calculated and measured values of k_p for both the oxidation of iron to wustite as well as for the conversion of one oxide to another, e.g. iron to wustite and wustite to magnetite, respectively (see Figure 2.4). Goursat et al. [67] also obtained agreement between measured parabolic constants and the ones calculated from Wagner's model.

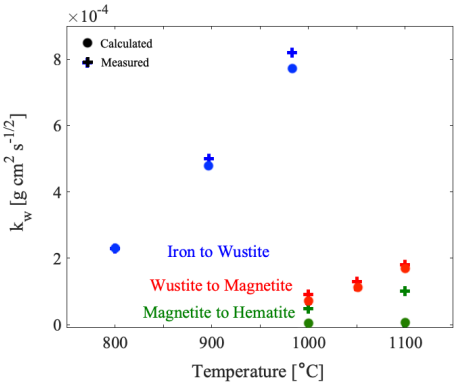

Figure 2.4: The comparison between measured and calculated values of parabolic growth rate constants as a function of temperature for oxidation of iron to wustite, wustite to magnetite, and magnetite and hematite [74].

Smeltzer et al. [142], compared the parabolic growth rate constants measured

in other works [47, 138] with the theoretical ones calculated with different diffusion coefficients [52] as inputs. As demonstrated in Figure 2.5, the experimental and calculated values are in good agreement throughout a broad temperature range, demonstrating the validity of Wagner's model.

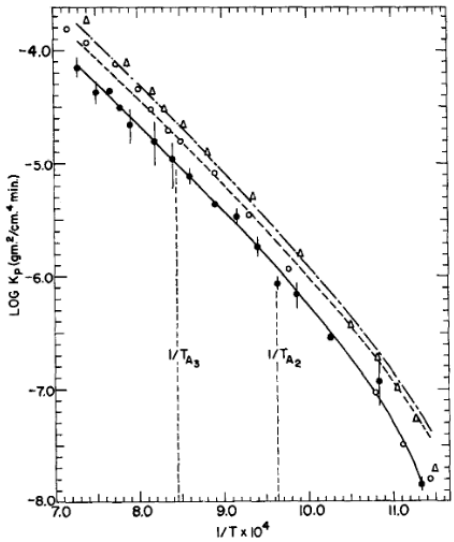

Figure 2.5: The comparison between measured (points) [47, 138] and calculated (curves) parabolic growth rate constants for oxidation of iron in oxygen as a function of temperature [142].

2.4.3. Limitations of Wagner's model

Wagner's model could accurately predict the growth rate in a fair number of cases, despite making certain questionable assumptions such as a dense oxide scale and no grain boundary effect (see Section 2.4.1). The use of Equation (2.6) is primarily hindered by the lack of input data needed to solve it. As a result, calculating the oxidation rate by finding the diffusion coefficients and the deviations from stoichiometry as a function of oxygen potential is more difficult than testing it experimentally. Therefore, the true importance of the theory lies in its capacity to elucidate the oxidation mechanism. This means that it clarifies how parameters like temperature and oxygen partial pressure impact the diffusion mechanism, and consequently the growth rate. Some major limitations of Wagner's theory are discussed in the following sections.

Impurities and substitute metals

Wagner assumed the oxidizing metals to be pure. However, that is usually not the case and the impurities can significantly affect the kinetics of oxidation because impurities can change the defect concentration in the oxide scale. The valence difference between the impurity and the solvent could change the vacancy concentration, i.e. it can rise by doping with a higher valent cation and vice versa. An

excellent illustration of this is the HT oxidation of Ni, which has been observed to proceed more quickly in situations when it includes a low concentration of Cr as an impurity [50, 190]. Thus, in the mentioned case of Ni oxidation with Cr impurities, to use Wagner's model (Equation (2.6)), the Cr concentration profile within the scale is needed. The oxidation of multi-component systems is described in more detail in Section 2.5.

Microstructural effects

In his classic model, Wagner assumed the oxide layer to be dense and adherent to the metal substrate with lattice diffusion as the only way of mass transportation within the oxide scale. Such conditions are not always met in practice.

Grain boundary effect: The formed oxide scales are usually polycrystalline and therefore at higher temperatures, the diffusion occurs both through the lattice and the grain boundaries. However, at lower temperatures, diffusion primarily occurs through the grain boundaries, which is not accounted for in Wagner's model. Herchl [71] showed this effect for NiO. The effect of grain boundary diffusion was considered by Smeltzer [143] for oxidation of Ni by defining an effective diffusion coefficient including both lattice and grain boundary diffusion contributions

$$D_{eff} = D_L(1 - f) + D_B f \tag{2.7}$$

where D_L and D_B are the lattice and bulk self-diffusion coefficients, respectively. f is the fraction of diffusion sites within the boundaries.

Scales with more than one layer: In many HT oxidation cases -including iron- the scale consists of more than one layer, which can be predicted via the phase diagrams. The oxide layers interfaces are in local equilibrium, so the values for oxygen activities (a_O) are fixed and could be calculated at those points. The classic examples are the oxidation of iron, copper, and cobalt. The iron oxide scale, for instance, can be formed of wustite, magnetite, and hematite, depending on the oxidizing condition such as temperature and oxygen partial pressure [16] (see Figure 2.6).

Although the produced oxide phases may be predicted, it is not possible to directly estimate the growth rate of each layer from the diffusion fluxes since there is extra mass transfer at the interfaces. Several authors have worked on theories to determine the thickness of simultaneous forming oxides during HT oxidation [87, 62, 78, 167]. By implementing the theory of the growth of two oxide layers by Yurek [187] in HT oxidation of iron, Gernaud and Rapp [58] determined the parabolic growth rate constants for each iron oxide phase individually in the presence of the others. Finally, the oxide phases thickness ratio values from experiments (Figure 2.7) were in good agreement with the calculated ones.

In a recent work, Larsson [92] combined the independently assessed thermodynamic and kinetic data for the Fe–O system to predict the evolution of hematite, magnetite, and wustite layers during oxidation at 600°C in dry oxygen. He calculated the effective mobility by considering the grain boundary mobility, the volume fraction of grain boundaries, and the bulk (lattice) mobility. Finally,

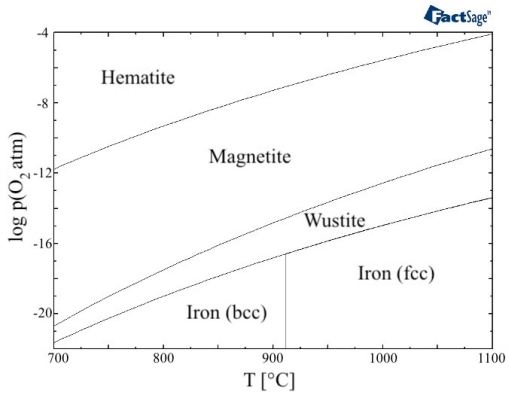

Figure 2.6: The iron oxygen phase diagram plotted via FactSage software [16].

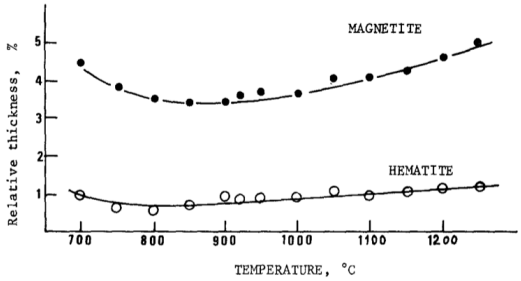

Figure 2.7: Relative thicknesses of magnetite (Fe_3O_4) and hematite (Fe_2O_3) in the scaling of iron in the air [118].

he demonstrated that the variations in the wustite/magnetite thickness ratio can be at least partly attributed to the impacts of grain growth and the corresponding changes in the contribution of grain boundary diffusion.

Macroscopic defects (surface spalling, pores, and cracks): Wagner's model assumes that the oxide scale is dense and adhered to the substrate, however, this is not always the case. One of the main causes of scale defects like cracking and spallation is the stress generated in the oxide scale [176]. In oxide scales, two basic types of stresses often occur: thermal stress, caused by the difference in thermal expansion between the oxide scale and the metal substrate, and growth stress, which develops during the oxidation process and has a complex origin that is not fully understood. The volume change caused by the development of the oxide at the metal/oxide interface can cause growth stress and is described using the Pilling-Bedworth ratio (PBR) [176].

$$PBR_{metal} = \frac{Volume\ of\ oxide}{Volume\ of\ metal} \tag{2.8}$$

It is commonly acknowledged that when the PBR is more than 1, compressive

stress occurs in the oxide scale, and when the PBR is lower than 1, tensile stress develops. The PBR model served as the foundation for modern models of growth stress [135] and has been often implemented for its explanation of how stress is generated during oxidation [19] to predict cracking and spallation.

Another parameter that can change the scale adhesion on the substrate and its porosity is the gas environment. Chen [37] discovered that the addition of water vapor to the atmosphere completely altered the oxidation characteristics of low carbon and low silicon steel. First, the scale formed in 1% O_2-N_2 was easier to spall after cooling, whereas the scale formed in the atmospheres containing water vapor was not. Moreover, the addition of 2.5–10% water vapor caused the formation of a number of depressed spots -i.e. where the scale is thinner-, and at these spots, the scale-steel adhesion was significantly strengthened. Finally, by the additions of 17.2 and 24.8% water vapor to the environment, the formation of depressed spots and scale spallation upon cooling were both prevented. The results from other research [156, 82, 183] on the effect of gas environment on the adhesion and porosity of the oxide scale on pure iron were in good agreement with Chen's. Ehlers' [51] explanation of how oxygen is transported through the scale with the assistance of water vapor in the pore is depicted in Figure 2.8. It is suggested that the molecules of water vapor might appear in the in-scale voids. At the surface, closest to the scale/metal interface, water molecules oxidize the metal in the void thereby releasing hydrogen gas. These hydrogen molecules reduce the oxide at the void surface closest to the scale/gas interface. By accelerating the inward transport of oxygen, this mechanism which is called H_2O-H_2 bridge process, increases the rate at which metals oxidize. Moreover, it causes the voids to shift from the interior to the external interface, enhancing scale adhesion. In conclusion, defects such as pores, cracks, and spallation can occur in oxide scales but were not considered in Wagner's model.

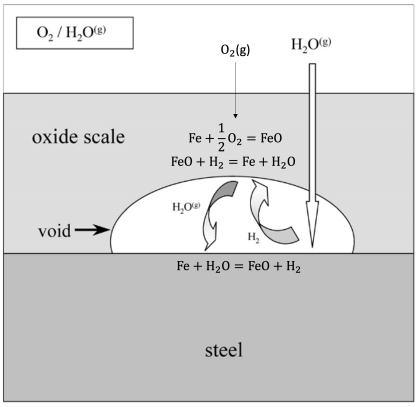

Figure 2.8: The transportation of water vapor molecules through the scale and oxygen transfer across in-scale void via "H_2O-H_2 bridge" process [51].

Reactions not controlled by diffusion through the scale - linear growth rate

Contrary to what Wagner assumed, HT oxidation does not always occur at steady-state conditions. If either the interfacial process (reactions) or gas-phase mass transfer is slower than diffusion within the scale, a linear scale growth rate would occur.

A linear growth rate is widely reported for HT oxidation of iron in low oxygen partial pressures (p_{O_2}) where only wustite can form [124, 142]. To keep p_{O_2} low for only wustite to form, gas mixtures of CO + CO_2 and H_2 + H_2O are used. So

p_{O_2} would be as low as around 10^{-14} atm at 1000°C where the gas-phase dissociation of both CO_2 and H_2O as the main species, is relatively slow. Therefore, in such cases, the dissociation of CO_2 or H_2O to adsorbed oxygen and CO/H_2, respectively, controls the scale growth rate via the reaction [124]

$$CO_2(g) + S = CO(g) + O|S \tag{2.9}$$

where S is a surface adsorption site. Pettit [124] developed a model to show that in a gas mixture of CO + CO_2, the iron oxidation linear rate depends on p_{CO_2} and also the total gas pressure. The calculated effect of gas pressure and composition on the oxidation kinetics of iron was shown to be in agreement with the experiment (see Figure 2.9).

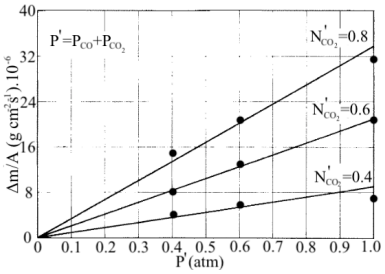

Figure 2.9: Dependence of the linear rate constant on the sum of the partial pressures of CO and CO_2, in the gas phase for a temperature of 1100 °C [124].

Investigation on the oxidation of low-carbon steels in simulated reheat furnace atmospheres by Lee et al.[96] showed that when linear, the growth rate was controlled by the surface reactions (oxygen uptake reactions). It was determined that since the oxide growth rate fluctuates with changing gas compositions, the surface is not saturated with adsorbed CO_2. Finally, the following expression to predict the linear growth rate of the wustite when controlled by the surface reactions was proposed:

$$k_l = \frac{p_{CO_2}}{a + b\, p_{CO}} \tag{2.10}$$

where a and b are constants. The data were found to fit this expression well when with $a = 0.375$ mg^{-1}cm^{-2}s atm and $b = 27.3$ mg^{-1}cm^{-2}s [96]. A similar treatment is valid for the H_2O surface reaction, but with different a and b constants.

Finally, there is another regime of linear growth rate observed when iron is oxidizing at high temperatures in dilute oxygen-bearing gases. Abuluwefa [2] worked on the oxidation of low carbon, low silicon steel in a gas mixture with up to 16% O_2 at temperatures between 1000 and 1250 °C. It was found that the initial linear rate constant had a very low activation energy of 17 kJmol^{-1}, with a growth rate that was directly proportional to p_{O_2}.

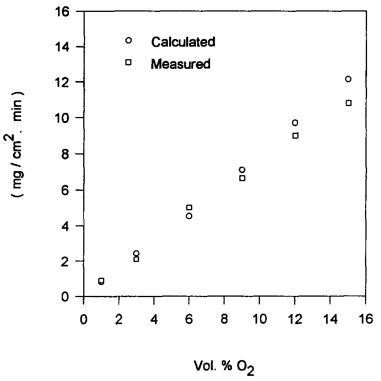

Figure 2.10: Comparison between calculated and measured values of the linear oxidation rate constant for different oxygen concentrations at 1200 °C [2].

The linear oxidation rate constants calculated using Equation (2.11) for the mass transport of oxygen in the gas mixture to the sample surface were in good agreement with experimental measurements (see Figure 2.10), proving that the mass transport of oxygen to the reaction interface controls the initial phase of oxidation.

$$k_l = M_O k_{MTC} \left(C^G_{O_2} - C^*_{O_2} \right) \qquad (2.11)$$

M_O is the molar mass of atomic oxygen (g/mol), and the molar concentrations of oxygen in the bulk gas and at the sample surface are shown with $C^G_{O_2}$ and $C^*_{O_2}$ (mol/cm^3), respectively. k_{MTC} is the mass transfer coefficient (cm/s) that can be obtained from the convective mass-diffusion equation across a laminar boundary layer to a flat surface with a known bulk gas velocity [97].

Slow-growing oxides

The Wagner approach is found to be applicable when the scale growth is governed by solid-state diffusion, provided that sufficient information about the characteristics of the oxide defects is available. In cases of slow-growing oxides such as Al_2O_3 and Cr_2O_3, where there is a lack of knowledge about defect properties and the oxygen potential effect on them, Wagner's approach cannot be used. Furthermore, diffusion in these oxides is usually via the grain boundaries, and as discussed in Section 2.4.3, then the measured scale growth rates are very different from the ones predicted with Wagner's model [72].

2.5. Oxidation Kinetics of Steels

The kinetic models for the HT oxidation of pure metals, primarily iron, were covered in Section 2.4. However, usually, a variety of elements is present and involved in oxidation, which complicates the kinetics. In this section modes of alloy oxidation are discussed with a focus on steels. Models to forecast the conditions under which each of these modes operates and to determine the rate at which the alloy is consumed will be discussed [163, 164, 160].

2.5.1. Formation of solid solutions

In HT oxidation of binary alloys, the oxides (AO_{v_1} and BO_{v_2}) may form solid solutions. In particular, when conditions are met such as [181]:

1. $v_1 = v_2$

2. the oxides having a similar crystal structure
3. the cations having similar size and polarisability
4. the oxides having close stability.

Oxides like MnO, FeO, CoO and NiO, which form a face-centered cubic NaCl structure, are examples of $A_{1-\xi}B_{\xi}O$ solid solution oxides where $0 \leq \xi \leq 1$. The N_A/N_B ratio (with N_A and N_B as the mole fraction of components A and B, respectively) in these oxides can be different from that in the substrate alloy, because of the difference in the stability of the oxides (see Figure 2.11, the stability of an oxide has an inverse relationship with its Gibbs free energy of formation). Additionally, the composition of the oxide varies with the position in the scale, due to changes in the diffusion coefficients of cations, D_A and D_B, with position within the scale. To calculate the distribution of the two metals within the scale, Wagner [163] developed a diffusion-based model which was later extended by Coates [42]. Next, it was applied by Mayer and Smeltzer [108] for the oxidation of Fe – Mn alloys exposed to CO_2 – CO at 1000 °C, where single-phase (FeMn)O scales grow parabolically. This investigation made it feasible to determine the iron and manganese self-diffusion coefficients as well as the nonstoichiometry of wustite in relation to manganese content (see Figure 2.12).

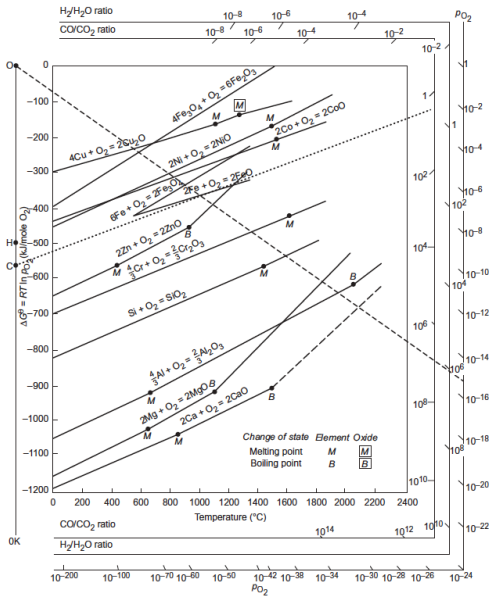

Figure 2.11: Ellingham/Richardson diagram illustrating the free energies of formation for different oxides as a function of temperature, together with corresponding equilibrium p_{O_2} and p_{O_2}/p_{H_2O} and p_{CO}/p_{CO_2} ratios [181].

Similar studies on the solid-solution oxide scales that formed on Co-Fe [106, 107] and Ni-Fe [45] alloys showed a good agreement between the calculated

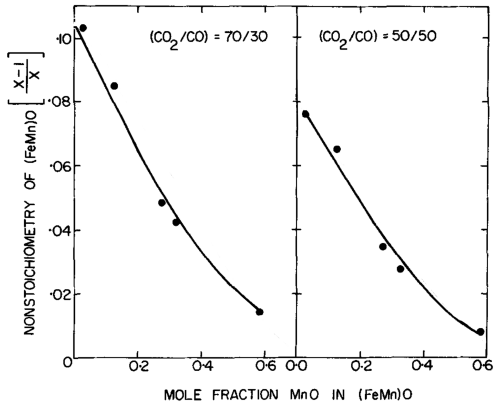

Figure 2.12: The nonstoichiometry of $(FeMn)_{1-\xi}O$ as a function of mole fraction of MnO in the scale at 1000 °C. The points are calculated through Wagner's model, and the curves are measured in the experiments [108].

and measured concentration profiles within the oxide scale, as can be seen in Figure 2.13.

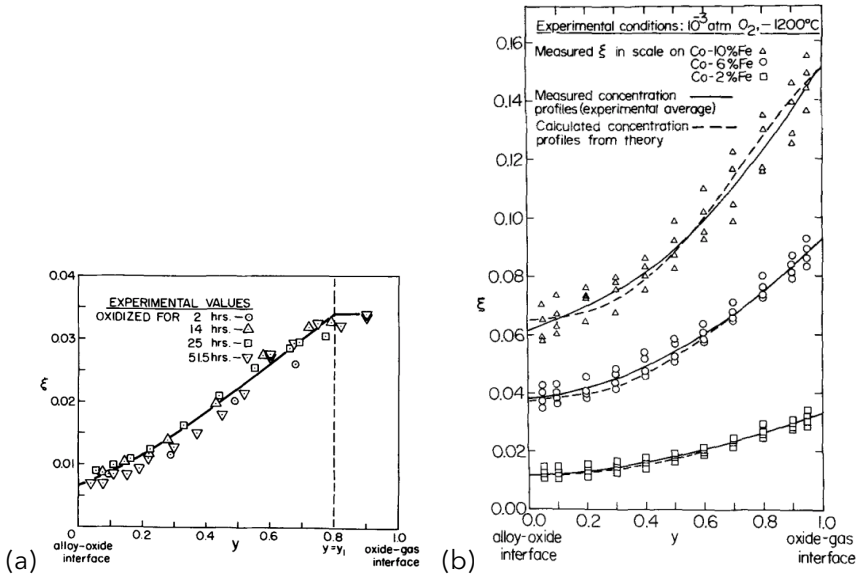

Figure 2.13: Comparison between the calculated and measured FeO Mole fraction (ξ) vs. the normalized distance coordinate y in (a) the (Ni, Fe)O scale layer formed on the Ni alloy containing 2 wt% Fe (the solid curve represents calculated values [45]), and in (b) the (CoFe)O scales formed on the Co alloys with 10, 6, and 2 wt% Fe [106].

2.5.2. Selective oxidation

Depending on the oxidizing condition, either one or more of the components can oxidize. In the case of selective oxidation in a binary alloy AB, the oxidizing condition is only met for the less noble element (B) to form an oxide (BO). As a result, the concentration of B drops at the surface while that of A rises. The concentration drop of element B can either cover a large region of the alloy or be limited to the subsurface area, depending on whether the rate of diffusion is greater or lesser than the rate of oxidation (see Figure 2.14). Therefore, in the case of relatively fast diffusion, there is no depletion of B in the metal substrate. As is the case for HT oxidation of Fe–Cr when the p_{O_2} value is high enough for the formation of Cr oxides (less noble) but not for Fe oxides.

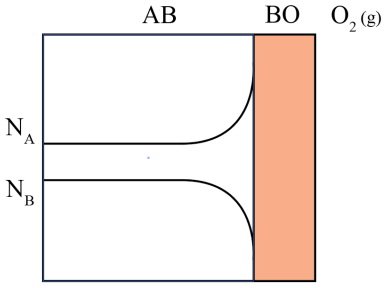

Figure 2.14: The depletion of the more reactive alloying element (B) and enrichment of the more noble component (A) below the oxide (BO)/metal (AB) interface. N is the mole fraction of the elements.

Wagner [164] showed that in the internal oxidation of AB (with B, the less noble element forming a BO scale), the rate-controlling step can be the diffusion of B through the AB alloy or diffusion through the BO scale. If diffusion through the scale controls the oxidation rate, the rate should be equal to that of pure B. The oxidation rate would be much slower if the alloy diffusion is controlling the rate. So, by comparing the oxidation rate of pure B with that of the AB alloy the controlling mechanism could be determined. In the case of Pt–Ni [164], the growth rates of the NiO scale on Pt–Ni and pure Ni were compared. Considering that these rates are proportional to nickel cation flux to the oxide, Wagner calculated the ratio α.

$$\alpha = \frac{J_{Alloy}^{NiO}}{J_{Metal}^{NiO}} \tag{2.12}$$

For Pt-Ni at temperatures of 850 and 1100 °C in air, $\alpha \approx 1$, which means that the oxidation is controlled by diffusion in the NiO oxide scale. This implies that there is a minimum amount of Ni required at the oxide/metal interface to support the flux of Ni to the oxide surface. This amount is also related to the original Ni level in the bulk alloy. So, in the case of AB alloy, the critical amount of alloying element B, above which the alloy can sustain an oxide scale growth is determined by Equation (2.13).

$$N_B^{(0)}{}_{min.} = \frac{V_m^{AB}}{V_m^{BO}} \left[\frac{\pi\, k_p}{2\tilde{D}_{AB}} \right]^{1/2} \tag{2.13}$$

where k_p is the parabolic growth rate of the BO scale, $\tilde{D}_{AB}$ is the interdiffu-

sion coefficient in AB assumed to be independent of concentration. V_m^{AB} and V_m^{BO} are the molar volume of the alloy and the oxide, respectively. Lashgari [93] used Equation (2.13) to calculate the minimum manganese concentration in a Fe–Mn binary to sustain MnO scale growth to be 23 wt%. Similar calculations for slow-growing scales on iron-based alloys such as Fe–Cr [173] and Fe–Al [14] resulted in much lower values for Fe–Al than for Fe–Cr. This is due to the lower k_p and higher alloy diffusion in the case of alumina-forming alloys. The calculated minimum concentrations for Cr and Al to sustain external scale growth were 0.07 and 10^{-4}, respectively, while the experimental values were 0.14 and 0.02-0.04, respectively.

The discrepancy between the measured and calculated minimum concentrations of the alloying element (Equation (2.13)) to sustain the scale growth is amongst others due to the sensitivity to the input data, k_p and $\tilde{D}$. Moreover, again lattice diffusion is assumed, but in some cases such as Pt–Ni, where a NiO scale grows, grain boundary diffusion is dominating at temperatures below 900°C [181]. Additionally, Wagner's assumption that the oxidation to be steady-state from the start could not be met. The nonsteady-state was studied using numerical methods like finite difference methods to calculate the diffusion coefficient as a function of composition [170, 175, 17, 115, 116], the variation of the interfacial concentration with time [170, 115, 116, 5], and the interface recession [115, 116, 5].

Internal oxidation

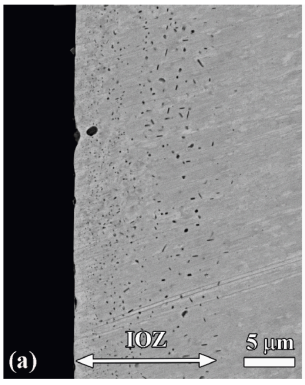

Figure 2.15: SEM image (backscattered electrons) of a cross-section of a Fe-1.7 at % Mn steel, after annealing for 16 hours at 950 °C in a gas mixture with oxygen partial pressure of 1.0×10^{-18} atm. An IOZ of around 15 microns is seen to be formed [101].

Internal oxidation generally occurs when (i) an alloy component is selectively oxidized but cannot reach the surface rapidly enough to form a scale or (ii) when an alloy is selectively oxidized to form a scale, and depletion of the oxidized component underneath the scale can lead to internal oxidation. Therefore, in some conditions, internal and external oxidation can occur simultaneously. Preventing internal oxidation is crucial in ensuring the durability of materials operating at high temperatures as it is the primary cause of failure [94].

A typical example of internal oxidation is shown in Figure 2.15 by Mao et al. [101], where internal precipitation of MnO had occurred because the p_{O_2} was so low that iron oxides were not stable to form. Obviously, oxygen has dissolved and diffused inside the alloy to form MnO precipitates. The internal oxidation zone (IOZ) or depth of precipitation zone X_i grew according to the parabolic kinetics.

$$X_i^2 = 2k_p^i t \tag{2.14}$$

where k_p^i is the parabolic growth rate constant for internal oxidation. Furthermore, various other studies [95, 134] have reported that diffusion governs the internal oxidation process.

Internal oxidation can be influenced in different ways. Dilute alloys form internal precipitates, while increased alloying element content can promote the formation of a scale along with internal oxidation. An even higher amount of the alloying element can lead to the formation of only the oxide scale. The volume fraction and shape of the precipitates are additional factors that impact internal oxidation, as the precipitates act as hindrances to the species' diffusion [46]. Furthermore, mechanical deformation and surface roughness could accelerate diffusion by introducing subsurface defects that could act as additional diffusion pathways. Finally, the precipitates can form either within the grains or on the grain boundaries [181].

In general, in an AB binary alloy there are three conditions for the internal oxidation of alloying element B:

1. BO is more stable than AO.
2. oxygen can dissolve in the alloy and diffuse internally to reach an activity high enough to stabilize BO but not AO.
3. N_B is low enough to form only internal oxidation and not an oxide scale.

The internal oxidation of component B when both B and oxygen are mobile is shown in Figure 2.16. By assuming very small values of N_O and N_B at the reaction front (low solubility product), Wagner [160] solved the equation for Fick's second law of diffusion for both B and O:

$$\frac{\partial N_i}{\partial t} = D\frac{\partial^2 N_i}{\partial x^2} \tag{2.15}$$

with the boundary conditions:

$$\begin{aligned}
&N_O = N_O^{(s)} && \text{for} \quad x = 0, && t > 0\\
&N_O = 0 && \text{for} \quad x \geq X_{(i)}, && t > 0\\
&N_B = N_B^{(0)} && \text{for} \quad x > 0, && t = 0\\
&N_B = 0 && \text{for} \quad x \leq X_{(i)}, && t > 0
\end{aligned}$$

By considering the mass balance at the reaction front ($x = X_(i)$), Wagner calculated the parabolic growth rate of internal oxidation through Equation (2.16).

$$k_p^{(i)} = \frac{\pi}{2D_B}\left(\frac{D_O N_O^{(s)}}{2\nu N_B^{(0)}}\right)^2 \tag{2.16}$$

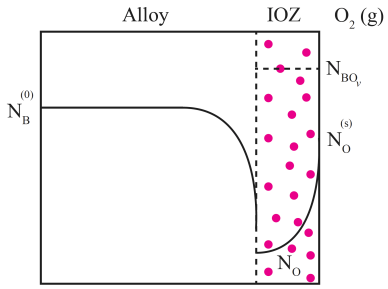

Figure 2.16: The schematic representation of internal oxidation of component B in an alloy.

Wagner [162] and Rapp [134] showed that there is a critical concentration of the less noble element in alloys above which there is a transition from internal to external oxidation. This is due to the fact that the precipitates are considered as obstacles for diffusion, thereby reducing the average flux. Hence, if $N_B^{(0)}$ is high enough for the flux required to maintain the precipitates' growth, their expansion leads to the production of a continuous oxide layer. The volume fraction of internal oxide BO, g_{BO}, can be calculated by

$$g_{BO} = f_{BO}\frac{V_{BO}}{V_A} \tag{2.17}$$

where f_{BO} is the mole fraction of BO. Then, Wagner concluded that $N_{B,min}^{(0)}$ would be the minimum value required for the formation of an external scale.

$$N_{B,min}^{(0)} = \left(g_{BO}\frac{\pi}{2v}\frac{V_A}{V_{OX}}\frac{N_O^{(s)}D_O}{D_B}\right)^{1/2} \tag{2.18}$$

Combining Equation (2.18) with Sievert's law for dissolution of gases in metals gives Equation (2.19)

$$N_{B,min}^{(0)} = \left(g_{BO_v}\frac{\pi}{2v}\frac{V_A}{V_{OX}}\frac{K\,p_{O_2}^{1/2}D_O}{D_B}\right)^{1/2} \tag{2.19}$$

where K is Sievert's constant for O in iron. Despite impressive effectiveness of Wagner's diffusion model in describing internal precipitation reactions, its applicability is constrained by the assumptions made. These assumptions are:

1. The values of N_B and N_O are zero in IOZ.
2. f_{BO} is constant in IOZ and zero at the reaction front.
3. The effect of nucleation and growth of the precipitates is not considered in the reaction kinetics.

4. Only lattice diffusion is assumed and it is considered to be unaffected by the formed precipitates.

2.5.3. Scales with several phases

Steels contain multiple alloying elements and most of them are prone to oxidation in a variety of environments. To predict oxidation behavior as a function of the steel composition and the oxidizing environment the simultaneous growth of several oxides needs to be taken into account. This section starts with binary iron-based alloys and moves forward with more complex steels. The effect of chromia and alumina scale formation as well as minority component effects are reviewed in this section.

Fe-Al

According to the phase diagram of the Fe – Al – O system, Al_2O_3 is by far the most stable oxide, which implies that the alloys, even those with very low Al contents, are in equilibrium with Al_2O_3. Boggs [24] demonstrated that in alloys containing less than 0.09 wt% Al, at temperatures below 570 °C the scale consisted of α-Fe_2O_3 and Fe_3O_4 at the scale/gas and scale/alloy interfaces, respectively. A third phase, $FeAl_2O_4$, was formed between the alloy and Fe_3O_4 at above 0.09 wt% Al. The protective phase, γ-Al_2O_3, started to form at the bottom of the scale at temperatures above 570 °C, leading to a decrease in growth rate. At around 800-850 °C, the oxidation rate was at its lowest, and the film was nearly entirely alumina. γ-alumina was developed at low temperatures (above 570 °C), and gradually transformed into α-alumina as the temperature increased (to 800-850 °C).

Since α-Al_2O_3 does not deviate measurably from stoichiometry, the defect concentration in its structure is very low and the self-diffusion is consequently very slow. Lattice diffusion measurements by Heuer [72] lead to the conclusion that $D_l^O \gg D_l^{Al}$, where at 1100 °C, $D_l^O = 10^{-15} cm^2 s^{-1}$, which is too low to control the observed scale growth rates. Therefore, it is expected that grain boundary diffusion occurs. Reviewing the available diffusion data, and assuming a grain boundary width δ of 1 nm, Heuer et al. [73] showed that D_{gb}^O/D_l^O is about 10^6 at 1500 °C. However, there is no good agreement between the found oxygen grain boundary diffusion coefficients (see Figure 2.17). Also, no tracer diffusion data is available for grain boundary diffusion of aluminum.

Given that grain size is known, the results of the oxygen permeability serve as the foundation for the scale growth kinetics prediction supported by grain boundary diffusion [144, 73, 72]. So, Equation (2.7) is approximated by

$$D_{eff} \approx f D_{gb}^O = \frac{2\delta D_{gb}^O}{G_i} \tag{2.20}$$

where G_i is the grain diameter as a function of time and position within the scale. As a result, it is advisable to treat the scale growth rate as an instantaneous variable because it is reliant on grain size (subscript "i"). Substituting Equation (2.20) in Equation (2.6) then yields

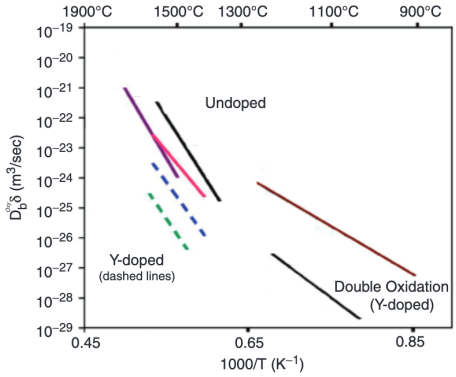

Figure 2.17: An Arrhenius plot showing the best available grain-boundary diffusivity data for oxygen in Al_2O_3 [73].

$$k_{p,i} = \int_{p_{O_2,int}}^{p_{O_2,gas}} \frac{2\delta D_{gb}^{O}}{G_i} d \ln p_{O_2} \tag{2.21}$$

The oxygen grain boundary diffusion term as a function of temperature and oxygen pressure from permeability measurements [159] is

$$\delta D_{gb}^{O} = 1.52 \times 10^{-8} exp\left(\frac{-467kJ}{RT}\right) p_{O_2}^{-1/6} \, cm^3 s^{-1} atm^{-1/6} \tag{2.22}$$

Combining Equation (2.21) and Equation (2.22), and integrating from one side of the scale to the other results in

$$k_{p,i} = -\frac{12A}{G_i}\left[\left(\frac{1}{p_{O_2,gas}}\right)^{-1/6} - \left(\frac{1}{p_{O_2,int}}\right)^{-1/6}\right] \approx \frac{12A}{G_i}\left(p_{O_2,int}\right)^{-1/6} \tag{2.23}$$

where $A = 1.52 \times 10^{-8} exp\,(-467kJ/RT)$. Such an approximation is reasonable because the equilibrium oxygen partial pressure at the metal/oxide interface is much lower than the oxygen partial pressure in bulk gas at the surface of the scale. In Figure 2.18 the measured parabolic rate constants for different FeCrAl alloys are compared to those calculated by Equation (2.23) using a grain size of 0.5 µm. Although the predicted values are at least one order of magnitude greater than the measured ones, they are still more accurate than extrapolations of bulk alumina diffusivity studies conducted without a p_{O_2} gradient. The author related such discrepancy to the fact that the calculations are done for pure alumina while the experimental values are measured from doped alumina scales. However, there are additional potential sources of deviations, such as the effect of varying grain size (which was assumed to be constant), or the oxygen grain

boundary diffusion coefficient value, which varies across reports based on permeability measurements as shown in Figure 2.17.

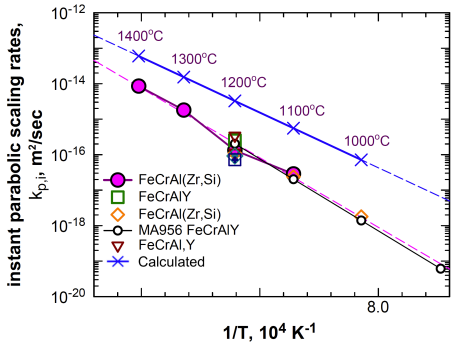

Figure 2.18: Instantaneous $k_{p,i}$ measured for G_i = 0.5 µm, compared to predictions from Equation (2.23) [144].

Fe-Cr

HT oxidation in diluted Fe–Cr alloys is controlled by the development of the wustite (FeO) scale. Depending on the temperature, Cr_2O_3 precipitates can also form internally. When the scale/metal interface progresses, the precipitates may become a part of it and transform into spinel. The larger the $N_{Cr}^{(0)}$, the greater the volume fraction of spinel is, until it reaches a crucial point at which the chromia phase begins to form (see Equation (2.19)). Young [181] calculated the critical Cr content (wt%) required in an austenitic Fe–Cr alloy at 1000 °C to avoid internal oxidation to be 0.16, which was very close to the measured value of 0.14.

Young [181] also showed that Fe–Cr alloys with chromium levels close to the critical value, $N_{Cr,min}^{(0)}$, cannot show long-term oxidation resistance. This is due to the high solubility of iron in Cr_2O_3 allowing the outward diffusion of iron and the formation of iron-rich oxides (spinel $FeCr_2O_4$) at the scale surface. A Cr content of around 25% was suggested to obtain long-term oxidation resistance. Kofstad [87] concluded that chromia scale growth is governed by outward diffusion of chromium, based on the early works on chromia scale growth rates and the proposed mechanisms. Later works [119, 145] showed that grain boundary diffusion is much faster than the lattice diffusion for both chromium and oxygen.

An estimate of the diffusion of iron from the metal/scale interface through the chromia scale towards its surface can be obtained by the 'pre-oxidation' technique [181]. Firstly, the alloy is subjected to a round of oxidation at low p_{O_2}, where wustite is unstable and only a protective Cr_2O_3 scale forms. Then, larger oxygen partial pressures are applied to provide a driving force for iron diffusion through the chromia layer to form iron oxide. The penetration distance of iron by diffusion is then given by

$$X^2 \approx 4D_{eff}(Fe)t \tag{2.24}$$

where $D_{eff}(Fe) = 1 \times 10^{-15} cm^2 s^{-1}$ [98]. Young [181] found a good agreement between the calculated and the measured values of penetration time of iron upon the oxidation of Fe with 7.5 and 9 wt% Cr for a 1 μm thick chromia scale.

Fe-Ni-Cr

Since data for $N_O^{(s)}$ and D_O are not available for Fe–Ni binaries, it is not possible to calculate the minimum Cr content for scale formation on Fe–Ni–Cr alloys using Equation (2.18) or Equation (2.19). Therefore, knowledge about the kinetics for HT oxidation of these alloys is mostly qualitative. Croll et al. [43] showed that for a given chromium content, the oxidation rates of Fe–Ni–Cr alloys decrease with an increase in nickel content (see Figure 2.19). Moreover, for a given nickel content, increasing Cr from zero to 10 wt% did not significantly influence the oxidation rate. Chromium was internally oxidized and the oxidation was controlled by diffusion through the scale, which was mainly consisting of $NiFe_2O_4$ and NiO. At chromium contents between 10 and 20 wt%, a layer of chromia was formed beneath the $NiFe_2O_4$ and NiO scale. Cr contents above 20 wt% caused the formation of a predominant chromia layer with low diffusion rates through the scale and consequently low oxidation rates, comparable with that of pure chromium.

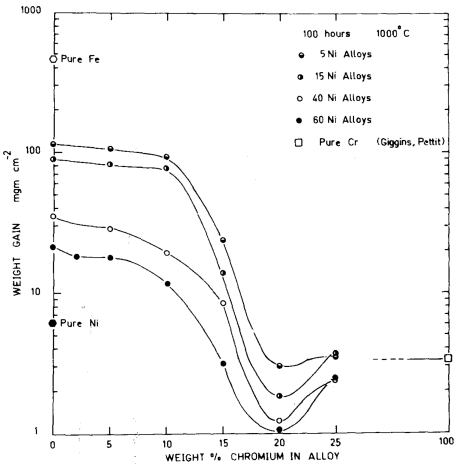

Figure 2.19: The mass gain results for oxidation of Fe–Ni–Cr alloys in pure oxygen at 1000 °C for 100 hours [43].

Fe-Cr-Al

The main feature of Fe-Cr-Al alloys is the formation of a protective alumina layer at very low aluminum contents. It can be seen in Figure 2.20 that when having around 20 wt% Cr in the alloy, the α-Al_2O_3 phase can form with only 3 wt% Al. However, in Fe–Al binaries, more than 7 wt% aluminum is required for the alumina to form. It is also shown by Pint et al. [129] through the experiments.

The oxidation kinetics of Fe–Cr–Al alloys differ greatly depending on their composition as a result of the variable diffusion properties of the oxide phases. In more dilute alloys the oxidation is usually more rapid because of the formation of an iron-rich oxide layer on top of the scale, or internal oxide precipitates. The oxidation is slower because of chromia scale formation in alloys with high amounts of Cr and low Al levels. An increased amount of Al (to around 5 wt%) causes the formation of a continuous alumina scale which considerably slows down the oxidation [181].

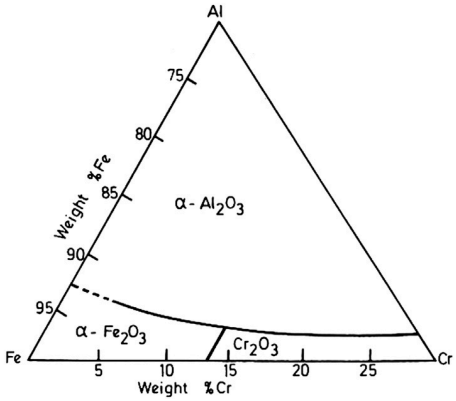

Figure 2.20: The oxide phase diagram for Fe – Cr – Al alloys at temperatures above 1000 °C [155].

Minor components effect

Si. The stability of SiO_2 is substantially greater than that of iron oxides (see Figure 2.11), but the effects of Si vary depending on the third element present. For instance, in the presence of Al, the more stable oxide (Al_2O_3) forms and silicon remains unreacted in the alloy. Furthermore, silica is more stable than chromia, so when Cr and Si co-exist in an oxidizing alloy, silica can form internal precipitates or an external scale beneath the chromia scale. This silica layer can act as a diffusion barrier and slow down the oxidation rate [53]. In any case, the presence of silicon can change the diffusion properties within the alloy.

Mn. even though manganese oxide is more stable than chromia, it does not form a layer under the latter because Mn is soluble in Cr_2O_3 [113], and it diffuses quickly in chromia [98] but rather slowly in the alloy. This results in a depletion of Mn in the alloy below the oxide/metal interface which explains the absence of MnO layer formation.

All in all, Wagner's diffusion-based models can be useful in predicting the HT oxidation of alloys. But the simplifying assumptions such as ignoring effects such as grain boundary diffusion, the impact of internal precipitates on diffusion, the microstructure, the volume change, scale spallation, the shape of the precipitates, and the nucleation hinders their general use. Although they have a remarkable predictive ability for the oxidation kinetics of pure metals and several simple alloys, the modified models are still unable to accurately forecast the oxidation kinetics of more complex alloys. There are several reasons why it is highly challenging to develop kinetic models for such complex multi-component systems:

1. Lack of thermodynamic data
2. Lack of data on the diffusion of elements in oxides and alloys
3. Limited knowledge of the effect of internal precipitates on the kinetics of oxide scale growth

4. Lack of information about the effect of nucleation and growth of the precipitates on the oxidation kinetics.

5. Insufficient knowledge about the mechanisms occurring in some cases such as the presence of water vapor

2.6. Data-Driven Methods for Kinetics of Oxidation

Because of the complexity of the HT oxidation processes, alternative approaches are sought based on the analysis of experimental datasets. In recent years, such data-driven methods have been employed to predict material behaviors, including the HT oxidation of alloys [128, 122, 21, 153, 6]. Machine learning (ML) models use statistical algorithms to analyze and learn from large datasets to accurately predict material properties. The use of ML in predicting the HT oxidation kinetics of alloys has the potential to reduce experimental costs, accelerate the design of new alloys, and improve the accuracy of the predictions.

Despite the success of ML techniques in predicting HT oxidation kinetics of certain alloys [122, 21], its use is still rather limited. Mainly because large datasets needed to train the models are often unavailable for the different steel grades and oxidizing conditions. Accordingly, there are two distinct strategies for addressing this. The first approach involves compiling data from published literature [21, 29, 153, 99, 11], and the second approach involves generating a dataset by conducting experiments under specific conditions [122, 128, 48, 84]. The former approach can predict a wider range of features but with lower precision due to the availability of data for many different conditions in the literature. The latter approach, on the other hand, is restricted to specific conditions, which allows for highly accurate predictions.

In the domain of HT oxidation of metals, ML studies follow a basic structure. There is a target value, which is the parameter being predicted, a set of features, which are the parameters considered that influence the target value, the ML algorithms themselves, which are designed to predict the target value based on the features, and error metrics that assess the accuracy of the predictions. As a result, the models are trained using the relationship between the features and the target values found in the dataset and can forecast the target value for new data based on the data used as input for training. As a result, the larger the dataset and the more accurate the selection of influential features, the better the prediction will be.

There are several ML algorithms that can be employed in data-driven works. Linear Regression (LR) [55] is among the most frequently employed algorithms and is well-liked for its ability to predict numerical values by assuming a linear correlation between the input features and the output variable. Polynomial Regression (PR) [154] extends LR by fitting higher-degree polynomial functions to the data. Random Forest (RF) [76] is an ensemble learning algorithm that combines multiple decision trees to improve predictive performance. *k*-Nearest Neighbors (KNN) [7] is a non-parametric algorithm that uses the similarity of neighboring data points to make predictions. Support Vector Machine (SVM) [13] is

a regression algorithm that uses a kernel function to map the input data into a high-dimensional space, where an LR model is applied. Artificial Neural Network (ANN) [20] is a deep learning algorithm that consists of multiple layers of interconnected nodes, inspired by the structure of the human brain, and is capable of learning complex patterns in data. These algorithms have various strengths and weaknesses, and the choice of algorithm depends on the specific problem and the characteristics of the data.

Various metrics can be used to assess the performance of ML algorithms, including Mean Absolute Error (MAE), Mean Squared Error (MSE), Root Mean Squared Error (RMSE), and Coefficient of Determination (R^2), as presented in Equations (2.25) to (2.28) [41].

$$\text{MAE} = \frac{\sum_{k=1}^{n} |\hat{y}_k - y_k|}{n} \tag{2.25}$$

$$\text{MSE} = \frac{1}{n}\sum_{k=1}^{n} (y_k - \hat{y}_k)^2 \tag{2.26}$$

$$\text{RMSE} = \sqrt{\frac{\sum_{k=1}^{n} (\hat{y}_k - y_k)^2}{n}} \tag{2.27}$$

$$R^2 = 1 - \frac{\sum_{k=1}^{n} (y_k - \hat{y}_k)^2}{\sum_{k=1}^{n} (y_k - \bar{y})^2} \tag{2.28}$$

where y_k = measured value, $\hat{y}_k$ = predicted value, $\bar{y}$ = mean value, and n = number of data points.

There are recent works on training the ML models with collected published experimental data on HT oxidation of metals in order to predict k_p. Mostly Wagner's kinetic model is considered to govern the HT kinetics, and the parabolic growth rate constant, k_p, is used to describe the rate of oxidation. Taylor et al. [153] conducted one of the limited studies on the kinetics of HT oxidation in iron-based alloys. They collected data on parabolic rate constants (k_p) for 75 alloys including low- and high-Cr ferritic and austenitic steels exposed to temperatures ranging from 500 to 1700 °C in various environments. They removed the effect of temperature in their models using an Arrhenius plot (1000/T in Kelvin vs log k_p in g2/cm4s); see Figure 2.21. Therefore, the target value was the activation energy, ΔE_a, for oxidation as in Equation (2.29).

$$k_p = A exp\left(-\Delta E_a / RT\right) \tag{2.29}$$

For simplification, they wrote Equation (2.29) for activation energy (expressed by m) with different selections of $c = \log_{10} A$ varied between 0 and +20, as

$$m = \left(log_{10} k_p - c\right) / \left(1000/T\right) \tag{2.30}$$

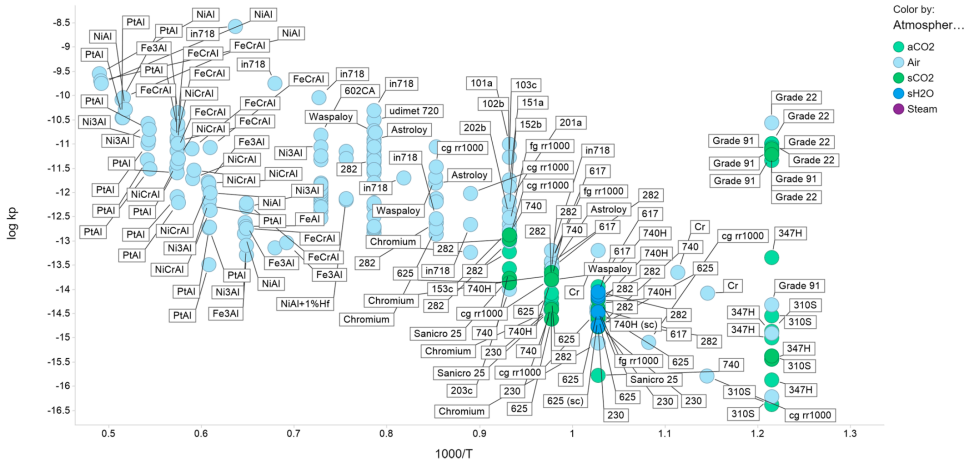

Figure 2.21: Arrhenius plot for the collection of alloys curated from the HT oxidation literature [153].

Several ML models, including LR, RF, ANN, KNN, SVM, and Single Decision Tree [132] were employed in Taylor's work. The accuracy of the predictions was assessed using four different indices: MSE, RMSE, MAE, and R^2. Finally, Ni, Cr, Al, and Fe were found to be the most important features in oxidation kinetics, although Mo and Co composition were also significant factors. The predicted (via RF model) vs actual values of m are shown in Figure 2.22 for $c = 0$, where an R-squared of 0.83 was achieved. However, it is evident based on Figure 2.21 that the models lack sufficient training data for oxidation in atmospheres other than air. Furthermore, when the environment is not explicitly reported in the sourced data, it is assumed to be air. These factors have the potential to confuse the ML models, resulting in less accurate predictions.

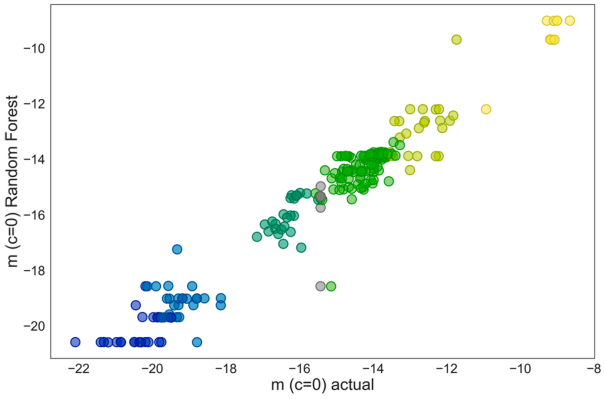

Figure 2.22: Parity plot of m values predicted by random forest vs actual values, assuming $c = 0$ [153].

As previously stated, many ML studies on HT oxidation utilize k_p as the target value. However, this can be misleading due to the fact that the growth kinetics of oxide is not always parabolic. In the research work by Anirudh et al. [11], time was incorporated as a feature and the target value was the mass gain in this case. This allows for the unraveling of different growth mechanisms over time. Using previously published data, different ML models were employed to predict the mass gain in cyclic oxidation of binary Fe–Cr alloys and ternary Fe–Cr–Ni alloys between 650 and 800 °C in the air + 10% water vapor atmosphere.

Moreover, a CatBoost classifier model [131] was employed to predict the type of oxidation behavior after one hundred hours of cyclic oxidation, for a given composition. These behaviors were divided into three categories: Protective oxide scale (POS), Accelerated attack without spallation (AA), and with spallation (AAS). In this context, "accelerated attack" specifically denotes the phenomenon of rapid oxidation. Finally, the regression model accurately predicted ($R^2 = 0.99$) the mass change after cyclic oxidation of the binary (Fe-Cr) and ternary (Fe-Cr-Ni) alloys with varying chromium and nickel concentrations. Besides, the oxidation behaviors POS, AA, and AAS were predicted by the multiclass classification model (CatBoost) with a probability over 91%.

In fact, most of the research using ML has been done on predicting the HT oxidation kinetics of non-iron-based alloys. The kinetics of cyclic oxidation was successfully predicted for NiCr-based alloys by Peng et al. [122]. Dewangan et al. [48] employed ANN to predict the HT oxidation behavior of $AlCrFeMnNiW_X$ (X = 0, 0.05, 0.1, 0.5) high entropy alloys precisely ($R^2 > 0.999$). They also considered time as an input feature as well as the alloying elements. The advantage of having time as a feature is to predict the whole mass gain curve instead of only the fitted parabolic constant (k_p) since the curve is not always fully parabolic. Furthermore, a statistical (machine) learning model was also developed by Somesh et al. [21] to forecast the parabolic rate constant (k_p) for the cyclic and isothermal HT oxidation of Ti alloys. They took a broader variety of input features into account, including the alloy composition, constituent phase of the alloy, the temperature of oxidation, time of oxidation, oxygen, and moisture content, remaining atmosphere (gas except O_2 in a dry atmosphere), and mode of oxidation testing. Among the regression models they utilized, the gradient-boosting regressor produced an R-squared value of 0.92. All in all, it is shown that HT cyclic oxidation kinetics of alloys can be predicted accurately via ML methods.

Although utilizing ML models to examine the kinetics of HT oxidation is a relatively new area of research, it offers distinct benefits over traditional predictive models in this domain. An advantage of ML models is their ability to enhance accuracy by incorporating numerous features, which was previously unachievable. Additionally, ML models can streamline the material design process by decreasing the cost and time of experimentation. There is also much potential to improve the use of ML in studying the HT oxidation kinetics of steels. Including additional features in the models, for instance, can improve their accuracy. Possible features for future research include gas composition and flow, sample size and roughness, grain size and orientation, pre-oxidation heat treatment, the possibility of

scale spallation/detachment, and void formation. Therefore, the development of more extensive data sets is necessary which can be achieved by conducting additional experiments or compiling data from different sources.

It should be noted that employing ML models has its drawbacks too. The most important one is the complexity of the models which can lead to misleading results if they are not appropriately understood. For example, having an overfitting model is one of the most common ones. Therefore, dealing with hyperparameters (parameters that are set before the learning process begins e.g. the number of hidden layers in ANN and the number of neighbors in KNN) is of great importance. Furthermore, ML models are based on statistical relationships between inputs and outputs. Thus, they may not provide a complete understanding of the underlying physical processes that govern the HT oxidation of steels. Finally, the development of ML models requires large amounts of data. However, in some cases, limited data may be available for the HT oxidation of steels, making it difficult to develop accurate models. So, the experiments are still pretty much needed for these models.

2.7. Summary and Future Directions

In this chapter, we have delved into various models and approaches for predicting the kinetics of HT oxidation in steels. We have explored the strengths and weaknesses of each model, shedding light on their capabilities and limitations in capturing the intricate processes of HT oxidation. This summary provides a consolidated assessment of the state-of-the-art in this field.

2.7.1. Assessment of Current Approaches:

In evaluating the current approaches to predicting the HT oxidation behavior of steels, we have explored various models and methodologies that offer unique insights into this complex phenomenon. Each approach has its own strengths and limitations, contributing to our understanding of HT oxidation behavior.

Analytical Models: Physics-based models have been instrumental in describing HT oxidation kinetics. The classic Wagner's kinetic model, for instance, describes the parabolic growth of an oxide layer during high-temperature oxidation. It uses a mathematical equation to represent the oxide growth rate based on diffusion principles and is used to predict the oxidation kinetics of pure iron. Such analytical models, rooted in fundamental principles of chemistry and physics, provide valuable insights into oxidation processes. While these models are versatile and capable of capturing various oxidation kinetics, they rely on simplifications and assumptions. Moreover, determining model parameters experimentally can be challenging, and the accuracy of predictions may vary based on data quality and underlying assumptions.

Numerical Models: One of the key takeaways from our exploration is the pivotal role played by Wagner's model in understanding HT oxidation kinetics. It provides a physics-based framework for understanding HT oxidation by considering the diffusion of reactants through oxide layers. Researchers have con-

sistently sought to enhance this model by considering additional influencing factors. By employing numerical solutions for the equations developed by Wagner, substantial improvements in model accuracy have been achieved. While such methods excel under well-defined conditions and offer valuable insights, they may fall short in their ability to predict HT oxidation kinetics in complex real-world scenarios. They often assume idealized conditions and may not account for the effects of multi-element alloys and varying gas compositions such as those containing H_2O and CO_2.

Data-Driven Approaches: Recent advancements in data-driven techniques, particularly ML models, have introduced a new dimension to predicting HT oxidation kinetics. ML models leverage statistical algorithms to analyze large datasets and predict material behaviors. They have shown promise in accurately predicting parameters like k_p and mass gain in cyclic oxidation. ML models are known for their ability to consider numerous features that were previously challenging to incorporate, offering the potential to enhance prediction accuracy. However, their effectiveness hinges on the availability and quality of training data. Limited data can compromise prediction accuracy, and ML models, if not managed properly, may exhibit overfitting. Furthermore, while they excel at prediction, they may not provide a comprehensive understanding of the underlying physical mechanisms governing HT oxidation.

In summary, our assessment of current approaches reveals a diverse landscape of models and methodologies used to predict HT oxidation kinetics in steels. Analytical models, such as Wagner's, originally developed for pure iron, provide valuable insights but have limitations when applied to alloys with specific alloying elements, as they often require separate model development. Both numerical and data-driven approaches necessitate experimental data, and in some cases, additional experiments may be required to generate the necessary datasets for accurate predictions. It's worth noting that, to our knowledge, there have been no ML-based studies specifically addressing the kinetics of HT oxidation in steels to date. As we move forward, it is essential to recognize the strengths and limitations of each approach and explore potential synergies to advance our understanding of HT oxidation in steels.

2.7.2. Pathways for Advancement:

Building upon this critical assessment of current approaches, it is clear that there are promising pathways to advance our understanding of HT oxidation in steels. Here, we outline concrete steps for future research:

Expanding the Scope of Data: To improve the accuracy of any model, it is imperative to gather extensive datasets. Experimental data play a pivotal role in these models, serving as input, validation data, or the foundation for constructing ML models. Achieving this entails ongoing experimentation or aggregating data from diverse sources. Moreover, there is room for improvement by including additional features, such as gas composition, gas flow rates, sample characteristics, and pre-oxidation heat treatment, to enhance the predictive capabilities of these models. As a result, continuous experimentation under various conditions

remains an ongoing necessity.

Tailored Numerical Models: To advance our understanding of HT oxidation in steels, it is crucial to develop customized numerical models that account for the diverse oxidation behaviors observed in different materials/conditions. The complexity of real-world problems requires specific models for accurate predictions.

Leveraging Experimental Data: Utilizing ML models on experimental data for HT oxidation of different steel grades represents a promising avenue for future research. This approach not only enhances predictive capabilities but also has the potential to contribute valuable insights into the mechanisms governing HT oxidation. It is worth mentioning that developing a predictive model for steels may necessitate experiments on specific alloys to ensure accuracy and relevance to real-world applications.

3

Initial High-Temperature Oxidation Behavior Of Fe-Mn Binaries In Air

High-temperature (HT) oxidation of steels can be relatively fast when exposed to air. Consequently, elucidating the effect of different parameters on the oxidation mechanism and kinetics is cumbersome. In this study, short-time oxidation was investigated to determine the oxidation mechanism, the affecting parameters, and the linear to parabolic growth transition of different Fe-Mn alloys in various oxygen partial pressures (10-30 kPa) and gas flow rates (26.6 and 53.3 sccm) in a temperature range of 950-1150 °C. Oxidation kinetics was investigated using a thermogravimetric analyzer (TGA) under a controlled atmosphere. Linear oxide growth was observed within the first 20 minutes of oxidation. The linear rate constant was significantly increased by increasing the oxygen partial pressure or the flow rate of the oxidizing gas. The morphology of the oxide layer was determined by scanning electron microscopy (SEM). The crystal structure of the oxides formed was followed by in-situ X-ray diffraction (XRD), confirming that the growing layer consists of wustite mainly, which upon slow cooling to room temperature, transformed into magnetite. Energy-dispersive X-ray spectroscopy (EDS) showed that the atomic ratio of Fe+Mn to O was ≈1.03:1 in the oxide scale, corresponding to Fe(Mn)O formation. Based on the characterization and a model for linear growth kinetics, it is concluded that the oxidation rate is controlled by the diffusion of oxidizing molecules through the gas layer to the sample's surface. The findings led to a better understanding of initial oxidation behavior and provided a pathway for improved insight into the HT oxidation behavior for more complex alloys.

This chapter has been published in [4] by S. Aghaeian, W.G. Sloof, J.M.C. Mol, and A.J. Böttger, "Initial High-Temperature Oxidation Behavior of Fe–Mn Binaries in Air: The Kinetics and Mechanism of Oxidation." Oxidation of Metals 98, no. 1-2 **(2022)**: 217-237.

3.1. Introduction

Oxidation at high temperatures is a critical topic in metallurgical processes such as steelmaking. The steel is often hot at various processing stages during production, and if oxygen is present, oxidation can start. For example, during hot rolling, the steel sheets are heated up for better formability. Consequently, fast oxidation is inevitable since the sheets are in contact with oxidizing gases such as air and water vapor at high temperatures (around 1000 °C).

This oxidation reaction can change the substrate alloy composition and affect some properties that depend on the alloying element content. Furthermore, the oxide scale's characteristics such as thickness can vary depending on the oxidation condition. This would lead to different defects on the sheets' surfaces at further steps in production, such as coating. For example, the presence of oxide scale at the surface can reduce the wettability of liquid zinc [146], and decrease the adhesion between zinc coating and steel substrate. Therefore, understanding and predicting the initial oxidation stage at different conditions is essential.

The progress of oxidation of metals is commonly measured through the mass change or scale thickness per unit surface area of the sample. There are two main regimes in mass change versus time plots: linear and parabolic [181]. Oxidation typically begins with rapid linear growth of the oxide scale. Then, after reaching a specific scale thickness the oxide grows parabolically [124, 35].

At the beginning of oxidation, the diffusion through the oxide layer is, in general, not the rate-limiting step because the species diffuse rapidly through the thin scale. Therefore, two other phenomena could control the process: (a) The surface reactions [96, 142, 123, 26, 178], and (b) the diffusion of the oxidizing molecules in the gas phase [36, 2, 178, 171]. In both cases, the oxide growth is linear. In the oxidation of iron, wüstite is the only oxide phase that can form within the linear regime [181]. As the oxide scale gets thicker, the diffusion of species in the metal phase becomes slower and limits the oxidation rate. This means that the other iron oxide phases, such as magnetite and hematite, start forming, [182, 38, 180].

The oxygen partial pressure of the atmosphere can significantly influence the reaction kinetics. Lashgari et al. [95, 94] showed that oxidation of Mn-steel alloys at low dew point (-45 to +10 °C) and a temperature of 950 °C led to the formation of only manganese oxide (MnO). Oxidation for more than 4 hours in such conditions followed a parabolic growth and was dependent on the diffusion of the species through the matrix. In such cases, the concentration of manganese in the alloy affects the kinetics. Mayer and Smeltzer [108] exposed Fe-Mn alloys to carbon dioxide-carbon monoxide atmospheres with equilibrium oxygen partial pressures of between 8×10^{-15} and 8×10^{-11} atm. for more than 10 hours. They also observed a parabolic growth based on the mass-gain data during the oxidation.

Wikström et al. [171] studied the effect of oxygen content and temperature on the initial HT oxidation behavior of different steels. They showed that increasing the amount of oxygen in the furnace chamber resulted in higher linear growth-rate constants, while the effect of temperature was negligible. Finally, they con-

cluded that the oxidation at the initial stage is controlled by the mass transfer in the gas phase. However, they did not consider the effect of gas flow rate nor the dwell time of the gas on the metal's surface. For low alloyed steels, Yin et al. [178] observed that at 800 °C, the oxidation rate is initially limited by the mass transfer in the gas phase. The effect of different parameters such as the oxidizing gas flow rate were considered, and the experiments were conducted at low oxygen partial pressures where only wüstite is stable enough to form within the oxide layer.

Extensive research has been carried out on HT oxidation of steels during annealing where the oxygen partial pressure is low, and the exposure time is long. However, only a few studies have investigated the short-time HT oxidation behavior of pure Fe-Mn binaries in gases with variable oxygen partial pressures. It has been done mostly on complex steels in the air, making it difficult to separate the effect of different alloying elements and parameters such as oxygen partial pressure and gas flow rate. Therefore, the initial oxidation of pure binaries at different conditions is still not fully understood.

In this paper, the initial HT oxidation behavior of iron-manganese alloys is investigated. In particular, the effect of different parameters are separated and the rate-limiting steps and oxidation mechanism in the early oxidation stage are determined. The process starts with the diffusion of the oxidizing molecules to the alloy surface and ends with the reaction between species. The HT oxidation experiments were conducted in a TGA (thermogravimetric analyzer) to obtain the mass gain data. Gas mixtures containing high amounts of oxygen with different flow rates were applied. The oxide layer morphology and composition was studied using scanning electron microscopy (SEM), combined with X-ray microanalysis using energy-dispersive spectroscopy (EDS) and X-ray diffractometry (XRD).

3.2. Experimental Procedures

3.2.1. Samples and preparation

Alloys with different concentrations of Mn as the main alloying element were provided by ChemPur (Karlsruhe, Germany). Table 3.1 shows the chemical composition of the pure iron and alloys with 1, 3, and 5 percent manganese as obtained with inductive coupled plasma-optical emission spectrometry (ICP-OES). Samples were cut into pieces of 2 × 8 × 15 mm with a hole of 2.2 mm diameter by electric discharge machining (EDM). All the surfaces were ground using SiC emery paper and then cleaned ultrasonically in isopropanol. Finally, the specimens were dried with a flow of pure nitrogen and stored in airtight membrane boxes (Agar Scientific, G3319, Essex, UK).

3.2.2. Oxidation Process and Analyses

The experiments were carried out in a symmetrical thermogravimetric analyzer (TGA, Setaram TAG 16/18, Caluire, France) to get continuous mass-gain data. The specimen was hanging through its hole in the first furnace chamber. Additionally, there was a dummy sample of alumina in the second furnace to eliminate the buoyancy effect. The furnace chamber was a tube with 280 mm length and the

Table 3.1: Chemical composition of the alloys obtained with ICP-OES.

Sample	Elements (wt.%)				
	Mn	Si	Al	C	Cr
Pure Fe	0.0011	0.0002	0.0003	0.0055	0.0001
Fe-1Mn	1.0300	0.0010	0.0012	0.0157	0.0026
Fe-3Mn	2.8450	0.0014	0.0002	0.0002	0.0002
Fe-5Mn	5.3200	0.0020	0.0003	0.0031	0.0110

diameter of 18 mm. To start, the TGA system was pumped to vacuum (< 50Pa), then the gas lines, balance, and the furnace were flushed with pure nitrogen. The purity of nitrogen was 5N vol.% and was filtered to remove any residual hydrocarbons, moisture, and oxygen, with Accosorb (< 10 ppb hydrocarbons), Hydrosorb (< 10 ppb H_2O) and Oxysorb (< 5 ppb O_2) filters (Messer Griesheim, Germany), respectively.

Next, the dual furnaces were heated up with a rate of 10 °C/min in pure nitrogen again. 5 target temperatures were chosen between 950 and 1150 °C. After reaching the target temperature, the chamber's atmosphere was switched to oxidizing by introducing an oxygen/nitrogen gas mixture. Different flow rates of 26.6 and 53.3 sccm (Standard Cubic Centimeters per Minute at standard condition of 0 °C and pressure of 1.01 bar) and oxygen partial pressures (10 to 30 kPa) were applied by changing the ratio between O_2 and N_2 gases, while the total chamber pressure was kept at 101 kPa (1 atm). After an exposure time of 20 minutes, the furnace tube was flushed with pure N_2 and cooled down to room temperature with a rate of 10 °C/min.

Figure 3.1 shows the temperature profile and the mass gain per unit area for an oxidation experiment in the TGA system. The mass gain data is assumed to correspond to the total weight of oxygen consumed by the metal to form the oxide scale and is used to determine the thickness of the oxide scale.

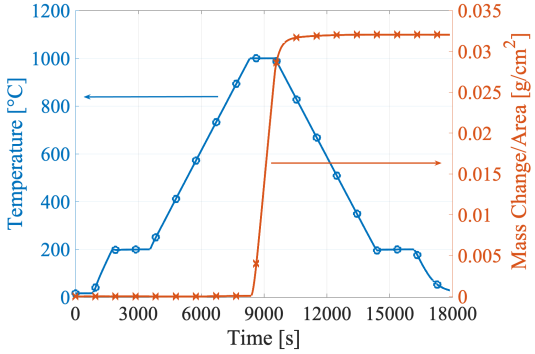

Figure 3.1: The mass gain data and temperature profile for oxidation of Fe-5Mn at 1000 °C at oxygen partial pressure of 20 kPa with a gas flow rate of 53.3 sccm.

X-ray diffraction, on oxidized samples, was conducted to identify the oxide

phases that were formed during the oxidation experiments. The XRD patterns were recorded with a D8 Advance diffractometer (Bruker, USA) in the Bragg-Brentano geometry using Cu Kα radiation and a Lynxeye position-sensitive detector. A 2θ region between 20 to 100 ° with a step size of 0.030 ° 2θ and a dwell time of 2s was applied.

The surface and cross-section of the oxidized alloys were observed using a Helios UXe Dual Beam G4 PFIB SEM (Thermo Fisher Scientific, USA). Energy Dispersive Spectroscopy (EDS) was performed with a JSM-6500F (JEOL, Japan) operated with an accelerating voltage of 15 kV and equipped with an UltraDry 30mm^2 detector (Thermo Fisher Scientific, USA) to determine the chemical composition of oxides qualitatively. To prepare the cross-section, the oxide surface was embedded in an epoxy resin (G2 epoxy resin, Gatan 601.07270, UK) and covered with a silicon wafer. Then, the specimens were embedded in fast-curing acrylic cold mounting resin (ClaroCit Kit, Struers, Denmark) -to protect the scale- and ground using SiC emery paper and then cleaned ultrasonically in isopropanol.

In-situ HT XRD experiment was performed to follow the phases formed during oxidation upon heating and cooling. The sample for this experiment was a sheet of 7.2 × 8 mm and thickness of 1 mm. Then it was clamped in the Anton-Paar DHS1100 high-temperature stage and measured at the center position. The experiments were carried out using a D8 Discover diffractometer (Bruker, USA) using Cu Kα and Eiger-2 500k 2D-detector radiation. The 2θ region was chosen to be between 22 to 55 ° with a step size of 0.05 ° 2θ and a dwell time of 1s. The oxidizing condition was the same as in the TGA. The alloy was heated up in nitrogen, and at the desired temperature the oxygen partial pressure of the chamber increased to 20 kPa for 20 minutes. Finally, the sample was cooled down in pure nitrogen. Scans were recorded at set temperatures: room temperature, 500, 900, and 1000 °C during heating as well as cooling.

3.3. Results

The alloys were oxidized in a TGA with a controlled atmosphere where the mass change was measured continuously. Figure 3.2 shows the mass gain per unit area $\Delta m/A$ (surface area was 3.32 cm^2) as a function of time. The growth was mostly linear ($R^2 > 0.99$ for all the lines) within the first 20 minutes of oxidation in 10 to 30 kPa oxygen with the gas linear flow rates of 26.6 and 53.3 sccm. The slope of the line in this linear part was measured to be the linear kinetic constant k_l. The initial curve in the mass gain is related to switching the atmosphere from pure N_2 to the mixture of N_2 and O_2. Therefore, the time zero for Figure 3.2 is determined when the first signs of mass gain were observed. However, to get more precise linear rate constants, the initial part of the mass gain data was not considered. Furthermore, an increase in the gas linear flow rate or oxygen partial pressure increased the mass gain during oxidation. This means a higher linear rate constant which led to the transition to parabolic growth in some cases.

The samples with 5 wt% Mn were oxidized in 20 kPa oxygen with a gas linear flow rate of 53.3 sccm at different temperatures (between 950 and 1150 °C) to determine the activation energy. Figure 3.3 shows the logarithm of the measured

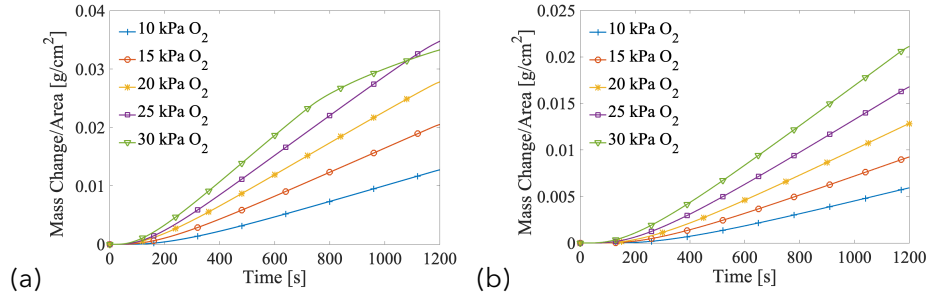

Figure 3.2: The mass gain data for 20 minutes of oxidation of Fe-5Mn binary alloys at 1000 °C in 10 to 30 kPa oxygen with the total gas linear flow rate of (a) 53.3 sccm and (b) 26.6 sccm.

linear rate constant versus the reciprocal of the absolute temperature, approximated by a straight line. The activation energy of 2 kJ · mol^{-1} ± 1 kJ · mol^{-1} was obtained, which is a typical value for an oxidation process controlled by the gas phase diffusion [171].

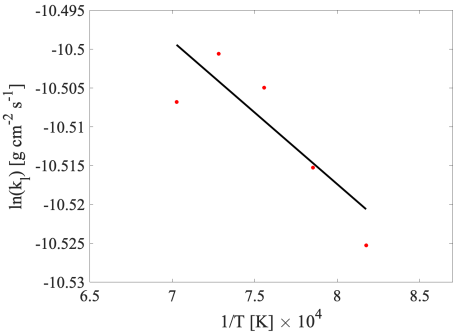

Figure 3.3: Dependence of the linear rate constant on the temperature for oxidation of Fe-5Mn in 20kPa at a constant gas linear flow rate of 53.3 sccm. The calculated activation energy is approximately 2 kJ · mol^{-1} ± 1 kJ · mol^{-1}.

To study the effect of the alloy composition on the oxidation kinetics, pure iron, and samples with 1, 3, and 5 %wt Mn were used. The specimens were oxidized at 1000 °C for 20 minutes in 20 kPa oxygen with the gas linear flow rate of 53.3 sccm. The linear rate constants were measured 2.75×10^{-5}, 2.73×10^{-5}, 2.73×10^{-5}, and 2.72×10^{-5} ± 0.1 gcm^{-2}s^{-1}, respectively for pure iron and alloys with 1, 3, and 5 wt% of Mn. Therefore, the effect of the alloy composition was found to be negligible.

The oxidized samples were analyzed with XRD and SEM. The XRD patterns obtained at room temperature after the TGA experiments, showed the presence of all iron oxide phases (wüstite, magnetite, and hematite), with magnetite as the main oxide phase present. Moreover, most of the oxidized samples showed a non-uniform surface, varying from the top to the bottom. This is related to the laminar boundary layer's width formed on the surface of the sample which causes

different roughnesses on the sample and is discussed in more detail in Section 3.4 (see Figure 3.4).

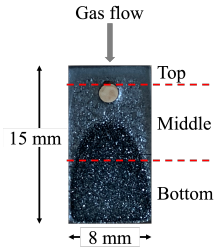

Figure 3.4: The surface of the alloy with 5 wt% Mn oxidized at 1000 °C with a gas linear flow rate of 53.3 sccm and oxygen partial pressure of 20 kPa.

This roughness difference is shown in more detail in the surface SEM images of the samples oxidized at the lowest and highest oxidizing conditions (Figure 3.5). The sample oxidized with the gas linear flow rate of 53.3 sccm in 30 kPa, had a loose oxide scale that was separated from the substrate alloy, SEM imaging was not possible.

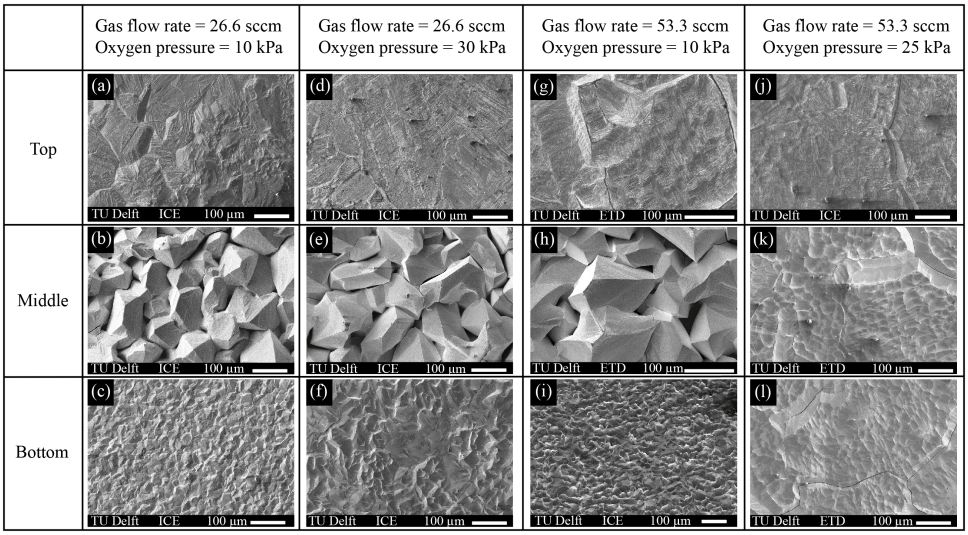

Figure 3.5: SEM images from different spots (top, middle, and bottom) on the surface of the alloy with 5 wt% Mn oxidized at 1000 °C with a gas linear flow rate of 26.6 and 53.3 sccm and oxygen partial pressures from 10 to 25 kPa.

After the surface characterization of the samples, the cross-sections of the oxide scales were also analyzed. Figure 3.6, shows the oxide scale profile at different spots on the samples (top, middle, and bottom). Large differences in oxide thickness can be seen from bottom to top on most of the samples. For instance,

the average oxide thickness ratio for the alloy shown in Figure 3.6 (a),(b), and (c) was 10.6: 2.4: 1, for top to middle to bottom.

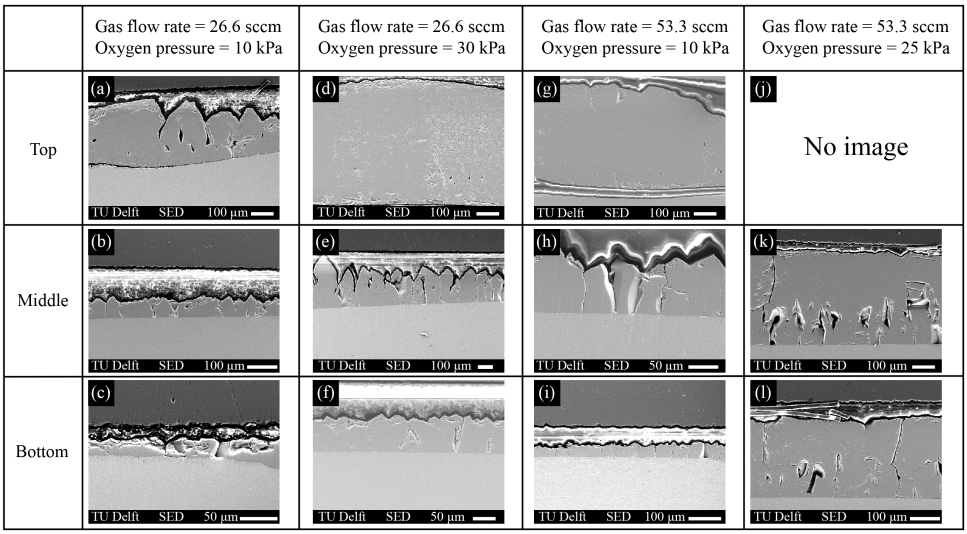

Figure 3.6: Cross-section SEM images from the different spots (top, middle, and bottom) of the alloy with 5 wt% manganese oxidized at 1000 °C with a linear gas flow rate of 26.6 and 53.3 sccm and oxygen partial pressures from 10 to 30 kPa.

Figure 3.7 is a phase diagram, obtained by using Factsage software [16], showing the thermodynamically stable phases possible to form in the current work's experimental condition. The thermodynamic data corresponds to oxidation at 1000 °C. All in all, the phase diagram shows that all the oxide phases are thermodynamically stable in the experimental conditions applied in this work. In addition, it shows that FeO and MnO are the most stable ones, and are the first ones to form. It means that these two oxide phases are at the metal/oxide interface. Additionally, it shows that FeO and MnO are entirely miscible and could form a continuous solid solution with the rock salt cubic structure.

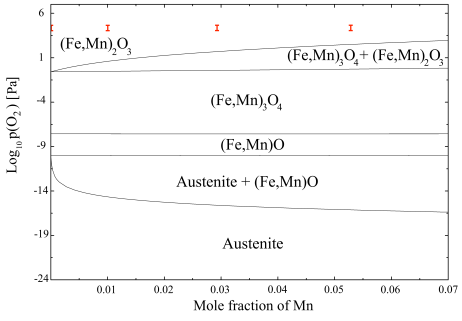

Figure 3.7: Stability regions of different iron and manganese oxide phases as a function of Mn mole fraction and oxygen partial pressure at 1000 °C, obtained by using Factsage software [16]. The red marks show the experimental condition of this work.

An in-situ XRD experiment was conducted to identify the oxide phases forming at each stage of the oxidation. Figure 3.8 shows the XRD patterns at different times and temperatures. At room temperature, only ferrite was observed. Then,

the sample was heated in nitrogen with only small amounts of impurities such as oxygen. Accordingly, at 500 °C, there were traces of oxide phases. At 900°C during heating, the ferrite to austenite transformation occurred and diffraction peaks of wüstite were detected. Then, at 1000 °C, the metal substrate was entirely austenite, and no peaks for magnetite and hematite could be observed. After 20 minutes of oxidation, when cooling down in nitrogen, the XRD pattern at 900 °C showed wüstite still as the only oxide phase. It also showed the austenite to ferrite transformation in the substrate. Since wüstite is not thermodynamically stable below 570 °C, by reaching 500 °C, the pattern showed the partial transformation of wüstite into magnetite and ferrite. Finally, at room temperature, the oxide scale consisted mainly of magnetite, and only little peaks of wüstite were seen.

Figure 3.9 shows the EDS mapping results of the sample with 5 wt% Mn oxidized at 1100 °C in 20 kPa oxygen with a linear flow rate of 53.3 sccm. The EDS results show that the oxide scale contains Fe, O, and Mn, 47.3, 49.1, and 3.6 at.%, respectively.

3.4. Discussion

The initial linear growth of the oxide scale at all oxidation conditions is shown in Figure 3.2. The transition from linear to parabolic regime was seen for the samples oxidized in 25 and 30 kPa oxygen with a linear flow rate of 53.3 sccm. This linear part of the oxidation before the parabolic growth is observed many times in previous works by different authors [36, 2, 96]. The mechanism that controls the oxidation within the parabolic regime is known to be the diffusion of species in the solid phase. However, in the initial stage of the reaction, there is only a thin scale of wüstite in which diffusion is fast. Therefore, the oxidation rate is limited by either the surface reactions or the gas phase diffusion. To identify the mechanism of oxidation, the effects of different parameters were studied.

Measurements showed that increasing the Mn concentration of the alloys from zero to 5 wt% did not change the results substantially. Moreover, Figure 3.7 shows that FeO and MnO can form a continuous wüstite solid solution in the whole range of Mn concentration. Both FeO and MnO have the cubic crystal lattice (rock salt), which is expected to be the main phase in the oxide scale. This can explain the very close linear rate constant values for pure iron and the Fe-Mn alloys studied in this work. It is shown in [93] that increasing the amount of oxygen in the chamber causes the Fe/Mn ratio in the oxide layer to increase. Hence, this explains the negligible effect of Mn concentration on oxidation of alloys at high oxygen partial pressures and is in agreement with previous findings in the literature [179, 88].

The oxidation kinetics was also unaffected by the temperatures applied in this work (between 950 and 1150 °C) (Figure 3.3). An activation energy of around $2 kJ \cdot mol^{-1}$ was measured, which is comparable to values found in literature [36, 171, 96, 2]. When the oxide growth follows a linear regime, a low activation energy (between zero and 20 kJ) indicates that gas phase diffusion is the rate-controlling step. But, when surface reactions control the oxidation, the activation

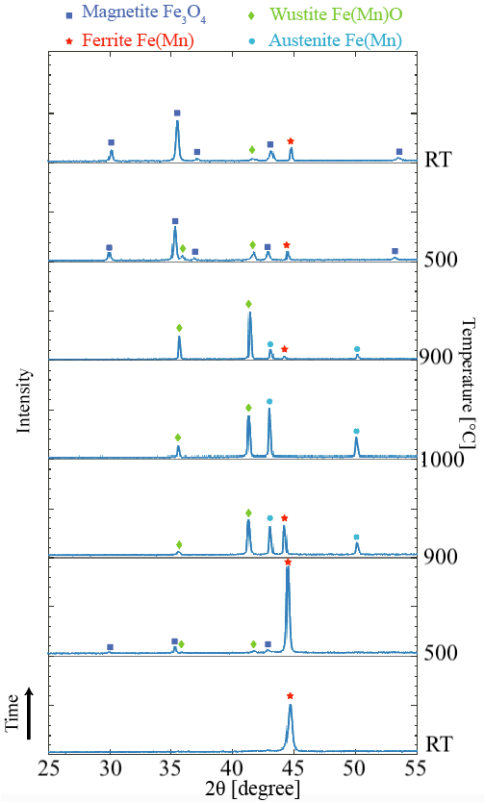

Figure 3.8: In-situ XRD results for the alloy with 5 wt% Mn during heating from room temperature to, 500 °C, 900 °C, 1000 °C and during cooling at 900 °C, 500 °C, and room temperature. Oxidation occurs at 1000 °C for 20 minutes in the presence of a gas mixture including oxygen and nitrogen with partial pressures of 20 kPa and 80 kPa, respectively.

energy is found to be larger than 80 kJ [3, 178]. Furthermore, higher activation energies (> 140 kJ) relate to solid-phase diffusion control [31]. Accordingly, the low temperature sensitivity of the activation energy supports the idea of an oxidation process controlled by the gaseous mass transfer.

All in all, the amount of oxygen in contact with the sample surface was the most influential parameter on the oxidation kinetics. That can be controlled by changing the oxygen partial pressure and/or the oxidizing gas linear flow rate in the chamber. Increasing any of those parameters led to an increase in the linear rate constant. If the oxidation process was limited by the diffusion rate of the species within the solid or if the reaction rate between iron/manganese and oxygen was slow, neither the oxygen partial pressure of the bulk gas nor the gas linear flow rate could play a role in the kinetics. This also points to oxygen diffusion through the gas layer as the rate-controlling step. The same pattern was seen in the literature on linear growth of the oxide layer for low-carbon steels

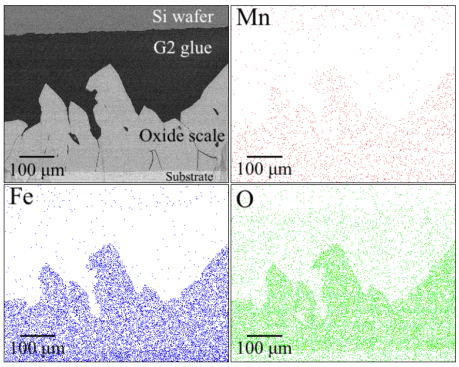

Figure 3.9: Cross-sectional SEM image and EDS mapping results of alloy with 5 wt% Mn oxidized at 1100 °C with gas linear flow rate of 53.3 sccm and oxygen partial pressure of 20 kPa.

when gas diffusion was the controlling step during oxidation [2, 35].

The roughness of the oxide scale reflects the mechanism of oxidation [96, 36]. Figure 3.5 shows the SEM images taken from different spots on the surface of samples oxidized at different conditions. It can be seen in the images from the top part of the samples (Figure 3.5(a, d, g, and j)) that the surface is more smooth compared to the other ones. Whereas, in the first three images from the middle part, massive grains are observed and the surfaces are extremely rough; see Figure 3.5(b, e, and h). The first three images from the bottom part (Figure 3.5(c, d, and i)) also show rough surfaces but not as rough as those from the middle. Furthermore, Figure 3.6 shows the SEM images on the cross-sections of the samples in different spots from top to bottom. It can be seen that for all the oxidizing conditions, the oxide scale on top is between 7 to 10 times thicker compared to it on the bottom, and the oxide on the middle is between 1.5 to 3 times thicker than on the bottom. Therefore, it can be concluded that the rough surface pertains to a thinner oxide scale and the smooth surface to the thicker scales.

During the first 20 minutes of oxidation, when the oxide scale is following a linear growth regime (see Figure 3.2), the amount of oxygen consumed by the alloy is constant over time. This means that the oxidation rate is independent of the thickness of the oxide scale. Local thickness variations are related to the grain orientations, which leads to a rough surface. Furthermore, when there is a laminar flow over a flat surface, a boundary layer forms which has a width of almost zero at the leading edge and it is wider at the trailing edge [35]. So, diffusion of gas through this layer is easier at the leading edge. Therefore, different thicknesses and roughnesses on different spots (top, middle, bottom) of the oxidized samples are related to the width of the laminar boundary layer formed across the surface of the sample, when gaseous diffusion is the controlling step. Also after the set time of 20 minutes of oxidation, it took some time for the chamber atmosphere to switch back to pure nitrogen. This caused further oxidation. Figure 3.10 shows the mass gain data and indicates when the gas atmosphere was switched from inert to oxidizing and vice versa.

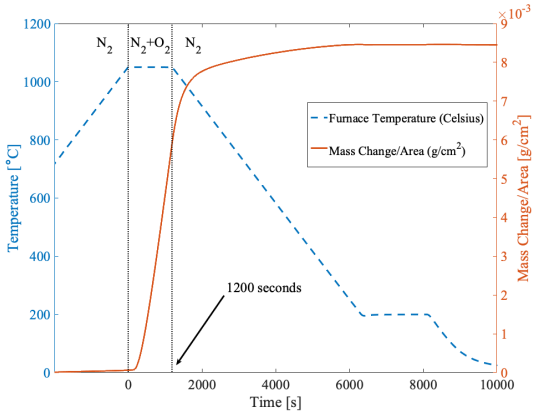

Figure 3.10: The total mass gain data for oxidation of Fe-5Mn binary alloy at 1000 °C in the presence of 10 kPa oxygen partial pressure with a gas linear flow rate of 26.6 sccm. The vertical dotted lines show the 20 minutes of isothermal oxidation and indicate when the gas atmosphere is switched from inert to oxidizing and vice versa.

Moreover, the samples which were oxidized in 25 and 30 kPa oxygen with a linear flow rate of 53.3 sccm, showed parabolic growth during the last minutes of oxidation (Figure 3.2). It can be seen in the SEM images of the surface (Figure 3.5 (k and l)) that the oxide scale is not as rough as in the other images. This is also an indicator of parabolic growth of the oxide scale. Additionally, in the images of the cross-section of the same sample it can be seen that the oxide thickness on the bottom is almost equal to that at the middle part (see Figure 3.6 (k and l)). This is due to the parabolic growth of the oxide layer on this sample which was seen in the mass-gain data. So, SEM images from the surface and the cross-section showed a thick and smooth scale which indicates the parabolic growth regime and solid-phase diffusion mechanism.

However, the kinetic data from the first 20 minutes of oxidation shows that the gas phase diffusion controls the oxide scale growth. HT in-situ XRD measurement (See Figure 3.8) showed wüstite as the only oxide phase present at 1000 °C during oxidation. The formation of magnetite only occurred during cooling down and at temperatures where wüstite is not thermodynamically stable. Moreover, the EDS analysis showed that the atomic ratio of Fe + Mn to O within the oxide layer was around 1.03:1, corresponding to Fe(Mn)O formation (see Figure 3.9). The weight fraction of Mn within the oxide layer was almost the same as it was in the substrate alloy (around 5 wt%).

All in all, wüstite was the main oxide phase present in the oxide scale during the first 20 minutes of oxidation. Moreover, based on the previously shown results, it is concluded that the gas-phase diffusion is the controlling mechanism. Also, the gas-phase diffusion is considered for the model in the work by Abuluwefa [2]. Next, the kinetic constants measured in this work were compared with the ones calculated via this model. If the gaseous mass transfer limits the oxidation rate, then the linear rate constant k_l ($gcm^{-2}s^{-1}$)can be calculated through

Equation (3.1).

$$k_l = M_O k_{MTC} \left(C^G_{O_2} - C^*_{O_2} \right) \tag{3.1}$$

M_O is the molar mass of atomic oxygen (g/mol). $C^G_{O_2}$ and $C^*_{O_2}$ are the molar concentrations of oxygen in the gas mixture at the bulk of the gas and at the sample surface, respectively. k_{MTC} is the mass transfer coefficient (cm/s) and can be obtained from Equation (3.2), which is the convective mass-diffusion equation across a laminar boundary layer to a flat surface with a known bulk gas velocity [97].

$$k_{MTC} = \frac{4}{3} \frac{D_{N_2-O_2}}{l} (Re)^{\frac{1}{2}} (Sc)^{\frac{1}{3}} \tag{3.2}$$

Re and Sc are the Reynolds number (ul/ν) and Schmidt number ($\nu/D_{N_2-O_2}$), respectively. u is the velocity of the gas mixture above the sample surface (cm/s), l is the sample's length (cm), and ν is the kinematic viscosity of the gas (g/cm.s). $D_{N_2-O_2}$ is the diffusion coefficient in the binary gas layer (cm^2/s), and can be calculated via the Chapman-Enskog formulation of the kinetic theory of gases [130].

$$D_{N_2-O_2} = \frac{1.858 \times 10^{-3} \sqrt{T^3 \left(1/M_{N_2} + 1/M_{O_2}\right)}}{p \, \sigma^2_{N_2-O_2} \Omega_{N_2-O_2}} \tag{3.3}$$

T is the temperature (K), p is the pressure (atm.), M_{N_2} and M_{O_2} are the molecular weights of nitrogen and oxygen (g/mol). $\sigma_{N_2-O_2}$ is the average collision diameter (in) in the N_2-O_2 gas mixture, and can be estimated by the average of individual collision diameters of oxygen and nitrogen (σ_{N_2} and σ_{O_2}). $\Omega_{N_2-O_2}$ is the collisional integral for diffusion, which is dimensionless and a function of a dimensionless temperature parameter $\frac{kT}{\varepsilon_{N_2-O_2}}$, where k is the Boltzmann constant, and $\varepsilon_{N_2-O_2}$ is the interaction energy between oxygen and nitrogen molecules. σ_{N_2}, σ_{O_2}, ε_{N_2}/k and ε_{O_2}/k are the Lennard-Jones parameters. These parameters as well as the collisional integral for diffusion for oxygen and nitrogen are obtained from [59].

In order to calculate the kinematic viscosities (given by $\nu = \eta/\rho$, where η is absolute viscosity and ρ is density), the absolute viscosities (η) for the two gases have to be calculated [130].

$$\eta = \frac{2.669 \times 10^{-5} \sqrt{MT}}{\sigma^2 \Omega} \tag{3.4}$$

M is the molecular weight of the species. In order to calculate the viscosity for a mixture of gases, the method given by [130] is used.

$$\eta_{N_2-O_2} = \frac{X_{N_2} M^{1/2}_{N_2} \eta_{N_2} + X_{O_2} M^{1/2}_{O_2} \eta_{O_2}}{X_{N_2} M^{1/2}_{N_2} + X_{O_2} M^{1/2}_{O_2}} \tag{3.5}$$

X_{N_2} and X_{O_2} are the mole fractions of nitrogen and oxygen in the gas mixture, η_{N_2} and η_{N_2} are the absolute viscosities of each gas at the system temperature

and pressure. The densities of each gas and the binary mixture of gases at different temperatures were calculated. Therefore, the dimensionless Reynolds and Schmidt numbers are calculated as required for having the mass transfer coefficient k_{MTC}.

Finally, the linear rate constants calculated using Equations (3.1) to (3.5) were compared with the ones measured in the experiments. The calculated values were not sensitive to small changes of a few percent in the parameters. The discrepancy between the model and the experiments can be due to the assumption that all the oxygen molecules diffused to the alloy surface are consumed. In other words, the sticking probability was neglected in the model. By considering sticking probabilities of 0.3 for oxidation with a gas linear flow rate of 26.6 sccm, and 0.4 for 53.3 sccm, the discrepancy between the model and the experiments was below 6 percent, for both the low and high flow rates (See Figure 3.11). These sticking probabilities are very close to the values found previously in the literature [77].

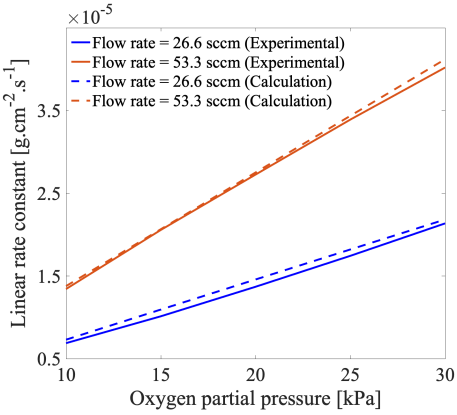

Figure 3.11: Comparison between measured and calculated linear rate constants for oxidation at 1000 °C with considering the sticking probabilities of 0.3 and 0.4, respectively for low and high linear flow rates.

Based on all the data and calculations, it was concluded that gas-phase mass transfer is the controlling step in the HT oxidation of iron-manganese alloys within the mentioned experimental condition. It means that species diffusion through the oxide scale was fast enough and did not control the oxidation rate. Knowing the diffusion coefficient of iron cations in the oxide scale [74] (which is fully wüstite; see Figure 3.8), the total flux of iron species to the scale-gas interface can be calculated. So, it can be confirmed via calculations that the diffusion within the oxide scale has been quick enough and it was not the controlling step.

In the short-time oxidation experiments done in this work, the growth of the oxide layer was linear, which means that the amount of iron cations needed at the surface to form a new layer of oxide is constant during the time. Using Equation (3.6), the total mass gain caused by oxygen entering the oxide layer from the gas environment can be calculated.

$$\frac{\Delta m}{A} = k_l \times t \tag{3.6}$$

Where Δm is the oxygen mass-gain (g), A is the oxidized area of the sample (cm2), and t is the time (s). Having the linear rate constant from the experiments, the mass of oxygen per unit area per second can be calculated and translated to the number of moles of oxygen. Assuming wüstite (FeO) as the only oxide phase present in the oxide scale, the number of moles of oxygen and wüstite would be equal. Therefore, the average thickness of the oxide scale as a function of time can be calculated from the experimental data.

Then, the flux of iron that can diffuse through the growing oxide layer at each time step and unit area is calculated. Since the thickness of the oxide layer is growing over time, it is expected to see a decreasing flux of iron diffused through the oxide layer, which in the end leads to parabolic growth. A coupled linear-parabolic kinetic model was implemented to find the flux of iron that is diffused from the substrate to the scale-gas interface. Then the incorporation rate of oxygen can be related to the outward flux of iron ions [124].

$$J_O = \frac{J_{Fe}}{1 - \tilde{\delta}} \tag{3.7}$$

Where $\tilde{\delta}$ is the average iron deficiency in the wüstite scale ($Fe_{1-\tilde{\delta}}O$), moreover, the outward flux of iron can be calculated as followed.

$$J_{Fe} = \frac{D\delta^{Fe/FeO}}{xV}\left(\frac{\delta^*}{\delta^{Fe/FeO}} - 1\right) \tag{3.8}$$

Where δ^* and $\delta^{Fe/FeO}$ are the iron deficiency at the scale-gas and the scale-alloy interface, respectively. D is the diffusion coefficient of iron in the wüstite scale and is assumed to be only a function of temperature [74]. x and V are the thickness and the molar volume of the oxide scale, respectively. Due to the high oxygen partial pressure, based on the phase diagram, it is expected that a thin layer of magnetite is formed on top of wüstite (Figure 3.7). Then local thermodynamic equilibrium is established at the magnetite-wüstite interface, and δ^* can be taken as the iron deficiency of wüstite at that interface (δ^{FeO/Fe_3O_4}). Moreover, the equilibrium iron deficiency of wüstite (δ) is a function of oxygen partial pressure [63].

$$log(pO_2) = M\left(\frac{1}{1-\delta}\right) + B \tag{3.9}$$

Where B and M are temperature-dependent constants that were experimentally evaluated for the temperature range of 700 to 1300 °C [63].

$$M = -\frac{7765.6}{T} + 29.4 \tag{3.10}$$

and

$$B = -\frac{19475.1}{T} - 24.1 \tag{3.11}$$

Then the iron deficiency of wüstite at both wüstite-alloy and wüstite-magnetite interfaces can be obtained simply by putting equilibrium oxygen partial pressures at wüstite-alloy and wüstite-magnetite interfaces in Equation (3.9). Therefore, assuming that all the iron species diffused through the oxide layer would immediately react with the oxygen at the surface, the oxide layer thickness as a function of time can be calculated assuming that solid-phase diffusion is the rate-controlling step.

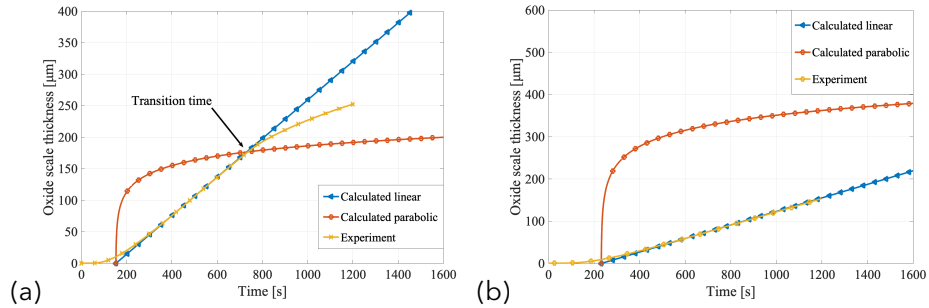

Figure 3.12: Calculated oxide scale thickness as a function of time for gas-phase mass transfer as the rate controlling step (linear) and for solid-phase diffusion as the rate controlling step (parabolic) compared to the experimental result. The oxidation experiment is conducted for 20 minutes at 1000°C with a gas linear flow rate of 53.3 sccm (a) in the presence of 30 kPa oxygen partial pressure, and (b) in the presence of 15 kPa oxygen partial pressure.

Figure 3.12 shows both the linear and parabolic growth regimes. At each moment, the slower one would be controlling the oxidation rate. In Section 3.4, for 30 kPa oxygen partial pressure, the transition time from linear to parabolic occurred after around 10 minutes in the experiment in agreement with the calculated transition time. On the other hand, for 15 kPa oxygen partial pressure Section 3.4, the transition time is beyond the 20 minutes of oxidation. Gas-phase diffusion is slower and controls oxidation. It shows that the experimental results of this work are in agreement with the proposed mechanism for oxidation.

Similar calculations were done for all the experimental oxidation conditions used. In most cases within the first 20 minutes, the solid-phase diffusion was predicted to be faster. Exceptions were the alloys oxidized at 1000 °C in the presence of 25 and 30 kPa oxygen with a linear flow rate of 53.3 sccm. Those showed a parabolic growth already before the 20 min. The transition times obtained from the calculations are close (average deviation of around 10%) to those determined from the experiments.

Furthermore, the difference between the thickness of the oxide scale on different spots of the specimens can be explained by the diffusion of oxygen through the laminar boundary layer. The parts of the sample that are close to the leading edge (which means smaller l in Equation (3.2)) will get more oxidizing gas diffused to the surface. Therefore, the oxidation is faster on top of the sample which

causes the oxide scale on top of the sample to be substantially thicker than the bottom.

Figure 3.13 schematically shows all the stages from the beginning of the oxidation experiment until the end. It starts when the sample is at the required temperature and the atmosphere is switched from inert to oxidizing gas (Figure 3.13(a)). A gas mixture of oxygen and nitrogen flows over the sample surface. The oxygen molecules are in contact with the sample surface and the oxidation starts with the formation of a thin oxide layer on the surface (Figure 3.13(b)). A laminar boundary layer is formed on the surface of the specimen because of the gas flow, and the diffusion of oxygen molecules through this layer becomes the rate-determining step for the oxidation (Figure 3.13(c)). After 20 minutes of oxidation, the atmosphere is switched back to inert gas. Due to the thinner boundary layer and therefore faster diffusion to the leading edge, the scale is much thicker than at the trailing edge (bottom) (Figure 3.13(d)).

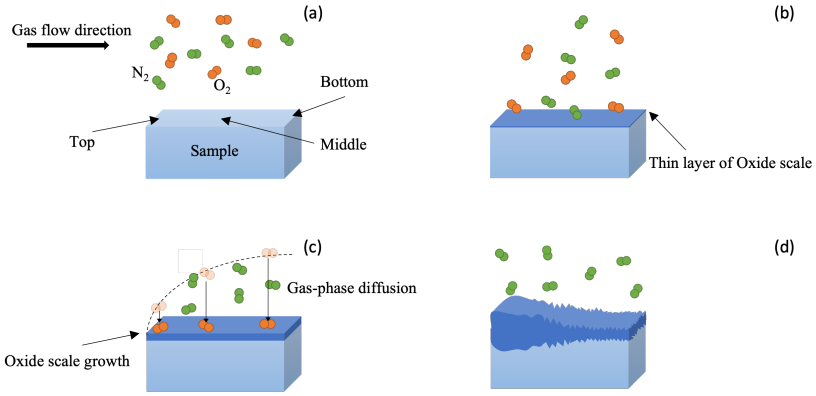

Figure 3.13: Schematic illustration of the alloy surface at different stages during HT oxidation of Fe-Mn samples in N_2-O_2 atmosphere. From (a) the start of the oxidation when the oxidizing gas flows over the sample, to (b) the formation of the oxide scale, (c) the formation of the boundary layer and diffusion of gas through this layer, and finally, (d) formation of a thicker and less rough oxide on the top part of the sample.

3.5. Conclusions

To study the kinetics and the mechanism of HT oxidation of Fe-Mn binaries, a series of experiments were conducted. The samples of pure iron and iron with 1, 3, and 5 wt% Mn were oxidized at 950-1150 °C in gas mixtures with 10-30 kPa oxygen and linear flow rates of 26.6 and 53.3 sccm. The following conclusions can be drawn.

1. In all of the oxidizing conditions, the oxidation kinetics of the samples showed a linear growth rate in the beginning. Only the samples oxidized in 25 and 30 kPa oxygen partial pressures with the linear flow rate of 53.3 sccm experienced the transition to parabolic growth within the first 20 minutes of

oxidation. Oxygen partial pressure and gas linear flow rate were the only parameters influencing the oxidation kinetics. Temperature and Mn content had no significant effect on the growth rates. An activation energy of around 2 $kJ \cdot mol^{-1}$ was obtained from the experiments.

2. Wüstite was the only oxide phase present in the scale during oxidation at high temperatures. But it was transformed to magnetite due to a low cooling rate (10 °C/min).

3. Within the 20 minutes of oxidation, the gas-phase mass transfer through a laminar boundary layer was the rate-controlling step for the oxidation reaction. On the leading and trailing edge of the sample, the oxidation rate was different, due to the substantial difference in the boundary layer thickness at different lengths. It led to thicker oxide layers on top and thinner ones at the bottom of the sample.

4. The measured linear rate constants were compared with the ones calculated via a model based on gas diffusion to the sample surface. The measured and calculated values agreed when taking into account the sticking probability (0.3-0.4) of oxygen molecules on the surface.

Understanding the kinetics and mechanism of initial HT oxidation of alloys in various oxidizing conditions can significantly help to develop new steel grades. Further study on other iron binary or ternary alloys will be necessary, in order to give more insights regarding the role of different alloying elements on the oxidizing behavior of the alloys.

4

Numerical Model For Isothermal Oxidation of Fe-Mn Binaries

Since the oxidation reactions in the process of steel production occur in harsh conditions (i.e. high temperatures and gas atmospheres), it is practically impossible to observe in-situ the compositional changes in the steel and the formed oxide scale. Hence, a coupled thermodynamic-kinetic numerical model is developed that predicts the formation of oxide phases and the composition profile of the steel alloy in a short time due to external oxidation. The model is applied to high-temperature oxidation of Fe-Mn alloys under different conditions. Oxidizing experiments executed with a thermogravimetric analyzer (TGA) on Fe-Mn alloys with different Mn contents (below 10 wt %) are used to determine kinetic parameters that serve as an input for the model. The mass gain data as a function of time show both linear and parabolic regimes. The results of the numerical simulations are presented. The effect of different parameters, such as temperature, Mn content of the alloy, oxygen partial pressure, and oxidizing gas flow rate on the alloy composition and oxide phases formed is determined. It is shown that increasing the temperature and decreasing the oxygen partial pressure both lead to a thicker depleted area.

This chapter has been published in [5] by S. Aghaeian, J.C. Brouwer, W.G. Sloof, J.M.C. Mol, and A.J. Böttger, "Numerical Model For Short-Time High-Temperature Isothermal Oxidation of Fe–Mn Binaries at High Oxygen Partial Pressure." High Temperature Corrosion of Materials **(2023)**: 1-18.

4.1. Introduction

High-temperature oxidation is a prominent phenomenon in several steps of steelmaking, such as hot rolling. Oxidation at high temperatures and high oxygen partial pressure can change the composition of the steel near the surface due to the depletion of the alloying elements. Furthermore, the oxide scale's characteristics such as thickness and phase composition vary depending on the oxidation condition. Since it is challenging to study such rapid processes under such extreme conditions experimentally, models are needed to predict the composition at the substrate surface as well as that of the oxide scale.

To model the oxidation behavior, fundamental and comprehensive knowledge of thermodynamics and kinetics of the occurring process is required [111, 39]. Although numerical and analytical models have been developed to predict the oxidation behavior and the compositional change of alloys during thermal oxidation, their general application is limited. A number of these studies focused on finding a criterion to predict whether internal or external oxidation occurs [95, 17, 60, 68, 61]. Furthermore, mathematical models developed for external oxidation of binary and ternary alloys mostly consider only parabolic growth kinetics for the oxide layer [115, 33, 28, 114, 117], while the growth rate in the initial stages of oxidation is usually linear [115, 89, 181]. Moreover, in most cases, only selective oxidation of the alloying element forming the most stable oxide phase at low oxygen partial pressures is considered [100, 17, 60, 65, 66, 164, 166, 170].

As an input for the oxidation simulations, the linear and parabolic kinetic constants of the oxidation reaction under different conditions of steel composition, temperature, and oxygen partial pressure are needed [115, 184, 127, 125, 126]. For the hot-rolling process, high oxygen partial pressures and temperatures need to be considered. However, experimental research on the oxidation of iron alloys with manganese as the main alloying element is either focused on the annealing step, i.e., at low oxygen partial pressures [149, 157, 103, 104, 141] or are done for long exposure times [108, 81, 172].

In the present work, a coupled thermodynamic-kinetic numerical model is developed that also considers hot-rolling conditions, based on earlier works by Nesbitt [114], and Nijdam [116, 115]. The model is applicable to high-temperature external oxidation of different alloys in dry oxygen with different partial pressures and flows. Here the model is applied to short-time, high-temperature oxidation of iron-manganese binary alloys to predict the amount of formed oxides, the concentration profiles of iron and manganese within the substrate alloy, and their oxide/metal (O/M) interface concentration. Measuring such parameters is not simply possible experimentally, because during cooling diffusion and homogenization in both the oxide scale and the substrate alloy can occur. Furthermore, fast cooling of steels could evoke phase transformations (such as martensite formation). Therefore, the developed model could provide information on oxidation that is practically impossible to measure.

The simulation consists of two main steps. In the first step, thermodynamic calculations are implemented in order to predict the stable phases. In the second step, the alloy composition change beneath the O/M interface is calculated using

a recently developed modified flux equation for a lattice fixed frame of reference [90, 91].

There are several advantages of the current model over the previous analytical and numerical models for oxidation. First, the computations include the initial stages of oxidation, whereas previous models only considered long-time exposures. Second, there is no limit to the number of elements that can oxidize simultaneously, unlike previous models that considered the most stable oxide phase only. Finally, the computation time is shorter due to the implementation of the modified flux equation for diffusion.

As an input for the calculations, the kinetic constants of both linear and parabolic growth modes are needed. Therefore, a series of oxidation experiments using a thermogravimetric analyzer (TGA) were conducted. The iron-manganese alloys were exposed to a gas mixture with different oxygen partial pressures and different velocities. Then the kinetic constants were obtained from the mass gain data.

4.2. Coupled Thermodynamic-Kinetic Model

We have considered a single-phase Fe-Mn binary alloy reacting with oxygen at temperature T and pressure p.

$$\frac{2x}{y}\mathrm{Me} + \mathrm{O_2} \rightarrow \frac{2}{y}\mathrm{Me_xO_y} \tag{4.1}$$

where Me represents Fe or Mn.

The most stable oxide phases can be found by calculating and comparing the dissociation oxygen partial pressures at the O/M interface for different oxide phases, through their standard Gibbs free energy of formation $\Delta G^{\circ}_{\mathrm{Me_xO_y}}$ [115]. The equilibrium oxygen partial pressure in which the oxide $\mathrm{Me_xO_y}$ is in local equilibrium with the metal at the interface, can be calculated according to:

$$p_{O_{2(\mathrm{Me_xO_y})}} = \left(\frac{a_{Me_xO_y}^{\frac{2}{y}}}{a_{Me}^{\frac{2x}{y}}} \right) \exp\left(\frac{\Delta G^{\circ}_{\mathrm{Me_xO_y}}}{RT} \right) \tag{4.2}$$

where $a_{Me_xO_y}$ and a_{Me} are the thermodynamic activities of the oxide phase $\mathrm{Me_xO_y}$ and the alloy constituent (Me) at the O/M interface, respectively.

A phase diagram that shows the iron and manganese oxides phases which can form at 1000 °C, is shown in Figure 4.1. The mixture of MnO and FeO (wüstite) is the most stable oxide phase forming at very low oxygen pressure. Due to the higher diffusion coefficient of Fe and Mn in wüstite than in magnetite and hematite, wüstite grows much faster than the other oxides. This for high temperature oxidation of pure iron, results in the formation of wüstite, magnetite, and hematite with thickness ratios of 95, 4, and 1, respectively [67]. In-situ XRD results [4] also showed the formation of FeO and MnO together as a solid solution at oxidizing temperature. It is also known that during the linear growth of the oxide scale, a local equilibrium between the oxide scale and the alloy is established,

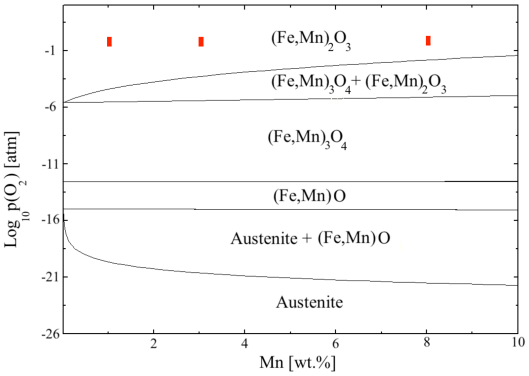

Figure 4.1: Stability regions of different iron and manganese oxide phases as a function of Mn weight fraction and oxygen partial pressure at 1000 °C, obtained by using Factsage software [16]. The red marks show the experimental conditions of this work which are oxygen partial pressures of 10, 20, and 30 kPa for three different alloys.

and thus the equilibrium oxygen partial pressure is fixed. The parabolic regime starts only after the formation of magnetite and hematite. Then the equilibrium oxygen partial pressures at the wüstite/magnetite and magnetite/hematite interfaces are also fixed. Although all the iron oxide phases can form in such conditions, it was seen that wüstite (FeO+MnO) was the main oxide phase that formed more than 95% of the oxide scale. Therefore, only FeO and MnO are the considered oxides in our simulations.

The simulation is based on a model which was developed and also validated previously [116, 127, 126]. A schematic illustration of the grid used for the model calculations at the start of the oxidation process ($t = 0$) and also after some time ($t = t$) is shown in Figure 4.2. At the beginning of oxidation, a number of slices L with an initial equal width of $\Delta z^{i,0}$ are defined perpendicular to the surface of the alloy with total thickness Z. Z is considered thick enough to simulate a semi-finite diffusion case. The slices have a homogeneous and uniform composition $C_{\mathrm{Me}}^{i,0}$, where i and Me refer to the slice number and the constituent (Fe or Mn), respectively.

The compositional variations parallel to the metal surface are negligible, thus only diffusion perpendicular to the O/M interface within a limited depth of material is considered. The positions of the boundaries between slices are indicated with z^i, and the concentration of each slice is assigned to the middle point of each slice which is located at l^i. Therefore, the number of moles of each constituent Me at each slice at the beginning of oxidation is $n_{\mathrm{Me}}^{i,0}$, for which it holds that:

$$n_{\mathrm{Me}}^{i,0} = \frac{N_{\mathrm{Me}}^{i,0} \Delta z^{i,0}}{V_m} \tag{4.3}$$

where $N_{\mathrm{Me}}^{i,0}$ and V_m are the initial mole fraction of the constituent Me and the molar volume of the alloy, respectively. After establishing the grid, the time is increased

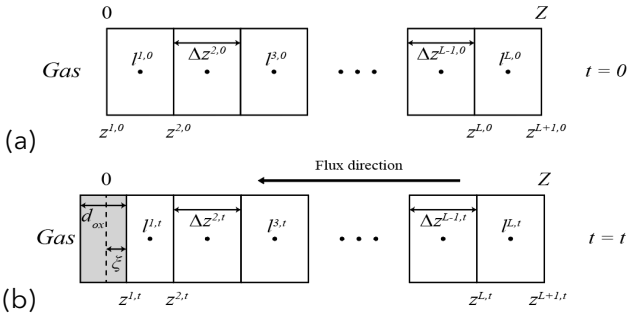

Figure 4.2: Schematic of the grid used for the calculations (a) at the start of oxidation ($t = 0$) and (b) after a time ($t = t$).

by a small increment Δt. The explicit method for solving the above equation is limited by the stability criterion S [54] and as such the time-steps Δt being used must be smaller than the stability limit.

$$S = D\left[\frac{\Delta t}{\Delta z^2}\right] \leq 0.25 \tag{4.4}$$

where D is the diffusion coefficient of the diffusing element. After a certain amount of time t, a layer of oxide with the thickness d_{ox} is formed at the alloy surface; see Figure 4.2b. The oxidation leads to an interface displacement ξ with respect to the initial metal/gas interface.

At each time step, a number of calculations are performed which provide information such as oxide scale thickness, concentrations of the slices 2 to L, displacement of the O/M interface, and the interface concentrations for the next time step. It is assumed that local thermodynamic equilibrium at the O/M interface is established at each time step. The mass balance at the O/M interface plays an important role in the calculations. It is assumed that no material is lost, implying that all material that diffuses out of the alloy is present in the oxide scale.

4.2.1. Oxide scale thickness

In order to calculate the total oxide scale thickness at time t, the scale growth kinetic data such as linear and parabolic constants are needed. The fast initial stage of oxidation is linear which changes into a parabolic regime with a slower growth rate at $t = t_{trans}$. Having the required kinetic data, the calculations are as follows:

$$t \leq t_{trans} \rightarrow d_{lin} = k_{lin}\, t \tag{4.5a}$$

$$t > t_{trans} \rightarrow d_{par} = \sqrt{k_{par}(t - t_{trans})} \tag{4.5b}$$

$$d_{ox} = d_{lin} + d_{par} \tag{4.5c}$$

where k_{lin} and k_{par} are the kinetic constants for the linear and parabolic regimes, respectively.

The total oxide scale thickness d_{ox} formed at time t, can be related to the total amount of oxides Me_xO_y that is formed at the O/M interface, which are FeO and MnO based on the assumption of this work. It is expressed in terms of the volume of each oxide per unit interface area of the alloy, $\varphi_{Me_xO_y}$. Then, it holds that:

$$d_{ox} = \Sigma\varphi_{Me_xO_y} \tag{4.6}$$

Consumption of the material from the alloy also results in the displacement of the O/M interface [170]. Compared to its original location at $t = 0$, the displacement of the OM interface can be calculated by considering the mass balance, as:

$$\xi = \frac{V_{Mn}\varphi_{MnO}}{V_{MnO}} + \frac{V_{Fe}\varphi_{FeO}}{V_{FeO}} \tag{4.7}$$

where V_{MeO} is the molar volume of FeO and MnO, and V_{Me} is the partial molar volume of each component at the OM interface in the alloy.

4.2.2. Concentrations of the second to last slices

Due to the consumption of the constituents from the metal substrate by the oxide formation, a concentration difference is established between neighboring slices, which drives diffusion of the constituting elements. For calculating the concentration profile underneath the alloy-surface, a modified flux equation was used [116, 91, 90]. The flux of manganese at time t from slice i to $i+1$ is given by:

$$J_{Mn}^{i/i+1,t} = -\frac{RT}{V_m}\left(\frac{\sqrt{M_{Mn}^{i+1,t}N_{Mn}^{i+1,t}M_{Mn}^{i,t}N_{Mn}^{i,t}}}{l^{i+1,t} - l^{i,t}}\right) 2\sinh\left(\frac{\mu_{Mn}^{i+1,t} - \mu_{Mn}^{i,t}}{2RT}\right) \tag{4.8}$$

where R is the gas constant ($Jmol^{-1}K^{-1}$), T is the temperature (K), $M_{Mn}^{i,t}$ and $\mu_{Mn}^{i,t}$ are the mobility and chemical potential of manganese at time t (s) in slice i, respectively. The value for the mobility of iron and manganese are obtained from the tracer diffusion coefficient of each constituent Me in the phase ϕ (here austenite), which is included in [10]:

$$M_{Me}^{\phi} = \frac{D_{Me}^{*,\phi}}{RT} \tag{4.9}$$

where $D*$ is the tracer diffusion coefficient of Me in ϕ. Calculations conducted via DICTRA [10] show that the diffusion coefficient of Mn is only weakly dependent on concentration; if the Mn concentration in the alloy increases from 0.5 to 8%, the diffusion coefficient of Mn in the matrix would increase only around 10%. This ideal behavior of Fe-Mn alloys has also been reported before in previous works [101]. Assuming ideal behavior for low concentration of the alloying elements,

i.e. negligible interaction between the elements, the chemical potential of each constituent can be simply related to its mole fraction, according to:

$$\mu_{\mathrm{Me}}^{i,t} = RT \ln N_{\mathrm{Me}}^{i,t} \tag{4.10}$$

A zero-flux slice is considered at depth Z in the bulk, which is far enough from the interface to be unaffected by the oxidation:

$$J_{\mathrm{Me}}^{L} = 0 \tag{4.11}$$

The value for the flux of both iron and manganese between all the slices at each time t allows calculating the number of moles of the constituents in the slices 2 up to the last one for the next time step $t + \Delta t$ by:

$$n_{\mathrm{Me}}^{i,t+\Delta t} = n_{\mathrm{Me}}^{i,t} + \Delta t \left(J_{\mathrm{Me}}^{i,t} - J_{\mathrm{Me}}^{i+1,t}\right) \tag{4.12}$$

Therefore, at each time step, a series of calculations through Equation (4.8) to Equation (4.12) results in the concentration for the second to the last slice for the next time step to be calculated as shown in the flowchart; see Figure 4.3. However, for calculating the composition of the alloy at the O/M interface another method, described in Section 4.2.3, has been implemented.

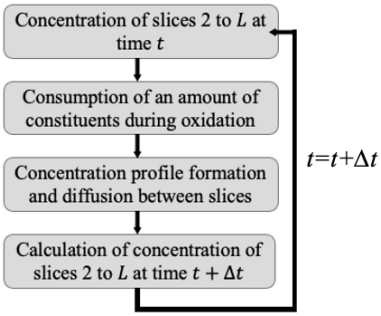

Figure 4.3: Flowchart of the model operations.

4.2.3. The interface composition and displacement

The interface concentration of manganese is constantly changing during oxidation because of the consumption of manganese. To determine whether oxidation occurs of only manganese or also iron, a series of calculations was performed [115]. Since Mn forms a more stable oxide than Fe (i.e. $p_{O_{2_{\mathrm{MnO}}}} < p_{O_{2_{\mathrm{FeO}}}}$; cf. Equation (4.2)), oxidation of Mn at the O/M interface occurs first, and the interface concentration of manganese would decrease. Due to the limited amount of Mn present at the interface (which is related to the concentration and diffusion coefficient of manganese in the alloy), all the Mn at the interface is consumed at each time step. Moreover, the mass balance at the O/M interface must be fulfilled. This implies that the total amount of iron and manganese incorporated into the

oxide layer at time t must be equal to the same amount consumed from the alloy until time t. So at time t, the mass balance can be written as:

$$\frac{\varphi_{MeO}}{V_{MeO}} = \int_0^Z C_{Me}^0 dz - \int_\xi^Z C_{Me}^t dz \tag{4.13}$$

where C_{Me}^0 is the initial concentration of the constituents, and ξ is the interface recession. Therefore at each time step, the total amount of Mn consumed from the substrate metal, which is denoted as the so-called accessible amount Γ^t, can be calculated by Equation (4.14). As explained before, all the Mn at the interface is considered to be consumed, so $C_{\text{Mn}}^{1,t+\Delta t}$ is virtually zero. It is shown as the green area in Figure 4.4.

$$\Gamma_{Mn}^t = \int_{\xi^t}^Z C_{Mn}^t dz - \int_{\xi^{t+\Delta t}}^Z C_{Mn}^{t+\Delta t} dz \tag{4.14}$$

Where the difference between $\xi^{t+\Delta t}$ and ξ^t is the O/M interface displacement due to consumption of Γ_{Mn}^t during Δt, which can be calculated with Equation (4.7).

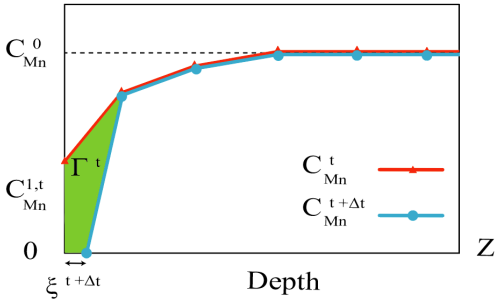

Figure 4.4: Schematic of accessible amount, i.e. the total amount of Mn from the substrate metal consumed by the oxide within the time step Δt.

Now $\Delta\varphi_{\text{MnO}}$ can be used as a criterion to determine if only the most stable oxide is present or that simultaneously the other constituent's oxide form. So at each time step, $\Delta\varphi_{\text{MnO}}$ is compared with Δd_{ox} (the thickness of the oxide scale formed during Δt) to establish the oxides formed.

1. If $\Delta\varphi_{\text{MnO}} \geq \Delta d_{ox}$, only MnO is formed during the time step Δt. Then the amount of MnO formed during this time step, $\varphi_{\text{MnO}}^{\Delta t}$, is equal to Δd_{ox} (see Equation (4.6)). Therefore, the displacement of the O/M interface can be obtained by Equation (4.7), with $\Delta\varphi_{\text{FeO}}$ equal with zero.

2. If $\Delta\varphi_{\text{MnO}} < \Delta d_{ox}$, simultaneous oxidation of Mn and Fe occurs during Δt. Then the amount of FeO formed ($\Delta\varphi_{\text{FeO}}$) is equal with $\Delta d_{ox} - \Delta\varphi_{\text{MnO}}$. Accordingly, the interface displacement can be calculated by Equation (4.7).

4.2.4. Grid adjustment

After each series of calculations for a time step, the interface displacement requires a rearrangement of the grid system in order to obtain a new set of semi-distance grid points (grid points are at the middle point of each slice). To achieve this, the size Δz and the number L of the slices are kept constant, as well as the total studied thickness of the alloy at each time step. Therefore at each time step, the starting point of the grid is moved inward by the value of $\Delta\xi^{\Delta t}$. The position of slices' walls z^i can be calculated with:

$$z^{i,t+\Delta t} = z^{i,t} + \Delta\xi^{\Delta t} \qquad i = 1, 2, 3, ..., L \tag{4.15}$$

Eventually, by having the oxide scale growth kinetics of the alloy, the concentration profile for both iron and manganese inside the alloy as well as the amount of each oxide phase formed can be obtained as a function of time by numerically solving Equations (4.2) to (4.15). To this end, a numerical model, based on finite difference technique [8], was developed in MATLAB [105].

4.3. Experiments

The kinetic data needed as an input for the simulations were obtained from oxidation experiments conducted using TGA.

The Fe-Mn alloys were provided by ChemPur (Karlsruhe, Germany). The chemical composition of the alloys with different manganese contents as obtained with inductive coupled plasma-optical emission spectrometry (ICP-OES) is presented in Table 4.1. The alloys were cut into 2 × 8 × 15 mm pieces with a hole of 2.2 mm diameter by electric discharge machining (EDM). Then, they were ground using SiC emery paper and cleaned ultrasonically in isopropanol. Finally, the specimens were stored in airtight membrane boxes (Agar Scientific, G3319, Essex, UK) after drying with a flow of pure nitrogen gas.

Table 4.1: Chemical composition of the alloys obtained with ICP-OES.

Sample	Elements (wt %)				
	Mn	C	Al	Si	Cr
Fe-1Mn	1.030	0.0157	0.0012	0.0010	0.0026
Fe-3Mn	2.845	0.0002	0.0002	0.0014	0.0002
Fe-8Mn	7.930	0.0031	0.0003	0.0020	0.0110

The alloys were oxidized in a symmetrical thermogravimetric analyzer (TGA, Setaram TAG 16/18, Caluire, France) in order to calculate the kinetic constants from the mass-gain data. An alumina pin with a diameter of 2.2 mm was inserted into the hole in the sample and placed onto a sapphire rod. The initial mass of the sample was measured by a Mettler Toledo balance (accuracy ±1 µg). To eliminate any buoyancy effect, a dummy sample of alumina of the same size was mounted onto a sapphire rod the counterpart of the balance. The furnace chambers were two identical tubes with 280 mm length and an inner diameter of 15 mm. First,

the TGA system was pumped to vacuum (<50 Pa). Then the gas lines, balance, and furnaces were flushed with pure nitrogen three times. The purity of nitrogen was 5N vol.%, and it was filtered additionally to remove any residual hydrocarbons, moisture, and oxygen, with Accosorb (<10 ppb hydrocarbons), Hydrosorb (<10 ppb H_2O) and Oxysorb (<5 ppb O_2) filters (Messer Griesheim, Germany), respectively. Next, both furnaces were heated up with a rate of 10 °C/min with a flow of pure nitrogen. Temperatures were chosen between 950 and 1150 °C. After reaching the target temperature, the chambers' atmospheres were switched to oxidizing by introducing a gas mixture of oxygen, and nitrogen. Different flow rates (26.6, 53.3, 100, 150, 200, and 250 mL min^{-1}, corresponding to average gas velocities of around 1 to 10 cms^{-1} at 1000 °C) and oxygen partial pressures (10 to 30 kPa) were applied by changing the ratio between O_2 and N_2 gases, while the total chamber pressure was kept at 101 kPa (1 atm). After oxidation, the furnace tube was cooled to room temperature with a rate of 10 °C/min while flushing with pure N_2.

The mass gain per unit area for an oxidation experiment in the TGA system is shown in Figure 4.5. The mass gain data corresponds with the total weight of oxygen consumed by the metal to form the oxide scale. The internal oxidation zone (IOZ) was negligible compared to the scale thickness. The mass gain data shows the initial linear growth of the oxide layer, which is followed by parabolic growth. The linear and parabolic rate constants are respectively the slope of the lines in mass gain and squared mass gain divided by area versus time. To obtain the slope of the line within the linear regime, the very first part of it is not considered due to the lack of oxygen in the beginning.

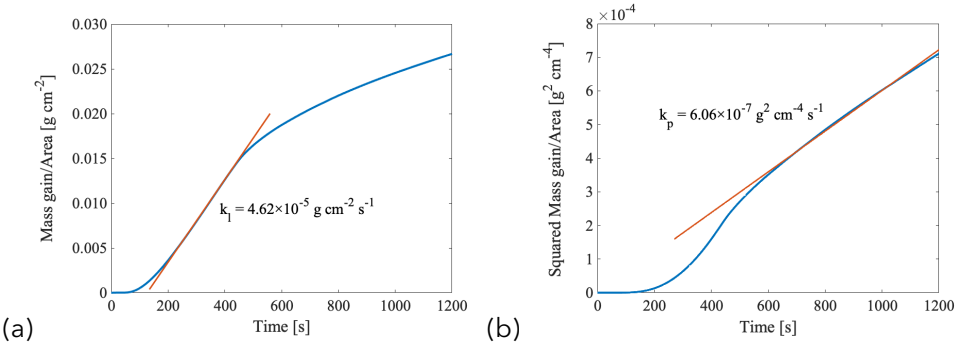

Figure 4.5: (a) The mass gain per unit surface area and (b) the squared mass gain per unit surface area data for 20 minutes of oxidation of Fe-8Mn binary alloys at 1000 °C in 20 kPa oxygen partial pressure with a total gas flow rate of 100 mL min^{-1}. The slopes of the lines represent the kinetic constants.

The details about the mechanism of high-temperature oxidation and characterization of the oxidized samples are described in our previous work [4]. It was concluded that for our experimental conditions, the linear growth of the oxide layer is controlled by the diffusion of the oxidizing gas through the boundary layer.

Different parameters that could influence the oxidation kinetics were studied. The effect of flow rate on the mass gain data is shown in Figure 4.6. It can be seen that an increase in the gas flow rate increases the linear constant (k_l) and total mass gain (Section 4.3), while it has almost no effect on the parabolic growth constant (Section 4.3). The linear constant increases from $1.4\times10^{-5}\pm3.1\times10^{-7}$ gcm^{-2}s^{-1} for oxidation with gas flow rate of 26.6 mL min^{-1} to $1\times10^{-4}\pm4.1\times10^{-7}$ gcm^{-2}s^{-1} for oxidation with gas flow rate of 250 mL min^{-1}. The parabolic constant only varies between $5.6\times10^{-7}\pm1.9\times10^{-9}$ and $5.7\times10^{-7}\pm3.0\times10^{-9}$ g^{2}cm^{-4}s^{-1} for oxidation with flow rates of 100 to 250 mL min^{-1}.

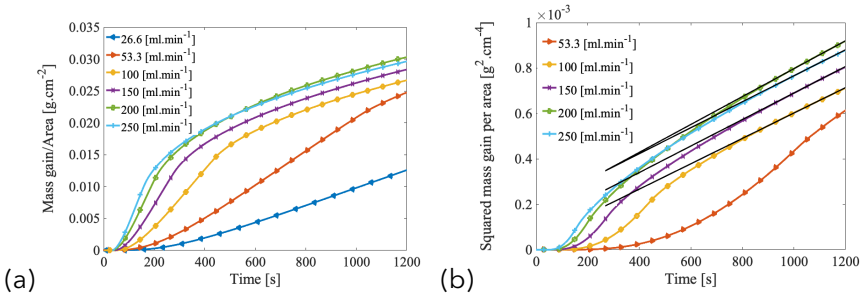

Figure 4.6: The experimental results for oxidation of Fe-8Mn binary alloy in 20 kPa oxygen partial pressure at 1000 °C for 20 minutes with a total gas flow rate between 26.6 to 250 mL min^{-1}: (a) mass gain per area, and (b) squared mass gain per area as a function of time.

The effect of increasing the oxygen partial pressure of the oxidizing gas mixture on the kinetics of the oxidation reaction is shown in Figure 4.7, and it was almost the same as rising the flow rate. It increased the linear constant from $4.3\times10^{-5}\pm2.5\times10^{-7}$ to $1.5\times10^{-4}\pm3.3\times10^{-6}$ gcm^{-2}s^{-1}, respectively for 10 and 30kPa, while the parabolic constant varied between $6.0\times10^{-7}\pm5.6\times10^{-9}$ and $6.6\times10^{-7}\pm6.4\times10^{-9}$ g^{2}cm^{-4}s^{-1} in the same range of oxygen partial pressure.

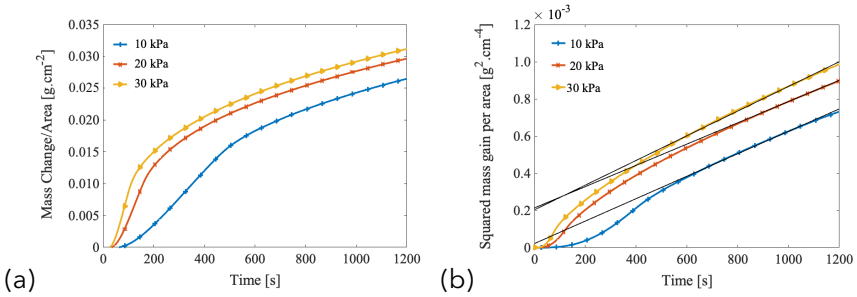

Figure 4.7: The experimental results for oxidation of Fe-8Mn binary alloy in 10, 20, and 30 kPa oxygen partial pressure at 1000 °C for 20 minutes with a total gas flow rate of 250 mL min^{-1}: (a) mass gain per area, and (b) squared mass gain per area as a function of time.

The effect of temperature on high-temperature oxidation of Fe-8Mn binary al-

loys oxidized in an atmosphere with 20 kPa oxygen with a flow rate of 200mL min^{-1} is shown in Figure 4.8. Increasing the temperature from 950 to 1150°C does not affect the slope of the linear part of the mass gain data, but only leads to a longer linear-to-parabolic transition time; see Section 4.3. However, oxidation at higher temperatures increases the parabolic kinetic constant; see Section 4.3. This is expected because of the higher diffusion rate through the oxide scale at higher temperatures. This also results in a longer linear regime because it takes a longer time before diffusion through the oxide layer becomes the rate-determining step. The parabolic constant increases from $5.90\times10^{-7}\pm1.59\times10^{-8}$ to 1.12×10^{-6} $\pm3.47\times10^{-8}$ $g^2cm^{-4}s^{-1}$, for oxidation at 950 and 1150 °C, respectively.

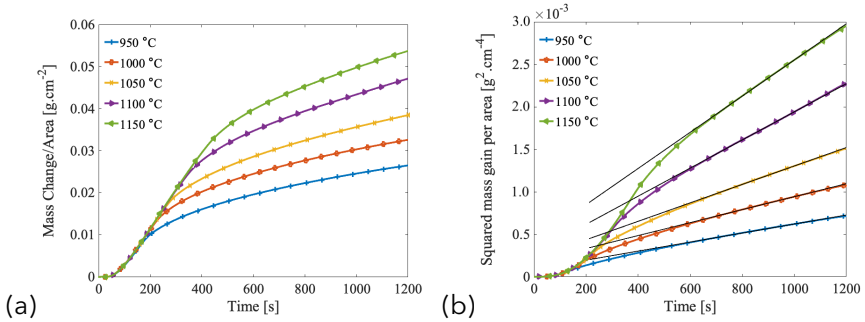

Figure 4.8: The experimental results for oxidation of Fe-8Mn binary alloy in 20 kPa oxygen partial pressure for 20 minutes with a total gas flow rate of 200 mL min^{-1}: (a) mass gain per area, and (b) squared mass gain per area as a function of time.

4.4. Simulation Results and Discussion

It is practically impossible to observe the O/M interface of the alloy, while oxidizing at very high temperatures. Only after the sample has cooled to room temperature the oxide scale can be analyzed. Within the cooling process, which is slow with TGA (10 °C/min), phase transformations and homogenization within the oxide scale and the alloy substrate will occur. Simulating the high-temperature oxidation allows the prediction of the changes in the alloy during oxidation. As mentioned earlier, this method for simulation was applied for MCrAlY coatings and alloys before and it has been validated by experiments [115, 116, 125].

The simulations were performed based on the model described in Section 4.2. The following data were used as input. The molar volume of the alloys were calculated with Thermo-Calc using the TCFE 5 database [10]; the molar volumes of MnO and FeO are taken to be 13.21 and 12.24 $cm^3\ mol^{-1}$, respectively [70]. The diffusion coefficients are taken from [12], and following Ref. [9] the mobilities of the alloy constituents in the alloy were calculated using Equation (4.9). The oxidation experiments with the Fe-Mn alloys (see Table 3.1) were conducted with TGA at 950 to 1150 °C, with 10 to 30 kPa oxygen partial pressure, and flow

rates of 26.6 to 250 mL min^{-1}. The oxide scale growth kinetic constants for the linear and parabolic parts were obtained from the mass gain data; see Section 4.3. As shown in Figure 4.9, the oxide growth kinetics in both linear and parabolic regimes could be described adequately with a combined linear and parabolic law (R-Squared= 0.98). Therefore, the developed model can predict the behavior of Fe-Mn alloys, which are oxidized within the mentioned range of oxidizing conditions.

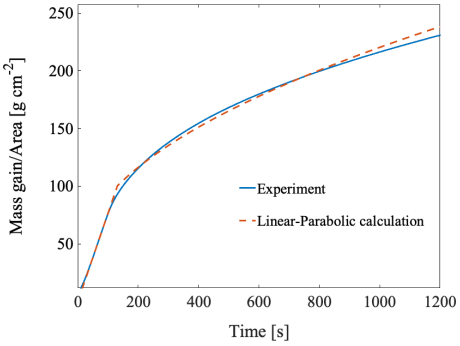

Figure 4.9: Experimental data and linear-parabolic calculation for oxidation of Fe-8Mn alloy at 1000°C in 20 kPa oxygen partial pressure with a gas flow rate of 250 mL min^{-1}, with linear and parabolic kinetic constants of $1.0\times10^{-4}\pm2.3\times10^{-6}$ $gcm^{-2}s^{-1}$ and $5.7\times10^{-7}\pm1.9\times10^{-8}$ $g^2cm^{-4}s^{-1}$, respectively.

The simulated concentration profiles of Mn in a Fe-8Mn alloy when it is oxidized in an environment with 20kPa oxygen partial pressure at different temperatures is demonstrated in Figure 4.10. It is observed that the depleted zone increased with increasing temperature, due to the faster diffusion of Mn within the alloy. Hence, the Mn depletion layer of less than 2 microns at 950 °C increases to more than 20 microns at 1150 °C.

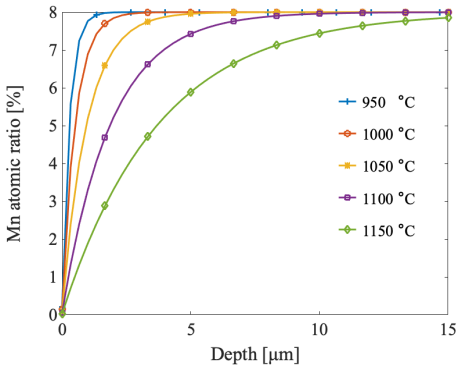

Figure 4.10: The calculated Mn concentration profiles within the alloy, when Fe-8Mn oxidized in the temperature range of 950 to 1150 °C in 20 kPa oxygen partial pressure for 20 minutes with a total gas flow rate of 53.3 mL min^{-1}.

The effect of the oxygen content in the oxidizing gas on the composition depth profile is calculated as well. In Figure 4.11 the simulated concentration profiles of Mn for Fe-8Mn when oxidized at 1000 °C for 20 minutes are demonstrated. It shows that reducing the oxygen partial pressure in the gas mixture from 30 to 10 kPa expands the manganese-depleted zone in the substrate alloy from 2 to more than 4 microns.

The effect of the composition of the alloy on concentration profiles is illus-

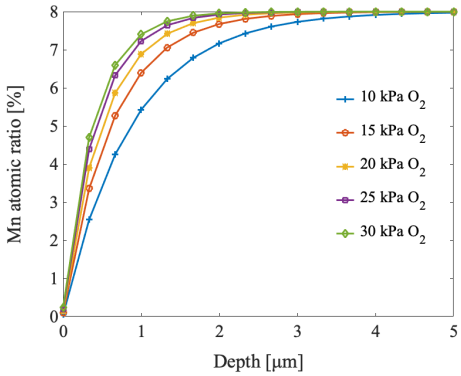

Figure 4.11: The calculated Mn concentration profiles within the Fe-8Mn substrate alloy when oxidized at the 1000 °C with oxygen partial pressure of 10 to 30 kPa for 20 minutes and a total gas flow rate of 53.3 mL min^{-1}.

trated in Figure 4.12. The Mn depleted zone is calculated to be less than 2 microns for all three alloy compositions. The Mn content has no clear effect on Mn depleted zone width. Also, a negligible effect of Mn content on the mass gain data (i.e. the kinetics of oxidation) was seen; see [4].

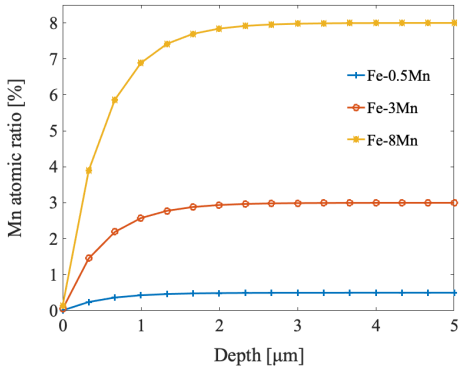

Figure 4.12: The calculated Mn concentration profiles within the substrate alloy for samples with different Mn contents when oxidized at the 1000 °C in 20 kPa oxygen partial pressure for 20 minutes with a total gas flow rate of 53.3 mL min^{-1}.

Generally, the oxide scale growth kinetics, and consequently the resulting compositional changes in the alloy, are significantly influenced by the oxidizing condition (e.g., T and p_{O_2}), microstructure, composition, and surface condition of the alloy [148]. The oxidation model is applied to study the effect of the scale growth kinetics on the composition near the surface of the alloy as well as the oxide phase constitution of the developing oxide layer, for the oxidation of Fe-Mn alloys at high temperatures. The effect of initial linear growth rate on the relative amount of Mn oxide ($\varphi_{MnO/d_{ox}}$) is shown in Figure 4.13.

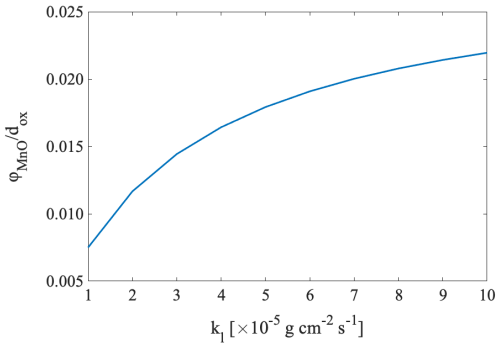

Figure 4.13: Calculated values for the ratio of MnO thickness to oxide scale thickness ($\varphi_{MnO/d_{ox}}$) as a function of linear oxidation growth rate for Fe-8Mn alloy oxidized at 1000 °C for 20 minutes.

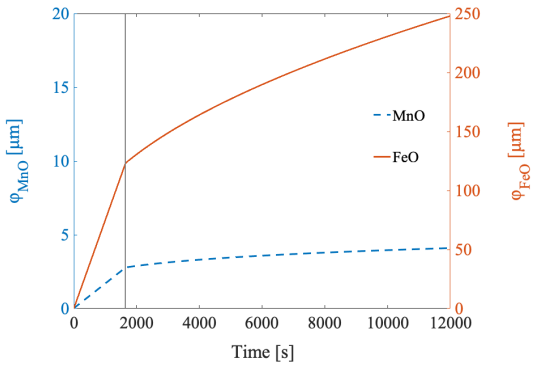

Figure 4.14: Calculated amount of each oxide as a function of time, when Fe-8Mn alloy is oxidized at 1000 °C in 20 kPa oxygen atmosphere with a gas flow rate of 250 mL min^{-1}; the transition time is indicated by the vertical line.

Since the dissociation oxygen partial pressure of MnO is less than that of FeO, the onset of oxidation starts with the preferential oxidation of Mn from the alloy. However, due to low Mn content and the rapid scale growth, the Mn interfacial mole fraction instantly (within the first time steps) drops. The early stage of oxidation then begins with the formation and development of FeO and MnO at the same time. The total amounts of MnO and FeO forming within the 20 minutes of oxidation are shown in Figure 4.14. Within the linear regime, only the most stable oxide phases of iron and manganese can form (i.e. FeO and MnO). It is known that when the growth regime is changed to parabolic, the other oxide phases (magnetite and hematite) are stable to form as well [101]. However, even during the parabolic growth most of the oxide scale consists of wüstite.

4.5. Conclusions

The in-situ methods for investigating the high-temperature oxidation behavior of alloys are limited, and it is practically impossible to experimentally access the alloy microstructure and composition in that condition. Measurements at room temperature require fast cooling to avoid homogenization; however, fast cooling can lead to phase transformations which also change the material. Therefore, to

study such a process, a numerical model was developed. The methodology of such a model is developed and verified by experiments before in several works [115, 116, 127]. The kinetic data necessary as input for the simulations were obtained from a series of TGA experiments. Iron with 1, 3, and 8 wt% Mn were oxidized at 950-1150 °C in gas mixtures with 10-30 kPa oxygen partial pressure and linear gas flow rates of 26.6 to 250 mL min^{-1} in a furnace tube of 15 mm inner diameter. The following conclusions can be drawn:

1. Considering the composition profile of Mn within the alloys and the depleted zone after the oxidation, temperature change plays an important role. Increasing the temperature increases the depleted zone due to the faster diffusion of Mn within the alloy.

2. Increasing the oxygen partial pressure of the oxidizing gas mixture leads to faster linear growth of the oxide scale when only FeO and MnO form. Faster oxidation results in higher O/M recession and a thinner Mn depleted zone.

3. The ratio between Mn and Fe within the oxide layer can be predicted via the introduced simulations. Therefore, the amount of Mn that the alloy has lost during the high-temperature oxidation can be calculated.

The ability to predict the initial high-temperature oxidation of alloys in various oxidizing conditions can help to control the surface behavior of steels at high-temperature processing. Further developments on other iron binary or ternary alloys will be necessary, in order to give more insights regarding the role of different alloying elements on the oxidizing behavior of the alloys.

5

Predicting the Parabolic Growth Rate Constant for High-Temperature Oxidation of Steels Using Machine Learning Models

The parabolic growth rate constant (k_p) of high-temperature oxidation of steels is predicted via a data analytics approach. Four machine learning models including Artificial Neural Networks, Random Forest, k-Nearest Neighbors, and Support Vector Regression are trained to establish the relations between the input features (composition and temperature) and the target value (k_p). The models are evaluated by the indices: Mean Absolute Error, Mean Squared Error, Root Mean Squared Error, and Coefficient of Determination. The steel composition regarding Cr and Ni content and the temperature were the most significant input features controlling the oxidation kinetics.

This chapter has been published in [6] by S. Aghaeian, J.C. Brouwer, W.G. Sloof, J.M.C. Mol, and A.J. Böttger, "Numerical Model For Short-Time High-Temperature Isothermal Oxidation of Fe–Mn Binaries at High Oxygen Partial Pressure." High Temperature Corrosion of Materials **(2023)**: 1-18.

5.1. Introduction

High-temperature oxidation occurs at different stages of steelmaking. The oxidation reaction can significantly influence the steel properties, including the near-surface composition, wettability, corrosion performance, mechanical properties, etc. Therefore, knowing the oxidation behavior of the alloys is of great importance. Currently, evaluating the alloys' high-temperature oxidation occurs through lengthy and costly experimental trials. Hence, developing the capability of predicting the oxidation behavior of steels in a variety of conditions is highly desirable. Although analytical [2, 65, 4] and numerical [66, 126, 115, 116, 5] simulations have significantly improved the high-temperature oxidation investigations, they are usually applicable for specific material compositions or a given oxidizing condition such as exposure time and gas mixture composition.

Facing the limitations of the conventional modeling approaches in the field of materials science, together with recent improvements in machine learning (ML) techniques, open a pathway to the use of data analytics to predict the properties of materials [128, 133, 139, 23, 122, 21]. Such algorithms have many advantages in providing insight into complex experiments on multi-component alloys. For instance, recent data analytics techniques in the design and development of new materials lead to a lower cost and can be considered as an alternative for experiments [153, 21, 122].

Despite the successful application of ML algorithms in the field of materials science, very limited studies addressed predicting high-temperature oxidation kinetics of alloys via data analytics approaches. In a recent work by Peng et al. [122] on NiCr-based alloys, a couple of different ML approaches have been applied to an experimental dataset to predict the parabolic growth rate constant (k_p) of oxidation. Alloy composition and temperature were the parameters, and k_p in both isothermal and cyclic oxidation was the target variable. The key input features were identified by Pearson's correlation coefficient (PCC) [120]. The oxidation temperature was found to have the biggest impact on the parabolic constant in all cases. It was also observed that Cr content, as the major alloying element in the studied alloys, had the most negative correlation with k_p, i.e. reduces the oxide growth kinetic constant. This agrees with previous studies, which showed that the presence of Cr promotes the formation of an external chromia solid-state diffusion barrier that slows down the oxidation reaction [64, 165].

In another work by Bhattacharya et al. [21] ML algorithms were applied to predict the high-temperature oxidation kinetics of Ti alloys between 550 and 750°C. The alloy composition, constituent phase of the alloy, the temperature of oxidation, time for oxidation, oxygen and moisture content, and mode of oxidation were considered as the independent input features, and k_p was set as the target value. When the Gradient Boosting Regressor algorithm [56] was employed, a good agreement was achieved between the experimental and the predicted k_p. Anirudh et al. [11] applied several ML models with a bottom-up approach (i.e. focussed on a very specific range of features) to predict the kinetics of elevated temperature cyclic oxidation of Fe-Cr and Fe-Cr-Ni alloys between 650 and 800°C in 10 % water vapor. The amount of Ni and Cr, temperature, and time were con-

sidered the independent input features, while the mass change was the target value. In that case, CastBoost was found to give the best performance among all the ML models. On the other hand, in a work by Taylor et al. [153], oxidation kinetics for some grades of steels, as well as other corrosion-resistant alloys, were investigated via machine learning models with a top-down approach (i.e. including a large range of features). Therefore, the effects of many features including the wide range of composition, temperature, and gas environment were considered in the models. The models were applicable for more varied oxidizing circumstances since they had multiple features and a wide range for each, but they subsequently had substantial prediction errors. Finally, they found Ni, Cr, Al, and Fe to be the most significant elements controlling the oxidation kinetics.

Additionally, deep learning methods such as Artificial Neural Network (ANN) models have significantly influenced the development of materials and associated processes [20, 75, 48, 84, 185, 80, 49]. This is because these models can deal with complex problems in materials science, where the target value depends on a large number of variables. However, there are distinct patterns that knowledgeable metallurgists can recognize and comprehend. As shown by the work of Dewangan et al. [48] ANN is applicable to predict the oxidation kinetics of high entropy alloys (HEA). The composition of the alloys, oxidation time, and temperature were chosen as input parameters, while the mass gain of the oxidized sample was the output of the ANN model. Finally, it was shown that the ANN model predicts the high-temperature oxidation behavior of HEA in a consistent and precise manner. Kim et al. [84] analyzed the high-temperature oxidation resistance of Ni-based superalloys using the ANN model. Finally, although ML algorithms have been successfully applied for predicting the oxidation behavior of several alloys, there is very limited work on steels with a broad range of alloying element content.

Our literature review reveals no works on employing ML models for predicting oxidation kinetics for a variety of steel compositions, in air. Such high-temperature oxidation behavior is observed in the hot rolling process, which involves exposing heated sheets to air to cool down, which can have a substantial impact on the steel performance and quality. In comparison to conventional steel development approaches based purely on limited experimental investigations or physical-based simulations, machine learning (ML) has the benefit of combining computational tools with experiments to forecast such oxidation behavior, having the potential to decrease development costs and time.

Here, a data analytics work is presented, which includes a correlation analysis of the high-temperature oxidation of a wide range of steels based on reported experimental data. In our work, the focus is on predicting the high-temperature oxidation kinetics of different steels, regardless of their phases, numerically represented by k_p. Because of having complex oxidation mechanisms, a broad, physics-based simulation of composition-dependent oxidation behavior is not yet feasible for steels. Correlation analysis was performed by PCC to find the interaction strengths between the input features (material and physical descriptors) and k_p statistically and rank them. Four widely used ML models were employed:

Artificial Neural Network (ANN), Random Forest (RF), *k*-Nearest Neighbors (KNN), and Support Vector Regression (SVR). The performance of the models in predicting the k_p values was evaluated by different metrics and discussed.

5.2. Methods

5.2.1. Dataset

Most of the reported experimental works on high-temperature oxidation of steels, focus on the steady-state parabolic scaling kinetics where the oxide growth rate is controlled by diffusion. Therefore, as a first step, a simple parabolic law (Equation (5.1)) was chosen to describe the high-temperature oxidation kinetics

$$\left(\frac{\Delta m}{A}\right)^2 = k_p t \tag{5.1}$$

where Δm is the mass gain in g, A is the specimen surface area in cm^2, t is time in s, and k_p is parabolic oxidation constant in $g^2\ cm^{-4}\ s^{-1}$. Parabolic growth rate constants, k_p, were collected directly from published reports [102, 4, 81, 112, 137, 34, 32, 180, 189, 40, 69, 191, 177, 79, 136, 188, 140, 57, 168, 15, 169, 83, 147, 186, 158, 85, 25, 150, 27, 151] where they were obtained from the mass gain results provided by Thermogravimetric analysis (TGA). The steps to get the parabolic growth rate constant are typically the same and begin with plotting the mass gain data on a squared mass gain vs. time plot. Then, a line is fitted to the linear part of the plot that represents the parabolic growth, and the slope of the fitted line would be the parabolic constant k_p. It is important to note that the dataset preparation was a manual literature survey to obtain values for k_p, without any extrapolation or interpolation. In this work, the focus is on the effect of steel composition and temperature (as input features) on oxidation kinetics k_p (target value). It is noted that data from the theoretical calculations were not included.

The collected dataset was tabulated for 76 different steel grades exposed to dry air at temperatures between 500 and 1200 °C. Within the data collection process, the dataset was visualized and studied at different stages to fill in the missing points. Finally, from a large amount of literature, 31 references were selected to prepare the dataset of 162 data points. It is not claimed to be a comprehensive dataset, but it will be shown later that it is enough to give precise quantitative predictions. The steel composition ranges, experimental conditions, and dataset details are shown in Table 5.1. The distribution of the dataset for temperature is shown in Figure 5.1 as an example. The detailed information about the distribution of data for all of the features and the target value is depicted in Figure B.2 and Figure B.1, respectively in the appendix. To identify gaps in the experimental dataset and suggest experiments to improve model predictions, ML can ultimately be effectively merged with the automated design of experiment methods in future research.

Investigating the high-temperature oxidation of multi-component alloys and, specifically, steels is a complex process that requires information about the thermodynamics and kinetics of the reaction [181]. The parabolic growth rate con-

Table 5.1: List of the alloying elements range in wt%, oxidizing condition, and dataset details.

Steel composition	Fe (47.91-100), Mn (0-40), Cr (0-25), Al (0-14.33), C (0-0.82), Si (0-7.2), Ni (0-24.59), Cu (0-2.65), S (0-0.048), P (0-0.22)
Commercial grade	Crofer 22 APU, Crofer 22 H, SUS 310S, SUS 430, AISI 304, AISI 430, AISI 439, AISI 441, AISI 1018, HR3C, AFA, SIMP, FHSS, HSLA
Temperature, °C	500-1200
Atmosphere	Dry air
Input features	Elemental composition in wt%, and oxidation temperature
Target value, $g^2cm^{-4}s^{-1}$	Parabolic growth rate constant ($k_p = 3.2 \times 10^{-15} - 1.21 \times 10^{-4}$)

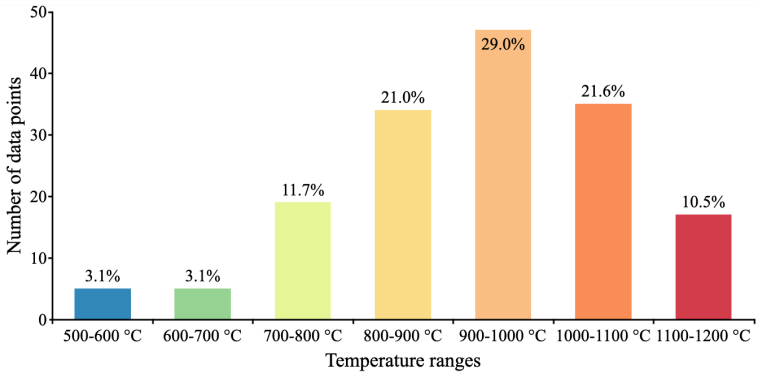

Figure 5.1: Temperature distribution of the dataset between 500 and 1200 °C. The values on the bars show the portion of the data points in that range.

stant (k_p) includes this information about the material and conditions in high-temperature oxidation implicitly [21, 122]. Such information encompasses the composition, temperature, gas mixture, etc. Since high-temperature oxidation in wet air has a different mechanism [181], only data for dry air has been collected for this work. ML algorithms utilize the collected data during the training process to predict the target value (k_p) for the testing data. However, the values for k_p were very small and it was difficult to visualize the differences between the calculated values. Therefore, by applying a logarithmic transformation (natural logarithm) of (k_p), the target value is converted. Therefore, the ML models in use will estimate the value of $\ln k_p$.

5.2.2. Correlation analysis and machine learning models

To identify the effect of each input feature on (k_p) and the interaction between different features, a PCC correlation analysis was conducted. PCC calculates the magnitude of the linear relationship between different features and allocates a

value between 1 and -1. Positive and negative values, respectively, show a correlation and anti-correlation, while zero indicates no correlation. A correlation analysis facilitates the training of the ML model with the top-ranking features, which are the input features with the highest absolute value of correlation with the target.

The dataset was split into training and testing sets in a range of 60% to 95% and 40% to 5% of the dataset, respectively. As shown in Figure B.3, smaller test sizes lead to high performances, but it is not reliable since the models are not tested with a sufficient number of data points and lead to unreproducible results. On the other hand, larger test sizes reduce the size of the training such that the reliability of the predictions is limited. A train and test size of respectively 80% and 20% were chosen as an optimum for reliable results. The data points were randomly distributed to the training and test sets by applying shuffling to the data before the split, which ensures the reproducibility of the results.

Four different models were employed to predict the parabolic growth rate constant (k_p): (a) Artificial Neural Network (ANN) [20], (b) Random Forest (RF) [76], (c) *k*-Nearest Neighbors (KNN) [7], and (d) Support Vector Machine (SVM) [13]. The regressor models of RF, KNN, and SVM were taken from Scikit-learn [121] sub-libraries to predict the continuous values of the target value (k_p). For ANN implementation, Keras was used, which is the high-level library built on top of TensorFlow [1]. Sequential and Dense models from the Keras library were used to add dense Neural Network layers. In addition, ReLU (Rectified Linear Unit) and Linear functions were employed respectively in hidden layers and the output layer.

In the KNN, the average number of neighbors for a given data point, or the *k*-nearest neighbors, is output by this non-parametric regression model. RF is a supervised learning technique that leverages the ensemble learning approach for regression. The ensemble learning method combines predictions from various ML algorithms (trees) to provide more accurate predictions than those from a single model. SVM is a powerful algorithm that allows choosing the tolerance of errors, both through an acceptable error margin (ϵ) and through tuning the tolerance of falling outside that acceptable error rate. Linear Regression (LR) [55] which is the most basic and commonly used predictive analysis algorithm was also employed in this work. It fits a linear equation to relate the input and output variables; however, the results are only described in the appendix due to lower accuracy.

To cover a wider class of ML algorithms, Artificial Neural Networks (ANNs) were used. ANNs are inspired by the biological nervous system and use interconnected mathematical nodes, also known as neurons, to describe complicated functional relationships. A typical ANN has input, hidden, and output layers. Building blocks of each layer are neurons that work as computational operation units. A neuron takes inputs from previous neurons, multiplies them by weights, and finally adds them up. Then this information is translated into output information by an activation function, and it can be used as input by other layers of neurons. This process is called feed-forward propagation, which generates the

output layer. In addition, a back-propagation process is needed to update the weight values and improve system performance.

Other than training and test sets, in ANN there is a validation set that is different from the test dataset, and its role is to test the trained model but within the training phase. During training, the model is evaluated on the validation dataset after each epoch to see how well it is generalizing to new, unseen data. For the ANN model, the data points are randomly distributed between training, validation, and test data sets with a 0.6:0.2:0.2 ratio, respectively.

5.2.3. Evaluation of models

The ML models mentioned above were trained with different proportions of training data and by considering different numbers of top-ranking features found via PCC analysis. Then, the performance of each model was evaluated with four metrics [41]: (a) Mean Absolute Error (MAE), (b) Mean Squared Error (MSE), (c) Root Mean Squared Error (RMSE), and (d) Coefficient of Determination (R^2) (see Equations (5.2) to (5.5)),

$$R^2 = 1 - \frac{\sum_{k=1}^{n} (y_k - \hat{y}_k)^2}{\sum_{k=1}^{n} (y_k - \bar{y})^2} \tag{5.2}$$

$$\text{MSE} = \frac{1}{n} \sum_{k=1}^{n} (y_k - \hat{y}_k)^2 \tag{5.3}$$

$$\text{MAE} = \frac{\sum_{k=1}^{n} |\hat{y}_k - y_k|}{n} \tag{5.4}$$

$$\text{RMSE} = \sqrt{\frac{\sum_{k=1}^{n} (\hat{y}_k - y_k)^2}{n}} \tag{5.5}$$

where y_k = measured k_p value, $\hat{y}_k$ = predicted k_p value, $\bar{y}$ = mean k_p value, and n = number of data points.

5.3. Result and Discussion

5.3.1. Correlation analysis

The correlation coefficient between all the variables (input features and the target value) is presented in Figure 5.2. While Fe content is the balance of the remaining alloying elements as the base element, it is important to note that Fe content is still utilized as an input feature because ML algorithms only solve mathematical problems and do not recognize this correlation. The last row and the last column of the matrix in Figure 5.2 show the correlation between the features on the target value, and the absolute values show the magnitude of each feature's influence on the target value (see Section 5.2.2). The amount of Cr was identified to have the most significant negative impact on $\ln(k_p)$ among all the features. It was also found that the oxidation temperature had the second-highest impact

on the target value. Fe and Ni were the third and fourth top-ranking features, respectively.

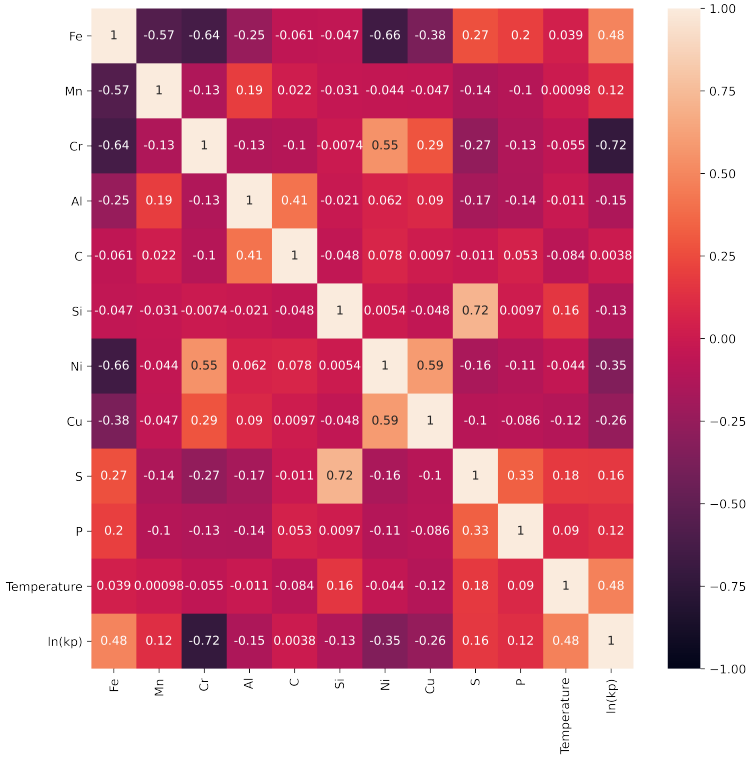

Figure 5.2: Graphical representation of the correlation between the input features and $\ln(k_p)$ for the training set determined using the PCC method.

The findings from the correlation analysis were in agreement with the current oxidation knowledge [181]. For instance, it is known that increasing the amount of Cr in steels, promotes the formation of the external chromia solid-state diffusion barrier, which results in a slower oxidation reaction and a lower value of k_p [109, 110], which is consistent with the big negative correlation value (-0.72) between Cr and $\ln(k_p)$. Moreover, iron produces rapidly forming oxides, and it has the highest positive correlation with $\ln(k_p)$ [43]. PCC also correctly identified that temperature has a high positive correlation with the target value (0.48). This is well-explained because increasing the temperature in the parabolic regime - which is known to be controlled by diffusion- can accordingly lead to higher k_p values [178]. It can also be observed in Figure 5.2 that Ni has a large negative correlation with the target value. Such correlation, which is due to the formation of protective oxides, has been seen and discussed before in the literature [43, 181, 11]. Moreover, the relative effect of the absolute correlation values of different features could also be analyzed. For instance, the bigger correlation value

of Cr-ln(k_p) compared with temperature-ln(k_p) was in agreement with the results found in previous experimental [30] and machine learning [11] works.

The aim of this correlation study is not only to acquire information about how input features affect k_p, but also to implement it for finding the top-ranking input features for ML model training and to study the effect of this selection on model performance.

5.3.2. The performances of machine learning algorithms

Four different algorithms (ANN, RF, KNN, and SVM) are trained and their performances have been evaluated by four metrics of MAE, MSE, RMSE, and R^2. In each of the employed models, there are several hyperparameters that can be tuned. Some parameters such as the number of considered top-ranking input features, and the test/training dataset ratio are applicable for all of the employed models and can be optimized for each separately. However, each model can have its own specific hyperparameters as well. For instance, the number of trees in RF, the number of neighbors in KNN, or the number of hidden layers and nodes in ANN.

The final structure of ANN used in this study is shown in Figure 5.3. It can be seen that the four top-ranking features are considered to be the input nodes. The developed ANN has one input layer with 4 neurons, three hidden layers with 128, 64, and 32 neurons, and an output layer with 1 neuron. The linear activation function with Adam optimizer [86] showed the best result in 1000 epochs [44]. An epoch is a hyperparameter that determines how many times the learning algorithm will run over the whole training dataset. Every sample in the training dataset has had a chance to update the internal model parameters once during an epoch.

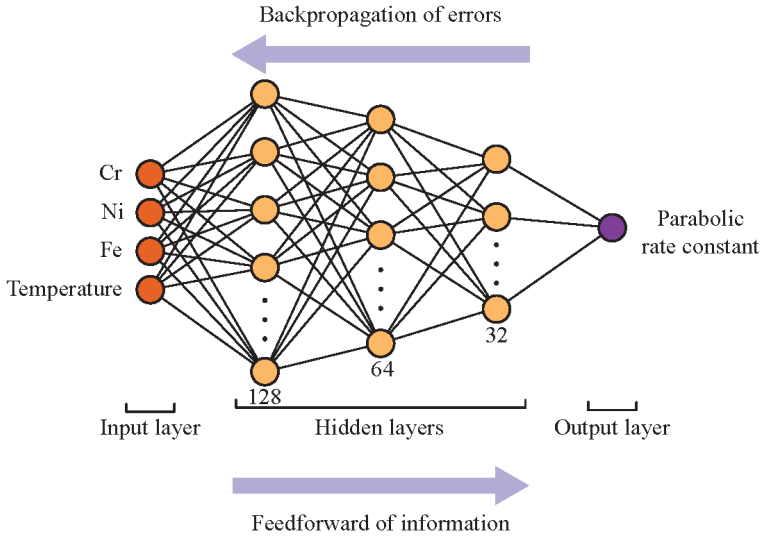

Figure 5.3: Graphical view of the ANN model with the parameters used in this work.

The effect of the considered number of top-ranking features on the performance of each model is shown in Figure 5.4. The top-ranking features are taken from the |PCC| ranking (the absolute values in Figure 5.2). Results indicate that, to varying degrees, the models are sensitive to the number of considered features in training. ANN, RF, and KNN showed better performances by reaching $R^2 > 0.9$, while SVR could not surpass 0.7. Generally, increasing the number of considered top-ranking features to 3 increased the performances of the models significantly. For SVR and RF, considering more than 3 features did not considerably enhance the efficiency of the models. On the other hand, KNN and ANN reached maximum efficiency when using the top 7 to 10 features.

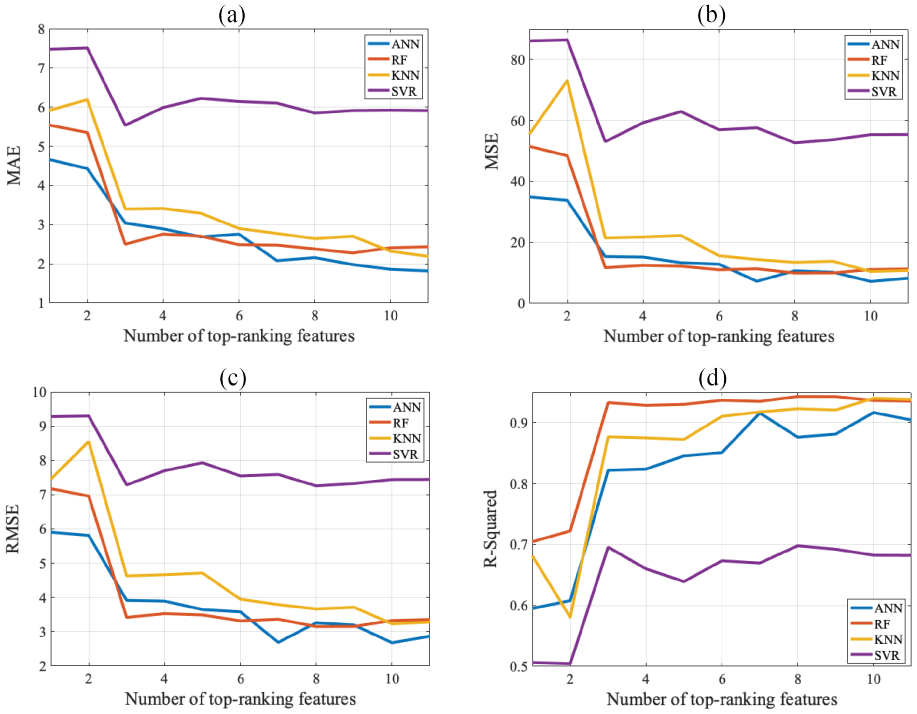

Figure 5.4: The performances of the ML models (KNN, RF, SVM, and ANN) as a function of the number of top-ranking features evaluated by (a) MAE, (b) MSE, (c) RMSE, and (d) R-squared indices.

Furthermore, the different indices show approximately the same trends in terms of the number of features' influence on the performances. While R-squared (Figure 5.4 (d)) shows a clear difference in the precision of the models (RF>KNN>ANN>SVR), the other indices (Figure 5.4 (a), (b), and (c)) show a comparable performance for ANN, RF, and KNN. However, it is worth mentioning that the computational cost for models such as ANN is much more than SVR. In our work, the execution time for the models was measured in the code and the approximate ratio was 1:1:12:2671, for SVR, KNN, RF, and ANN, respectively. So, in (industrial) applications where the dataset is huge, the calculation time is an

important parameter in choosing the most efficient model.

From Figure 5.2 and Figure 5.4, it is clear that employing just 3 features makes the predictions comparable to those made with all 11 features. In other words, adding features with lower PCC absolute values did not increase the accuracy of the predictions. However, it is worth mentioning that such observation is only based on the prepared dataset which is made from the available experimental results on HT oxidation of steels. Therefore, the results are limited to the included range of features and not beyond that.

The performances of the employed ML models trained with four top-ranking input features are indicated in Table 5.2. Regarding all four indices, and for models trained with the four top-ranking features, RF and SVR had the best and the worst performances, respectively. It can be seen that ANN and KNN models show comparable performances evaluated via different indices. For instance, the R-squared value shows better performance of KNN compared with ANN, while the other indices show the opposite.

Table 5.2: Performance comparison of ML models trained with four top-ranking features over the mean absolute error (MAE), mean squared error (MSE), root mean squared error (RMSE), and coefficient of determination (R^2).

	MAE	MSE	RMSE	R^2
RF	2.65	11.86	3.44	0.93
KNN	3.41	21.77	4.67	0.87
ANN	2.89	15.17	3.89	0.82
SVR	5.99	59.30	7.70	0.66

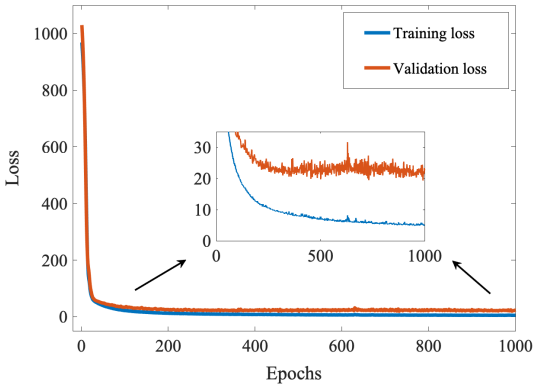

Figure 5.5: Comparison of training and validation losses in ANN model.

The training and validation losses over time for the ANN model are shown in Figure 5.5. The training loss indicates how well the model fits the training data, while the validation loss shows how well the model is adapting to the unseen data. The MAE metric is implemented to evaluate the performance of the ANN model by calculating the validation loss, and MSE is used to minimize the loss function and determine the training loss throughout the training process. It is shown that both losses are going down, which means that the predictions are good and the error is decreasing (no under-fitting). On the other hand, there is no divergence between the lines at longer times (higher epochs), and the validation loss does not increase, which shows that the ANN model is good at predicting the new data (no over-fitting).

For RF to perform at its best in this study, the top three features had to be

included; after that, the performance was virtually completely independent of the number of features taken into account. The same trend was seen for the RF model in a previous work [122]. Such a trend is understandable because as an ensemble learning method, RF gives varied importance to each feature during model training; as a result, fewer important features would have less or even no contribution to its performance. This leads to a performance that is not sensitive to the number of features when the maximum accuracy is achieved.

The performances of all four models in predicting the target value for the testing data points when they were trained with four top-ranking features have been visualized in Figure 5.6. These plots show the comparison between the predicted and actual k_p values. The blue lines depict the case when the actual and predicted values are identical (perfect prediction), and the red dots are the testing dataset. All four graphs show the predicted results from models tested with 20% of the dataset, which means 32 data points. Therefore, having the red points close to the blue line means a good prediction for the models. It can be seen that all the models except SVR could reasonably predict the k_p for high-temperature oxidation of steels. Furthermore, RF is clearly generating more precise values for k_p. Similar to what was reported in Table 5.2, it can also be seen in Figure 5.6 that the performances of ANN and KNN are relatively comparable. While R-squared shows slightly better results for KNN, the other indices show significantly lower errors in ANN predictions. Such a difference relates to the nature of the indices and the way that they calculate the errors [41] (see Equations (5.2) to (5.5)).

A general summarizing schematic of this data-driven work is shown in Figure 5.7, from stating the problem to finalizing the predictions via the trained ML models.

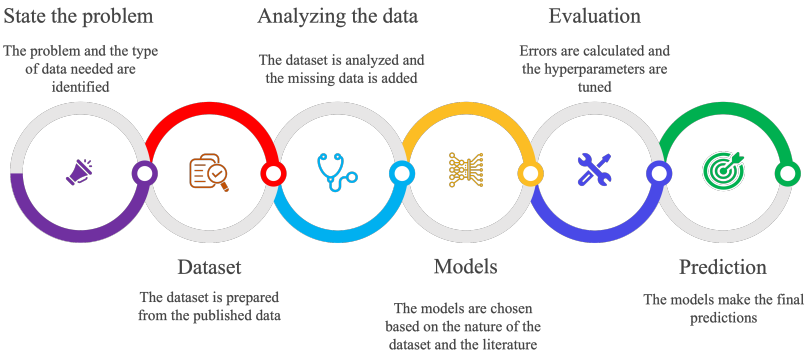

Figure 5.7: A general schematic of the steps taken in this work.

5.4. Conclusion

The kinetic data (k_p) for high-temperature oxidation of a wide range of steel grades, regardless of their phases, in dry air was extracted from published data. Four different machine-learning models namely ANN, RF, KNN, and SVR were employed

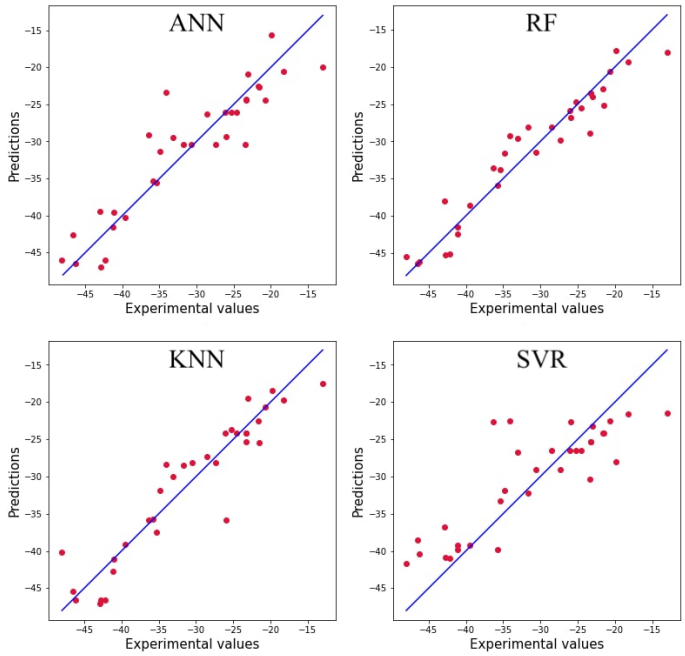

Figure 5.6: Actual values of experimental parabolic growth rate constants of high-temperature oxidation compared with values obtained from the ML models (ANN, RF, KNN, and SVM), where all the models were trained with four top-ranking features and tested with 20% of the dataset (32 red dots).

to predict k_p using the Phyton-libraries: Scikit-learn and TensorFlow. The models were evaluated by MAE, MSE, RMSE, and R-squared indices, and they were improved by optimizing the hyperparameters to get their best performance. The most significant features controlling the oxidation kinetics were the Cr, Fe, and Ni content as well as the temperature. Moreover, the models could successfully establish the relationship between the input features (composition and temperature) and the target value (k_p). Finally, it was shown that including more than three features, did not significantly improve the ML predictions. However, when trained with four top-ranking features, RF was found to have the smallest error in predictions, while KNN and ANN were shown to have almost the same prediction accuracy. SVR showed the largest errors in predicting the target value. The knowledge gained from this work can be useful in predicting the oxidation behavior of newly designed steel grades at different steps of the steel-making process where high-temperature oxidation can happen. It is possible with the valuable quantitative information provided about the correlation values of different features. Furthermore, the described method can be applied to datasets for other alloys, or investigate the effect of other features such as the components of the gas environment and their partial pressures on the kinetics of oxidation. In the end, in order to discover gaps in the experimental dataset and suggest ex-

periments to improve the model predictions even further, machine learning can be effectively integrated with the automated design of experiment techniques.

6

General Conclusions & Outlook

6.1. Conclusions

The main objective throughout the present work has been to develop a generic approach to predict the HT oxidation behavior of steel sheet in the hot-rolling process. The focus was on key oxidation characteristics, including the oxide growth rate, composition, and its impact on the underlying alloy in terms of depletion of the alloying elements and shifting of the oxide/metal interface. The whole work aims to minimize the number of trial-and-error experiments required for process development and optimization.

The significance of developing a predictive method for HT oxidation is crucial, particularly in processes like hot-rolling, which entails highly oxidizing conditions. It usually occurs within the temperature range of 900 to 1100 °C in an oxygen-rich environment (air), facilitating rapid oxidation that occurs within a minute, making it challenging to measure directly. Therefore, a model capable of forecasting the growth rate and composition of the oxide with good accuracy proves to be immensely valuable to the industry.

In the presented work, HT oxidation of steels has been investigated from different perspectives. Initially, experimental work is carried out to serve as the groundwork and to generate the input for the computations. Subsequently, a numerical model is formulated based on diffusion mechanisms within the steel. Lastly, the kinetics of HT oxidation for different steel grades are predicted via a data-driven approach employing several ML models. The conclusions drawn from the present work are summarized here:

- Wagner's models laid the groundwork for predictive approaches concerning the kinetics of HT oxidation in alloys. Subsequently, the scientists built their own models using Wagner's theories to include additional parameters. Nevertheless, the predictive capabilities of diffusion-based models in the oxidation of alloys are limited, especially when the oxidation mechanism is not well understood, which is frequently the case. For instance, elucidating the HT oxidation mechanism in steels with diverse alloying elements remains a challenge due to the interplay of various influencing parameters that can either mitigate or intensify each other's effects. Another example of the challenge in identifying the oxidation mechanism is where the gas mixture contains water vapor.

- HT oxidation experiments were conducted using TGA on iron samples containing varying manganese content, ranging from zero to approximately 5 wt.%, at temperatures within the range of 950 to 1150 °C. The samples were exposed to an oxidizing gas with oxygen partial pressures ranging from 10 to 30 kPa with flow rates of 26.6 and 53.3 sccm (Standard Cubic Centimeters per Minute) for 20 minutes. The mass gain results indicated a linear growth rate of the oxide scale for almost all of the samples. While temperature and Mn content had no significant effect on the kinetics of oxidation, increasing the oxygen partial pressure and the flow rate, remarkably raised the linear kinetic constant of oxidation.

- In the same experiments with lower flow rates, it was observed that the rate-controlling step for the oxidation reaction within the first 20 minutes of oxidation was the gas-phase mass transfer through a laminar boundary layer. Particularly, the oxidation rate varied between the leading and trailing edges of the sample, mainly due to the substantial difference in the boundary layer thickness at different locations. Consequently, thicker oxide layers formed on the top of the sample, while thinner ones were observed at the bottom. During the HT oxidation, the scale primarily consisted of wüstite as the only oxide phase. However, since the cooling rate in TGA was relatively slow, around 10 °C/min, the wüstite phase transformed to magnetite.

- The numerical model was employed to calculate the composition profile of Mn within the alloys during and after oxidation, revealing the significant influence of temperature changes. Higher temperatures led to an expanded depleted zone due to enhanced Mn diffusion within the alloy. Moreover, increased oxygen partial pressure in the oxidizing gas mixture accelerated the linear growth rate of the oxide scale, when only FeO and MnO form, resulting in increased O/M recession and a thinner Mn-depleted region. Based on the mass balance at the O/M interface, the model also facilitated the calculation of the oxide scale composition, offering valuable insights into the oxidation process and its impact on the alloy composition.

- As previously stated, the presence of multiple alloying elements in more intricate steels adds complexity to the oxidation mechanism, rendering the direct calculation of their oxide growth rate currently unfeasible. Therefore, it is proposed to utilize machine ML models to predict the growth rate constants. Kinetic data (k_p) for the HT oxidation of various steel grades, independent of their phases, in dry air was extracted from published literature. Four different ML models, namely Artificial Neural Network (ANN), Random Forest (RF), k-Nearest Neighbors (KNN), and Support Vector Regression (SVR), were employed to predict k_p. The models' performance was evaluated using metrics like Mean Absolute Error (MAE), Mean Squared Error (MSE), Root Mean Squared Error (RMSE), and R-squared indices, and their effectiveness was enhanced by optimizing hyperparameters. The most influential features governing oxidation kinetics were found to be the content of Cr, Fe, and Ni, along with the temperature. additionally, the models successfully established a correlation between input features (composition and temperature) and the target value (k_p). Interestingly, including more than three top-ranking features did not substantially enhance ML predictions. However, when trained with the top four features, RF exhibited the slightest prediction error, while KNN and ANN demonstrated comparable prediction accuracy. SVR showed the largest errors in predicting the target value.

6.2. Outlook

The research conducted in this thesis has provided valuable insights into the HT oxidation behavior of steels in the air. However, there are several routes for future investigations and improvements in this field.

Expanding the numerical model to include complex alloying elements is a crucial next step. While the model works well for Fe–Mn binary alloys, it should be noted that there are several other similar works on different alloys. However, expanding these models to more complex alloy systems is challenging because of the unknown oxidation mechanisms. To address this, a comprehensive experimental approach is necessary, under various oxidizing conditions and steel grades. Through advanced in-situ and ex-situ characterization techniques, the underlying mechanisms of oxidation could be elucidated, paving the way for the development of physics-based models tailored to predict oxidation behavior in complex scenarios. The experimental findings can also be utilized to address data gaps in data-driven approaches to reach higher predictive accuracy.

Additionally, while the numerical model and machine learning predictions have exhibited reasonable accuracy, it remains imperative to validate these results through rigorous experimentation. Experimental validation is necessary to investigate the real-world applicability and reliability of our models. Therefore, conducting more experiments is necessary to confirm the model predictions and make them more useful. Furthermore, to enhance model accuracy, it is advisable to conduct experiments with specific oxidizing conditions or distinct alloy compositions that have not been comprehensively explored in existing literature. To identify such knowledge gaps within the dataset and propose experiments aimed at refining the model predictions, the integration of machine learning with the automated design of experiment techniques offers a promising way for future research.

With the growing availability of experimental data, the potential for applying advanced data-driven techniques, particularly deep learning methods, becomes increasingly feasible. Collaborating with experienced data scientists is crucial to ensure the development of robust and reliable predictive models. Once these models are well-established, they can be extended to encompass datasets for alloys other than steel, expanding the scope of their application. Furthermore, there is an opportunity to explore the impact of additional variables, such as the composition of the oxidizing gas and partial pressures of its components, on oxidation kinetics. Including more features, such as sample size, surface roughness, and time, can further enhance the modeling accuracy. Additionally, the incorporation of target values, such as mechanical properties of the scale, oxidation mode, and Internal Oxidation Zone (IOZ) thickness, can provide a comprehensive understanding of HT oxidation behavior.

The developed predictive approach could have broader applications beyond HT oxidation in air. Exploring its applicability to other high-temperature processes in the steel industry, such as annealing or other heat treatments, could open up new possibilities for process optimization and material design. One of the most valuable applications for a predictive approach to the oxidation of iron

is in recently developed iron-air batteries. Such batteries work by oxidizing iron with oxygen from the air. When the system is delivering power, the iron particles combine with the oxygen drawn from the air to form iron oxide. When the system is recharging, the iron particles are regenerated and the oxygen is returned to the ambient air. The same applies to other metal-air batteries such as zinc-air batteries.

All in all, the work presented here has laid the groundwork for predicting the HT oxidation behavior of steels. By addressing the outlined outlook areas, further advancements can be made in understanding and optimizing the critical industrial processes, ultimately leading to improved material properties and efficiency in the steel manufacturing industry. So hopefully, it can play a role in achieving the goal of having a sustainable industry that respects environmental preservation, minimizes resource depletion, reduces waste generation, and fosters responsible manufacturing practices.

Bibliography

[1] Martin Abadi et al. "{TensorFlow}: a system for {Large-Scale} zrning". In: *12th USENIX symposium on operating systems design and implementation (OSDI 16)*. 2016, pp. 265–283.

[2] H Abuluwefa, RIL Guthrie, and F Ajersch. "The effect of oxygen concentration on the oxidation of low-carbon steel in the temperature range 1000 to 1250 C". In: *Oxidation of Metals* 46 (1996), pp. 423–440.

[3] HT Abuluwefa, RIL Guthrie, and F Ajersch. "Oxidation of low carbon steel in multicomponent gases: Part I. Reaction mechanisms during isothermal oxidation". In: *Metallurgical and Materials Transactions A* 28.8 (1997), pp. 1633–1641.

[4] S Aghaeian et al. "Initial High-Temperature Oxidation Behavior of Fe–Mn Binaries in Air: The Kinetics and Mechanism of Oxidation". In: *Oxidation of Metals* 98.1-2 (2022), pp. 217–237.

[5] S Aghaeian et al. "Numerical Model For Short-Time High-Temperature Isothermal Oxidation of Fe–Mn Binaries at High Oxygen Partial Pressure". In: *High Temperature Corrosion of Materials* (2023), pp. 1–18.

[6] Soroush Aghaeian et al. "Predicting the parabolic growth rate constant for high-temperature oxidation of steels using machine learning models". In: *Corrosion Science* (2023), p. 111309.

[7] Naomi S Altman. "An introduction to kernel and nearest-neighbor nonparametric regression". In: *The American Statistician* 46.3 (1992), pp. 175–185.

[8] WF Ames and C Brezinski. *Handbook of differential equations*. North-Holland, 1992.

[9] Jan-Olof Andersson and John Ågren. "Models for numerical treatment of multicomponent diffusion in simple phases". In: *Journal of applied physics* 72.4 (1992), pp. 1350–1355.

[10] Jan-Olof Andersson et al. "Thermo-Calc & DICTRA, computational tools for materials science". In: *Calphad* 26.2 (2002), pp. 273–312.

[11] MK Anirudh et al. "Artificial Intelligence Approach to Predict Elevated Temperature Cyclic Oxidation of Fe–Cr and Fe–Cr–Ni Alloys". In: *Oxidation of Metals* 98.3-4 (2022), pp. 291–303.

[12] Michael Auinger, E-M Müller-Lorenz, and Michael Rohwerder. "Modelling and experiment of selective oxidation and nitridation of binary model alloys at 700°C-The systems Fe, 1 wt.%{Al, Cr, Mn, Si}". In: *Corrosion Science* 90 (2015), pp. 503–510.

[13] Mariette Awad and Rahul Khanna. *Efficient learning machines: theories, concepts, and applications for engineers and system designers*. Springer nature, 2015.

[14] Hameed Al-Badairy and GJ Tatlock. "The application of a wedge-shaped sample technique for the study of breakaway oxidation in Fe–20Cr–5Al base alloys". In: *Oxidation of metals* 53 (2000), pp. 157–170.

[15] Tilen Balaško et al. "High-Temperature Oxidation Behaviour of Duplex Fe-Mn-Al-Ni-C Lightweight Steel". In: *Crystals* 12.7 (2022), p. 957.

[16] Ch W Bale et al. "FactSage thermochemical software and databases". In: *Calphad* 26.2 (2002), pp. 189–228.

[17] BD Bastow, DP Whittle, and G Cv Wood. "Alloy depletion profiles resulting from the preferential removal of the less noble metal during alloy oxidation". In: *Oxidation of Metals* 12.5 (1978), pp. 413–438.

[18] RE Bedworth and NB Pilling. "The oxidation of metals at high temperatures". In: *J Inst Met* 29.3 (1923), pp. 529–582.

[19] HL Bernstein. "A model for the oxide growth stress and its effect on the creep of metals". In: *Metallurgical transactions A* 18 (1991), pp. 975–986.

[20] HKDH Bhadeshia et al. "Performance of neural networks in materials science". In: *Materials Science and Technology* 25.4 (2009), pp. 504–510.

[21] Somesh Kr Bhattacharya, Ryoji Sahara, and Takayuki Narushima. "Predicting the parabolic rate constants of high-temperature oxidation of Ti alloys using machine learning". In: *Oxidation of Metals* 94.3-4 (2020), pp. 205–218.

[22] R Byron Bird. "Transport phenomena". In: *Appl. Mech. Rev.* 55.1 (2002), R1–R4.

[23] Frederic E Bock et al. "A review of the application of machine learning and data mining approaches in continuum materials mechanics". In: *Frontiers in Materials* 6 (2019), p. 110.

[24] William E Boggs. "The Oxidation of Iron-Aluminum Alloys from 450° to 900° C". In: *Journal of the Electrochemical Society* 118.6 (1971), p. 906.

[25] Valeria Bongiorno et al. "On the High-Temperature Oxidation and Area Specific Resistance of New Commercial Ferritic Stainless Steels". In: *Metals* 11.3 (2021), p. 405.

[26] Rune Bredesen and Per Kofstad. "On the oxidation of iron in CO_2+CO mixtures: II. Reaction mechanisms during initial oxidation". In: *Oxidation of Metals* 35.1 (1991), pp. 107–137.

[27] Tomasz Brylewski et al. "Application of Fe-16Cr ferritic alloy to interconnector for a solid oxide fuel cell". In: *Solid State Ionics* 143.2 (2001), pp. 131–150.

[28] P Carter, B Gleeson, and DJ Young. "Calculation of precipitate dissolution zone kinetics in oxidising binary two-phase alloys". In: *Acta Materialia* 44.10 (1996), pp. 4033–4038.

[29] Hobyung Chae et al. "Evaluation of Supercritical Carbon Dioxide Corrosion by High Temperature Oxidation Experiments and Machine Learning Models". In: *Metallurgical and Materials Transactions A* 53.7 (2022), pp. 2614–2626.

[30] Kamlesh Chandra et al. "High temperature oxidation behavior of 9–12% Cr ferritic/martensitic steels in a simulated dry oxyfuel environment". In: *Oxidation of Metals* 83 (2015), pp. 291–316.

[31] S Chandra-ambhorn, A Jutilarptavorn, and T Rojhirunsakool. "High temperature oxidation of irons without and with 0.06 wt.% Sn in dry and humidified oxygen". In: *Corrosion Science* 148 (2019), pp. 355–365.

[32] Somrerk Chandra-ambhorn, Thammaporn Thublaor, and Panya Wiman. "High temperature oxidation of AISI 430 stainless steel in Ar – H_2O at 800°C". In: *Corrosion Science* 167 (2020), p. 108489.

[33] A Chatterjee et al. "Kinetic modeling of high-temperature oxidation of Ni-base alloys". In: *Computational Materials Science* 50.3 (2011), pp. 811–819.

[34] Rex Y Chen and WY Yuen. "The effects of steel composition on the oxidation kinetics, scale structure, and scale-steel interface adherence of low and ultra-low carbon steels". In: *Materials science forum*. Vol. 522. Trans Tech Publ. 2006, pp. 451–460.

[35] Rex Y Chen and WYD Yuen. "Short-time oxidation behavior of low-carbon, low-silicon steel in air at $850 - 1180$°C –II. linear to parabolic transition determined using existing gas-phase transport and solid-phase diffusion theories". In: *Oxidation of Metals* 73.3 (2010), pp. 353–373.

[36] Rex Y Chen and WYD Yuen. "Short-time Oxidation Behavior of Low-carbon, Low-silicon Steel in Air at $850 - 1180$°C—I: Oxidation Kinetics". In: *Oxidation of Metals* 70.1 (2008), pp. 39–68.

[37] RY Chen and WYD Yuen. "Effects of the presence of water vapour on the oxidation behaviour of low carbon–low silicon steel in 1% O2–N2 at 1073 K". In: *Oxidation of metals* 79.5-6 (2013), pp. 655–678.

[38] RY Chen and WYD Yuen. "Longer Term Oxidation Kinetics of Low Carbon, Low Silicon Steel in 17H O_2-N_2 at 900 °C". In: *Oxidation of Metals* 85.5-6 (2016), pp. 489–507.

[39] RY Chen and WYD Yuen. "Oxidation of low-carbon, low-silicon mild steel at 450-900°C under conditions relevant to hot-strip processing". In: *Oxidation of Metals* 57.1-2 (2002), pp. 53–79.

[40] Lei Cheng et al. "High-Temperature Oxidation Behavior of Fe-10Cr Steel under Different Atmospheres". In: *Materials* 14.13 (2021), p. 3453.

[41] Davide Chicco, Matthijs J Warrens, and Giuseppe Jurman. "The coefficient of determination R-squared is more informative than SMAPE, MAE, MAPE, MSE and RMSE in regression analysis evaluation". In: *PeerJ Computer Science* 7 (2021), e623.

[42] DE Coates and AD Dalvi. "An extension of the Wagner theory of alloy oxidation and sulfidation". In: *Oxidation of Metals* 2.4 (1970), pp. 331–347.

[43] JE Croll and GR Wallwork. "The high-temperature oxidation of iron-chromium-nickel alloys containing 0–30% chromium". In: *Oxidation of Metals* 4.3 (1972), pp. 121–140.

[44] Ivan Nunes Da Silva et al. "Artificial neural networks". In: *Cham: Springer International Publishing* 39 (2017).

[45] AD Dalvi and WW Smeltzer. "A Diffusion Model for Oxidation of Nickel-Iron Alloys at 1000° C". In: *Journal of the Electrochemical Society* 121.3 (1974), p. 386.

[46] LS Darken. "Diffusion in metal accompanied by phase change". In: *MET TECHNOL* 9.5 (1942), pp. 1–13.

[47] MH Davies, MT Simnad, and CE Birchenall. "On the Mechanism and Kinetics of the Scaling of Iron". In: *Jom* 3 (1951), pp. 889–896.

[48] Sheetal Kumar Dewangan and Vinod Kumar. "Application of artificial neural network for prediction of high temperature oxidation behavior of AlCrFeMnNiWx (X= 0, 0.05, 0.1, 0.5) high entropy alloys". In: *International Journal of Refractory Metals and Hard Materials* 103 (2022), p. 105777.

[49] Sheetal Kumar Dewangan, Sumanta Samal, and Vinod Kumar. "Microstructure exploration and an artificial neural network approach for hardness prediction in AlCrFeMnNiW, X High-Entropy Alloys". In: *Journal of Alloys and Compounds* 823 (2020), p. 153766.

[50] DL Douglass. "The oxidation mechanism of dilute Ni-Cr alloys". In: *Corrosion Science* 8.9 (1968), pp. 665–678.

[51] J Ehlers et al. "Enhanced oxidation of the 9% Cr steel P91 in water vapour containing environments". In: *Corrosion science* 48.11 (2006), pp. 3428–3454.

[52] HJ Engell. "The concentration gradient of iron-ion-vacancies in wustite scaling films and the mechanism of oxidation of iron". In: *Acta Metallurgica* 6.6 (1958), pp. 439–445.

[53] HE Evans et al. "Influence of silicon additions on the oxidation resistance of a stainless steel". In: *Oxidation of Metals* 19 (1983), pp. 1–18.

[54] E Feulvarch, JM Bergheau, and JB Leblond. "An implicit finite element algorithm for the simulation of diffusion with phase changes in solids". In: *International Journal for Numerical Methods in Engineering* 78.12 (2009), pp. 1492–1512.

[55] David A Freedman. *Statistical models: theory and practice*. Cambridge university press, 2009.

[56] Jerome H Friedman. "Greedy function approximation: a gradient boosting machine". In: *Annals of statistics* (2001), pp. 1189–1232.

[57] Qiuzhi Gao et al. "High-temperature oxidation behavior of modified 4Al alumina-forming austenitic steel: Effect of cold rolling". In: *Journal of Materials Science & Technology* 68 (2021), pp. 91–102.

[58] G Garnaud and Robert A Rapp. "Thickness of the oxide layers formed during the oxidation of iron". In: *Oxidation of Metals* 11 (1977), pp. 193–198.

[59] David Gaskell. *An introduction to transport phenomena in materials engineering*. New York: Momentum Press, 2012.

[60] F Gesmundo and Y Niu. "The criteria for the transitions between the various oxidation modes of binary solid-solution alloys forming immiscible oxides at high oxidant pressures". In: *Oxidation of Metals* 50.1-2 (1998), pp. 1–26.

[61] F Gesmundo and Y Niu. "The formation of two layers in the internal oxidation of binary alloys by two oxidants in the absence of external scales". In: *Oxidation of Metals* 51.1-2 (1999), pp. 129–158.

[62] F Gesmundo and F Viani. "The formation of multilayer scales in the parabolic oxidation of pure metals—II. Temperature and pressure dependence of the different rate constants". In: *Corrosion Science* 18.3 (1978), pp. 231–243.

[63] Robert A Giddings and Ronald S Gordon. "Review of Oxygen Activities and Phase Boundaries in wüstite as Determined by Electromotive-Force and Gravimetric Methods". In: *Journal of the American Ceramic Society* 56.3 (1973), pp. 111–116.

[64] CS Giggins and FS Pettit. "Oxidation of Ni-Cr alloys between 800° and 1200°C". In: *Metallurgical Transactions* 1.4 (1970), pp. 1088–1088.

[65] L Gong et al. "Analytical model of selective external oxidation of Fe-Mn binary alloys during isothermal annealing treatment". In: *Corrosion Science* 166 (2020), p. 108454.

[66] L Gong et al. "Numerical model of selective external oxidation of Fe-Mn binary alloys during non-isothermal annealing treatment". In: *Corrosion Science* 178 (2021), p. 108921.

[67] AG Goursat and WW Smeltzer. "Kinetics and morphological development of the oxide scale on iron at 800° C in oxygen at 2.5× 10- 3 to 3.0× 10- 1 torr pressure". In: *Journal of The Electrochemical Society* 120.3 (1973), p. 390.

[68] SW Guan, HC Yi, and WW Smeltzer. "Internal oxidation of ternary alloys. Part II: Kinetics in the presence of an external scale". In: *Oxidation of Metals* 41.5-6 (1994), pp. 389–400.

[69] Mingxin Hao, Bin Sun, and Hao Wang. "High-temperature oxidation behavior of Fe-1Cr-0.2Si Steel". In: *Materials* 13.3 (2020), p. 509.

[70] William M Haynes, David R Lide, and Thomas J Bruno. *CRC handbook of chemistry and physics*. CRC press, 2016.

[71] R Herchl et al. "Short-circuit diffusion in the growth of nickel oxide scales on nickel crystal faces". In: *Oxidation of Metals* 4 (1972), pp. 35–49.

[72] AH Heuer. "Oxygen and aluminum diffusion in α-Al2O3: how much do we really understand?" In: *Journal of the European Ceramic Society* 28.7 (2008), pp. 1495–1507.

[73] AH Heuer et al. "On the growth of Al2O3 scales". In: *Acta Materialia* 61.18 (2013), pp. 6670–6683.

[74] Lawrence Himmel, RF Mehl, and C E_ Birchenall. "Self-diffusion of iron in iron oxides and the Wagner theory of oxidation". In: *JOM* 5.6 (1953), pp. 827–843.

[75] Bhadeshia Hkdh. "Neural networks in materials science". In: *ISIJ international* 39.10 (1999), pp. 966–979.

[76] Tin Kam Ho. "The random subspace method for constructing decision forests". In: *IEEE transactions on pattern analysis and machine intelligence* 20.8 (1998), pp. 832–844.

[77] A Hodgson, A Wight, and G Worthy. "The kinetics of O_2 dissociative chemisorption on Fe (110)". In: *Surface Science* 319.1-2 (1994), pp. 119–130.

[78] HS Hsu. "The formation of multilayer scales on pure metals". In: *Oxidation of metals* 26 (1986), pp. 315–332.

[79] Anne Marie Huntz et al. "Oxidation of AISI 304 and AISI 439 stainless steels". In: *Materials Science and Engineering: A* 447.1-2 (2007), pp. 266–276.

[80] Nusrat Islam, Wenjiang Huang, and Houlong L Zhuang. "Machine learning for phase selection in multi-principal element alloys". In: *Computational Materials Science* 150 (2018), pp. 230–235.

[81] PRS Jackson and GR Wallwork. "The oxidation of binary iron-manganese alloys". In: *Oxidation of Metals* 20.1-2 (1983), pp. 1–17.

[82] Torbjörn Jonsson et al. "An ESEM in situ investigation of the influence of H2O on iron oxidation at 500 C". In: *Corrosion Science* 51.9 (2009), pp. 1914–1924.

[83] CH Kao and CM Wan. "Effect of manganese on the oxidation of Fe-Mn-Al-C alloys". In: *Journal of materials science* 23.2 (1988), pp. 744–752.

[84] Hee-Soo Kim et al. "Regression analysis of high-temperature oxidation of Ni-based superalloys using artificial neural network". In: *Corrosion Science* 180 (2021), p. 109207.

[85] Insoo Kim, WD Cho, and HJ Kim. "High-temperature oxidation of Fe3Al containing yttrium". In: *Journal of materials science* 35.18 (2000), pp. 4695–4703.

[86] Diederik P Kingma and Jimmy Ba. "Adam: A method for stochastic optimization". In: *arXiv preprint arXiv:1412.6980* (2014).

[87] Per Kofstad. "High temperature corrosion". In: *Elsevier Applied Science Publishers, Crown House, Linton Road, Barking, Essex IG 11 8 JU, UK, 1988.* (1988).

[88] Oswald Kubaschewski and Bernarr Eugen Hopkins. *Oxidation of Metals and Alloys*. London: Butterworths, 1967.

[89] Ingard A Kvernes and Per Kofstad. "The oxidation behavior of some Ni-Cr-Al alloys at high temperatures". In: *Metallurgical Transactions* 3.6 (1972), pp. 1511–1519.

[90] Henrik Larsson and Anders Engström. "A homogenization approach to diffusion simulations applied to $\alpha+\gamma$ Fe-Cr-Ni diffusion couples". In: *Acta Materialia* 54.9 (2006), pp. 2431–2439.

[91] Henrik Larsson, Henrik Strandlund, and Mats Hillert. "Unified treatment of Kirkendall shift and migration of phase interfaces". In: *Acta Materialia* 54.4 (2006), pp. 945–951.

[92] Henrik Larsson et al. "Oxidation of iron at 600 C–experiments and simulations". In: *Materials and corrosion* 68.2 (2017), pp. 133–142.

[93] V Aghaei Lashgari. "Internal and external oxidation of manganese in advanced high strength steels". PhD thesis. Delft University of Technology, 2014.

[94] V Aghaei Lashgari, C Kwakernaak, and WG Sloof. "Transition from internal to external oxidation of Mn steel alloys". In: *Oxidation of metals* 81 (2014), pp. 435–451.

[95] V Aghaei Lashgari et al. "Kinetics of internal oxidation of Mn-steel alloys". In: *Oxidation of metals* 82 (2014), pp. 249–269.

[96] VHJ Lee, B Gleeson, and DJ Young. "Scaling of carbon steel in simulated reheat furnace atmospheres". In: *Oxidation of metals* 63 (2005), pp. 15–31.

[97] Veniamin Grigorevich Levich. *Physicochemical hydrodynamics*. Prentice-Hall Inc., 1962.

[98] RE Lobnig et al. "Diffusion of cations in chromia layers grown on iron-base alloys". In: *Oxidation of metals* 37 (1992), pp. 81–93.

[99] Jose A Loli et al. "Predicting Oxidation Behavior of Multi-Principal Element Alloys by Machine Learning Methods". In: *Oxidation of Metals* 98.5-6 (2022), pp. 429–450.

[100] Weichen Mao, Yao Ma, and Willem G Sloof. "Internal oxidation of Fe-Mn-Cr steels, simulations and experiments". In: *Oxidation of Metals* 90.1 (2018), pp. 237–253.

[101] William Mao. "Oxidation phenomena in advanced high strength steels: Modelling and experiment". PhD thesis. Delft University of Technology, 2018, pp. 103–122.

[102] AL Marasco and DJ Young. "The oxidation of Iron-Chromium-Manganese alloys at 900°C". In: *Oxidation of Metals* 36.1 (1991), pp. 157–174.

[103] C Martinez et al. "In-situ surface analysis of annealed Fe-1.5% Mn and Fe-0.6% Mn low alloy steels". In: *Analytical and Bioanalytical Chemistry* 374.4 (2002), pp. 742–745.

[104] Carlos Martinez et al. "In-situ investigation on the oxidation behaviour of low alloyed steels annealed under N_2-5% H_2 protective atmospheres". In: *Steel Research* 72.11-12 (2001), pp. 508–511.

[105] MATLAB. *version 9.8.0.1721703 (R2020a).* Natick, Massachusetts: The MathWorks Inc., 2020.

[106] P Mayer and WW Smeltzer. "Diffusional Growth of Cobaltous-Ferrous Oxide Scales on Cobalt-Iron Alloys". In: *Journal of the Electrochemical Society* 121.4 (1974), p. 538.

[107] P Mayer and WW Smeltzer. "Diffusional Growth of Cobaltous-Ferrous Oxide Scales on Cobalt-Iron Alloys". In: *Journal of The Electrochemical Society* 123.5 (1976), p. 661.

[108] P Mayer and WW Smeltzer. "Kinetics of Manganeseo-Wustite Scale Formation on Iron-Manganese Alloys". In: *Journal of the Electrochemical Society* 119.5 (1972), p. 626.

[109] HK Mehtani et al. "The oxidation behavior of iron-chromium alloys: The defining role of substrate chemistry on kinetics, microstructure and mechanical properties of the oxide scale". In: *Journal of Alloys and Compounds* 871 (2021), p. 159583.

[110] Gerald H Meier et al. "Effect of alloy composition and exposure conditions on the selective oxidation behavior of ferritic Fe-Cr and Fe-Cr-X alloys". In: *Oxidation of Metals* 74.5 (2010), pp. 319–340.

[111] Wanda Maria Carolina Melfo. "Analysis of hot rolling events that lead to ridge-buckle defect in steel strips". PhD thesis. University of Wollongong, 2006.

[112] Per A Munther and John G Lenard. "The effect of scaling on interfacial friction in hot rolling of steels". In: *Journal of Materials Processing Technology* 88.1-3 (1999), pp. 105–113.

[113] A Naoumidis et al. "Phase studies in the chromium-manganese-titanium oxide system at different oxygen partial pressures". In: *Journal of the European Ceramic Society* 7.1 (1991), pp. 55–63.

[114] JA Nesbitt and RW Heckel. "Modeling degradation and failure of Ni-Cr-Al overlay coatings". In: *Thin Solid Films* 119.3 (1984), pp. 281–290.

[115] TJ Nijdam, LPH Jeurgens, and W. G. Sloof. "Modelling the thermal oxidation of ternary alloys—compositional changes in the alloy and the development of oxide phases". In: *Acta Materialia* 51.18 (2003), pp. 5295–5307.

[116] TJ Nijdam and W. G. Sloof. "Modelling of composition and phase changes in multiphase alloys due to growth of an oxide layer". In: *Acta Materialia* 56.18 (2008), pp. 4972–4983.

[117] Y Niu and F Gesmundo. "An approximate analysis of the external oxidation of ternary alloys forming insoluble oxides. I: High oxidant pressures". In: *Oxidation of Metals* 56.5 (2001), pp. 517–536.

[118] Jean Paidassi. "Contribution to the study of the oxidation of iron in air in the range 700-1250° C". In: *Revue de métallurgie* 54.8 (1957), pp. 569–585.

[119] JONG-HEE PARK, Wayne E King, and STEVEN J ROTHMAN. "Cation Tracer Diffusion in Cr2O3 and Cr2O3-0.09 wt% Y2O3". In: *Journal of the American Ceramic Society* 70.12 (1987), pp. 880–885.

[120] Karl Pearson and Alice Lee. "On the laws of inheritance in man: I. Inheritance of physical characters". In: *Biometrika* 2.4 (1903), pp. 357–462.

[121] Fabian Pedregosa et al. "Scikit-learn: Machine learning in Python". In: *the Journal of machine Learning research* 12 (2011), pp. 2825–2830.

[122] Jian Peng et al. "Data analytics approach to predict high-temperature cyclic oxidation kinetics of NiCr-based Alloys". In: *npj Materials Degradation* 5.1 (2021), p. 41.

[123] F Pettit, R Yinger, and JB Wagner Jr. "The mechanism of oxidation of iron in carbon monoxide-carbon dioxide mixtures". In: *Acta Metallurgica* 8.9 (1960), pp. 617–623.

[124] FS Pettit and JB Wagner Jr. "Transition from the linear to the parabolic rate law during the oxidation of iron to wüstite in CO-CO2 mixtures". In: *Acta Metallurgica* 12.1 (1964), pp. 35–40.

[125] R Pillai et al. "Computational methods to accelerate development of corrosion resistant coatings for industrial gas turbines". In: *Superalloys 2020* (2020), pp. 824–833.

[126] Rishi Pillai, Anton Chyrkin, and Willem Joseph Quadakkers. "Modeling in High-Temperature Corrosion: A Review and Outlook". In: *Oxidation of Metals* 96.5 (2021), pp. 385–436.

[127] Rishi Pillai et al. "A new computational approach for modelling the microstructural evolution and residual lifetime assessment of MCrAlY coatings". In: *Materials at High Temperatures* 32.1-2 (2015), pp. 57–67.

[128] Rishi Pillai et al. "Lessons learned in employing data analytics to predict oxidation kinetics and spallation behavior of high-temperature NiCr-based alloys". In: *Oxidation of Metals* 97.1-2 (2022), pp. 51–76.

[129] BA Pint, J Leibowitz, and JH DeVan. "The effect of an oxide dispersion on the critical Al content in Fe-Al alloys". In: *Oxidation of Metals* 51 (1999), pp. 181–197.

[130] David R Poirier and G Geiger. *Transport phenomena in materials processing*. Cham: Springer, 2016.

[131] Liudmila Prokhorenkova et al. "CatBoost: unbiased boosting with categorical features". In: *Advances in neural information processing systems* 31 (2018).

[132] J. Ross Quinlan. "Induction of decision trees". In: *Machine learning* 1 (1986), pp. 81–106.

[133] Rampi Ramprasad et al. "Machine learning in materials informatics: recent applications and prospects". In: *npj Computational Materials* 3.1 (2017), pp. 1–13.

[134] RA Rapp. "The transition from internal to external oxidation and the formation of interruption bands in silver-indium alloys". In: *Acta Metallurgica* 9.8 (1961), pp. 730–741.

[135] Indranil Roy, Pratik K Ray, and Ganesh Balasubramanian. "Examining oxidation in β-NiAl and β-NiAl+ Hf alloys by stochastic cellular automata simulations". In: *npj Materials Degradation* 5.1 (2021), p. 55.

[136] Antônio Claret Soares Sabioni et al. "Ion diffusion study in the oxide layers due to oxidation of AISI 439 ferritic stainless steel". In: *Oxidation of Metals* 81.3 (2014), pp. 407–419.

[137] K Sachs and CW Tuck. "Scale Growth during Re-heating Cycles". In: *Materials and Corrosion* 21.11 (1970), pp. 945–954.

[138] Norbert G Schmahl, Hans Baumann, and Hermann Schenck. "The temperature dependence of the scaling of pure iron in oxygen". In: *Archive for the ironworks* 29.2 (1958), pp. 83–88.

[139] Jonathan Schmidt et al. "Recent advances and applications of machine learning in solid-state materials science". In: *npj Computational Materials* 5.1 (2019), pp. 1–36.

[140] Quanqiang Shi et al. "High temperature oxidation behavior of SIMP steel". In: *Oxidation of Metals* 83.5 (2015), pp. 521–532.

[141] Kozo Shinoda, Takamichi Yamamoto, and Shigeru Suzuki. "Characterization of selective oxidation of manganese in surface layers of Fe-Mn alloys by different analytical methods". In: *ISIJ international* 53.11 (2013), pp. 2000–2006.

[142] WW Smeltzer. "The kinetics of wustite scale formation on iron". In: *Acta Metallurgica* 8.6 (1960), pp. 377–383.

[143] WW Smeltzer, RR Haering, and JS Kirkaldy. "Oxidation of metals by short circuit and lattice diffusion of oxygen". In: *Acta Metallurgica* 9.9 (1961), pp. 880–885.

[144] James L Smialek et al. *Oxygen permeability and grain-boundary diffusion applied to alumina scales*. Tech. rep. 2013.

[145] HG Sockel, B Saal, and M Heilmaier. "Determination of the grain boundary diffusion coefficient of oxygen in Cr2O3". In: *Surface and Interface Analysis* 12.10 (1988), pp. 531–533.

[146] GM Song et al. "Relation between microstructure and adhesion of hot dip galvanized zinc coatings on dual phase steel". In: *Acta Materialia* 60.6-7 (2012), pp. 2973–2981.

[147] Roberto Spotorno. "High-Temperature oxidation of AISI441 ferritic stainless steel for solid oxide fuel cells". In: *Materials Science Forum*. Vol. 1016. Trans Tech Publ. 2021, pp. 1381–1385.

[148] FH Stott, GC Wood, and J Stringer. "The influence of alloying elements on the development and maintenance of protective scales". In: *Oxidation of Metals* 44.1 (1995), pp. 113–145.

[149] Srinivasan Swaminathan and Michael Spiegel. "Thermodynamic and kinetic aspects on the selective surface oxidation of binary, ternary and quarternary model alloys". In: *Applied Surface Science* 253.10 (2007), pp. 4607–4619.

[150] Belma Talic et al. "Comparison of MnCo2O4 coated Crofer 22 H, 441, 430 as interconnects for intermediate-temperature solid oxide fuel cell stacks". In: *Journal of Alloys and Compounds* 821 (2020), p. 153229.

[151] Belma Talic et al. "Effect of coating density on oxidation resistance and Cr vaporization from solid oxide fuel cell interconnects". In: *Journal of Power Sources* 354 (2017), pp. 57–67.

[152] G Tammann. "Tempering Colors of Metals". In: *Z. Anorg. Allg. Chem.* 111 (1920), pp. 78–90.

[153] Christopher D Taylor and Brett M Tossey. "High temperature oxidation of corrosion resistant alloys from machine learning". In: *npj Materials Degradation* 5.1 (2021), p. 38.

[154] Ljupčo Todorovski, Peter Ljubič, and Sašo Džeroski. "Inducing polynomial equations for regression". In: *Machine Learning: ECML 2004: 15th European Conference on Machine Learning, Pisa, Italy, September 20-24, 2004. Proceedings 15*. Springer. 2004, pp. 441–452.

[155] P Tomaszewicz and GR Wallwork. "Iron–Aluminum alloys: a review of their oxidation behavior". In: *Rev. High-Temp. Mater.* 4.1 (1978), pp. 75–105.

[156] CW Tuck, M Odgers, and K Sachs. "The oxidation of iron at 950 C in oxygen/water vapour mixtures". In: *Corrosion Science* 9.4 (1969), pp. 271–285.

[157] X Vanden Eynde, J-P Servais, and M Lamberigts. "Thermochemical surface treatment of iron-silicon and iron-manganese alloys". In: *Surface and Interface Analysis* 33.4 (2002), pp. 322–329.

[158] JA Von Fraunhofer and GA Pickup. "The oxidation behaviour of low alloy steels—Part1". In: *Anti-Corrosion Methods and Materials* (1970).

[159] Masashi Wada, Tsuneaki Matsudaira, and Satoshi Kitaoka. "Mutual grain-boundary transport of aluminum and oxygen in polycrystalline Al2O3 under oxygen potential gradients at high temperatures". In: *Journal of the Ceramic Society of Japan* 119.1395 (2011), pp. 832–839.

[160] C Wagner. "Reaction types in the oxidation of alloys". In: *Z. Elektrochem.* 63 (1959), pp. 772–782.

[161] Carl Wagner. "Equations for transport in solid oxides and sulfides of transition metals". In: *Progress in solid state chemistry* 10 (1975), pp. 3–16.

[162] Carl Wagner. "Reaktionstypen bei der Oxydation von Legierungen". In: *Zeitschrift für Elektrochemie, Berichte der Bunsengesellschaft für physikalische Chemie* 63.7 (1959), pp. 772–782.

[163] Carl Wagner. "The distribution of cations in metal oxide and metal sulphide solid solutions formed during the oxidation of alloys". In: *Corrosion Science* 9.2 (1969), pp. 91–109.

[164] Carl Wagner. "Theoretical analysis of the diffusion processes determining the oxidation rate of alloys". In: *Journal of The Electrochemical Society* 99.10 (1952), p. 369.

[165] GR Wallwork. "The oxidation of alloys". In: *Reports on Progress in Physics* 39.5 (1976), p. 401.

[166] Ge Wang, B Gleeson, and DL Douglass. "An extension of Wagner's analysis of competing scale formation". In: *Oxidation of Metals* 35.3-4 (1991), pp. 317–332.

[167] Ge Wang, B Gleeson, and DL Douglass. "Phenomenological treatment of multilayer growth". In: *Oxidation of metals* 31 (1989), pp. 415–429.

[168] Jian Wang et al. "The influence of temperature on the oxidation mechanism in air of HR3C and aluminum-containing 22Cr-25Ni austenitic stainless steels". In: *Oxidation of Metals* 89.5 (2018), pp. 713–730.

[169] Rosie Wang, Mark J Straszheim, and Robert A Rapp. "A high-temperature oxidation-resistant Fe-Mn-Al-Ni-Si alloy". In: *Oxidation of Metals* 21.1 (1984), pp. 71–79.

[170] DP Whittle et al. "Compositional changes in the underlying alloy during the protective oxidation of alloys". In: *Acta Metallurgica* 15.9 (1967), pp. 1421–1430.

[171] Patrik Wikström, Wlodzimierz Blasiak, and SC Du. "A study on oxide scale formation of low carbon steel using thermo gravimetric technique". In: *Ironmaking & Steelmaking* 35.8 (2008), pp. 621–632.

[172] PR Wilson and Zhixin Chen. "The effect of manganese and chromium on surface oxidation products formed during batch annealing of low carbon steel strip". In: *Corrosion Science* 49.3 (2007), pp. 1305–1320.

[173] GC Wood, IG Wright, T Hodgkiss, et al. "Oxidation rates of M-Cr alloys in pure O 2 at 1000 C". In: *Werkst u Korros* 21 (1970), p. 700.

[174] *World Steel in Figures 2022*. https://worldsteel.org/steel-topics/statistics/world-steel-in-figures-2022/. 2022.

[175] GL Wulf, MB McGirr, and GR Wallwork. "Theoretical analysis of alloy oxidation with reference to FeCr alloys". In: *Corrosion Science* 9.10 (1969), pp. 739–754.

[176] Chunhua Xu and Wei Gao. "Pilling-Bedworth ratio for oxidation of alloys". In: *Materials Research Innovations* 3.4 (2000), pp. 231–235.

[177] Yulai Xu et al. "Improved oxidation resistance of 15 wt.% Cr ferritic stainless steels containing 0.08-2.45 wt.% Al at 1000°C in air". In: *Corrosion Science* 100 (2015), pp. 311–321.

[178] H Yin et al. "Temperature Effects on the Oxidation of Low Carbon Steel in N_2-H_2-H_2O at $800-1200$°C". In: *Oxidation of Metals* 77.5 (2012), pp. 305–323.

[179] Suzue Yoneda et al. "Effect of Mn on Isothermal Transformation of Thermally Grown FeO Scale Formed on Fe–Mn Alloys". In: *Oxidation of Metals* 87.1-2 (2017), pp. 125–138.

[180] David J Young and Huaying Yin. "Water vapour effects on FeO scale growth: differences between iron and steel". In: *Oxidation of metals* 79.5-6 (2013), pp. 445–460.

[181] David John Young. *High temperature oxidation and corrosion of metals*. Vol. 1. Elsevier, 2008.

[182] DJ Young, F Viani, and F Gesmundo. "Parabolic growth of solid-solution scales: Effect of deviations from stoichiometry". In: *Oxidation of Metals* 30.5 (1988), pp. 391–403.

[183] Juntao Yuan et al. "Comparison between the oxidation of iron in oxygen and in steam at 650–750 C". In: *Corrosion Science* 75 (2013), pp. 309–317.

[184] Kang Yuan et al. "MCrAlY coating design based on oxidation-diffusion modelling. Part I: Microstructural evolution". In: *Surface and Coatings Technology* 254 (2014), pp. 79–96.

[185] Dae Won Yun et al. "Modelling high temperature oxidation behaviour of Ni-Cr-W-Mo alloys with Bayesian neural network". In: *Journal of alloys and compounds* 587 (2014), pp. 105–112.

[186] Jung-Yeul Yun et al. "Oxidation behavior of low carbon steel at elevated temperature in oxygen and water vapor". In: *steel research international* 84.12 (2013), pp. 1252–1257.

[187] Gregory J Yurek, John P Hirth, and Robert A Rapp. "The formation of two-phase layered scales on pure metals". In: *Oxidation of Metals* 8.5 (1974), pp. 265–281.

[188] Yingbo Zhang et al. "Influences of Si content on the high-temperature oxidation behavior of X10CrAlSi18 ferritic heat-resistant stainless steel at 700°C and 800°C". In: *Surface and Coatings Technology* 422 (2021), p. 127.

[189] Tao Zheng and Jing Tao Han. "High temperature oxidation behavior of SUS310S austenitic stainless steel". In: *Advanced Materials Research*. Vol. 941. Trans Tech Publ. 2014, pp. 212–215.

[190] Gordon E Zima. *Some high temperature oxidation characteristics of nickel with chromium additions*. Tech. rep. CALIFORNIA INST OF TECH PASADENA DYNAMIC PROPERTIES LAB, 1956.

[191] Dening Zou et al. "High temperature oxidation behavior of a high Al-containing ferritic heat-resistant stainless steel". In: *Materials Characterization* 136 (2018), pp. 435–443.

A

Appendix A

To show the consumption rate of oxygen in the high-temperature oxidation experiments of this work, a series of calculations are conducted (Equation (A.1) and Equation (A.2)).

$$Supply\ rate\ of\ oxygen\ (mol\ O_2/s) = \frac{Flow\ rate\ (ml/s) \times p_{O_2}(atm)}{22.4 \times 1000} \quad (A.1)$$

$$Consumption\ rate\ of\ oxygen\ (mol\ O_2/s) = \frac{k_l\left(g.cm^{-2}.s^{-1}\right) \times A\left(cm^2\right)}{M_{O_2}(g.mol^{-1})} \quad (A.2)$$

The supply and consumption rates are calculated in moles per second and are shown in Table 3.1.

Table A.1: The calculated amount of oxygen supplied and consumed for the experiments in this work.

Flow rate (ml/min)	p_{O_2} (atm)	k_l ($gcm^{-2}s^{-1}$)	Supplied oxygen (mol/s)	Consumed oxygen (mol/s)
26.6	0.1	6.88×10^{-6}	1.98×10^{-6}	7.14×10^{-7}
26.6	0.15	1.01×10^{-5}	2.97×10^{-6}	1.00×10^{-6}
26.6	0.2	1.37×10^{-5}	3.96×10^{-6}	1.42×10^{-6}
26.6	0.25	1.74×10^{-5}	4.95×10^{-6}	1.81×10^{-6}
26.6	0.3	2.14×10^{-5}	5.94×10^{-6}	2.22×10^{-6}
53.3	0.1	1.34×10^{-5}	3.97×10^{-6}	1.39×10^{-6}
53.3	0.15	2.06×10^{-5}	5.95×10^{-6}	2.14×10^{-6}
53.3	0.2	2.72×10^{-5}	7.93×10^{-6}	2.82×10^{-6}
53.3	0.25	3.39×10^{-5}	9.91×10^{-6}	3.52×10^{-6}
53.3	0.3	4.02×10^{-5}	1.19×10^{-5}	4.17×10^{-6}

Figure A.1 shows the supply and consumption of oxygen in each experiment.

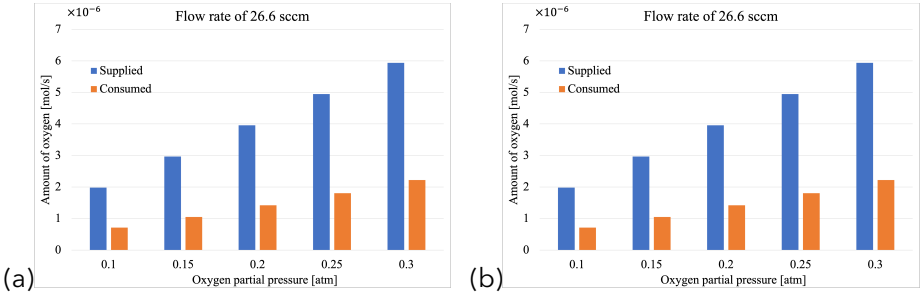

Figure A.1: The calculated supply and consumption of oxygen for the high-temperature oxidation experiments with two flow rates of (a) 26.6 sccm, and (b) 53.3 sccm.

Table A.2: Relevant parameters for calculation of the linear rate constant for oxidation of the iron-manganese alloys in binary O_2-N_2 gas mixtures with a linear flow rate of 53.3 sccm and oxygen partial pressure of 20 kPa at various temperatures.

Temperature (°C)	950	1000	1050	1100	1150
kT/ε_{N_2}	13.366	13.913	14.459	15.005	15.552
Ω_{N_2}	0.797	0.792	0.788	0.784	0.779
η_{N_2} ($gcm^{-1}s^{-1}$)	4.30×10^{-4}	4.41×10^{-4}	4.52×10^{-4}	4.63×10^{-4}	4.74×10^{-4}
ρ_{N_2} (gcm^{-3})	2.79×10^{-4}	2.68×10^{-4}	2.58×10^{-4}	2.48×10^{-4}	2.40×10^{-4}
ν_{N_2} (cm^2s^{-1})	1.541	1.646	1.754	1.864	1.978
kT/ε_{O_2}	10.823	11.265	11.708	12.150	12.593
Ω_{O2}	0.818	0.814	0.810	0.807	0.803
η_{O_2} ($gcm^{-1}s^{-1}$)	5.38×10^{-4}	5.51×10^{-4}	5.64×10^{-4}	5.77×10^{-4}	5.90×10^{-4}
ρ_{O_2} (gcm^{-3})	3.19×10^{-4}	3.06×10^{-4}	2.95×10^{-4}	2.84×10^{-4}	2.74×10^{-4}
ν_{O_2} (cm^2s^{-1})	1.687	1.799	1.914	2.033	2.155
$kT/\varepsilon_{N_2-O_2}$	12.027	12.519	13.011	13.502	13.995
$\Omega_{N_2-O_2}$	0.808	0.804	0.800	0.796	0.792
$\eta_{N_2-O_2}$ ($gcm^{-1}s^{-1}$)	4.52×10^{-4}	4.64×10^{-4}	4.76×10^{-4}	4.87×10^{-4}	4.99×10^{-4}
$\rho_{N_2-O_2}$ (gcm^{-3})	2.87×10^{-4}	2.86×10^{-4}	2.65×10^{-4}	2.56×10^{-4}	2.46×10^{-4}
$\nu_{N_2-O_2}$ (cm^2s^{-1})	1.578	1.684	1.794	1.907	2.023
D_{O_2} (cm^2s^{-1})	2.452	2.630	2.813	3.002	3.196

B

Appendix B

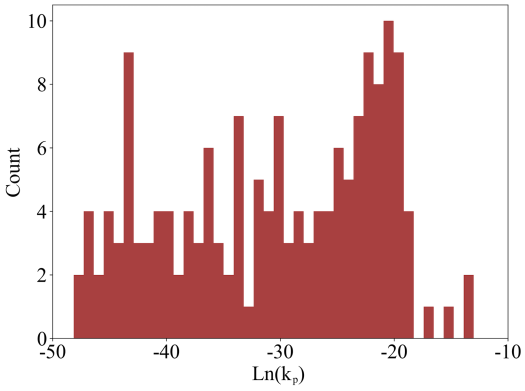

Figure B.1: The distribution of k_p values in the dataset.

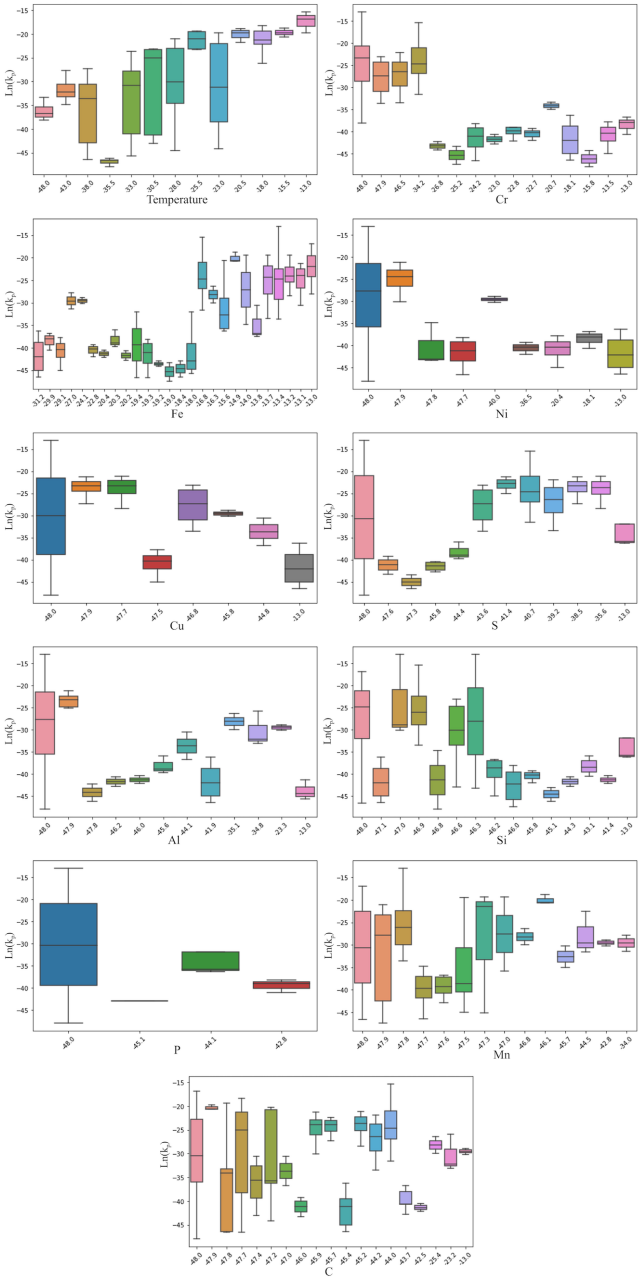

Figure B.2: The distribution of the dataset for all the features. The X axes show the normalized values.

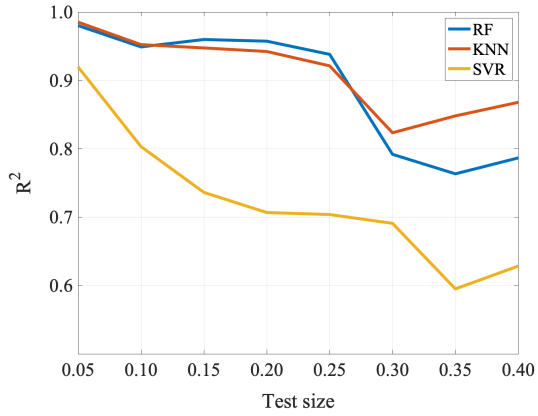

Figure B.3: The R-squared error for RF, KNN, and SVR models as a function of the size of the test dataset. The models are trained with the remaining portion of the data which is the training dataset.

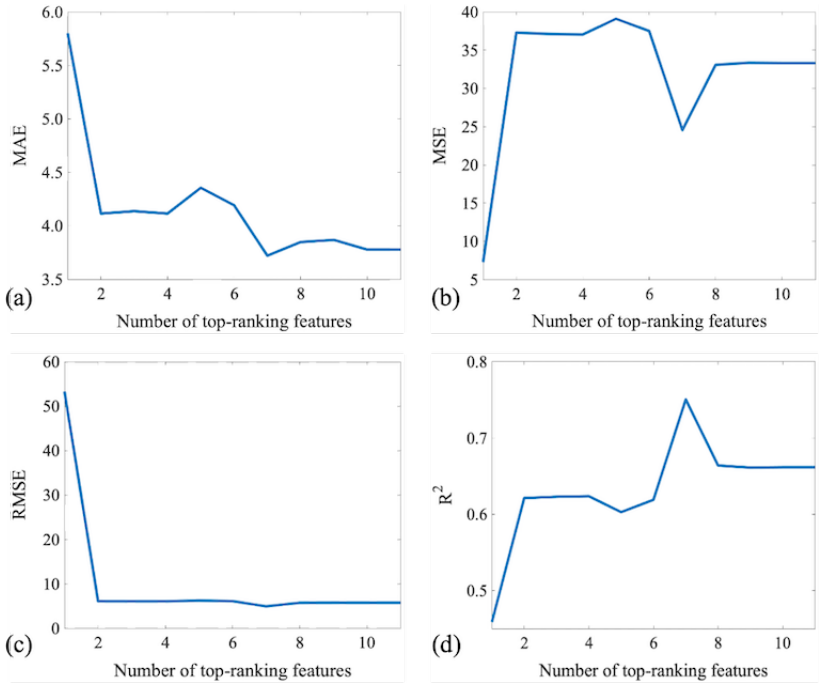

Figure B.4: The performance of the LR model as a function of the number of top-ranking features evaluated by (a) MAE, (b) MSE, (c) RMSE, and (d) R-squared indices.

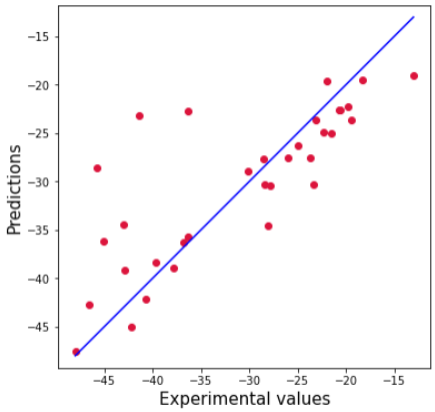

Figure B.5: Actual values of experimental parabolic growth rate constants of high-temperature oxidation compared with values obtained from the LR model where it was trained with four top-ranking features and tested with 20% of the dataset (32 red dots).

Acknowledgements

I would like to express my gratitude to **Dr. Amarante Böttger** for her guidance throughout this research period. My sincere thanks go to **Prof.dr.ir. Arjan Mol**, my co-promotor, for his support. I also wish to convey my deep appreciation to **Dr.ir. Wim Sloof**, my former promotor, who generously provided assistance and guidance despite his retirement during my PhD. Special thanks to **Hans Brouwer**, from the high-temperature lab, for his invaluable assistance with my experiments. Additionally, I am thankful to **Ruud Hendrikx** and **Richard Huizenga** for their consistent support with my measurements.

I express my gratitude to **Prof.dr.ir. Jilt Sietsma** for accepting the invitation to join my defense committee. Your participation as a committee member is a great honor for me. I extend my sincere thanks to the distinguished members of my PhD defense committee, **Prof.dr.ir. Rinze Benedictus**, **Prof.dr.ir. Bart Kooi**, **Dr. Michael Auinger**, **Dr. Wanda Melfo**, and **Prof.dr. Maria Santofimia Navarro**, for agreeing to be a part of my defense, reading my thesis and helping me improve it.

I was fortunate to share a workspace with a group of friendly researchers during my PhD. Gratitude goes to **Vibhor**, **Jan**, **Arthur**, **Pablo**, **Xiaohui**, **Jaji**, **Gaojie**, **Keer**, **Prasaanth**, **Prasad** and **Zhaoying**. Special appreciation is extended to the Iranian community at MSE, including **Mohsen**, **Behnam**, **Nilgoon**, **Farnaz**, **Peyman**, **Sajjad**, **Ali K**, **Khatereh**, **Ehsan**, **Arash**, and **Amin**. Your presence made it feel a bit closer to home.

I would also like to express my gratitude to my fantastic new colleagues at the SDE department. **Prof.dr. Ruud Balkenende** and **Prof.dr.ir. Conny Bakker**, thanks for your trust and support. My creative artist colleagues, **Dorien** and **Tekla**, thanks for the great help with the cover design. And a big thank to **Jullieta**, **Nik**, **Jelle**, and **Vibhash** for making work enjoyable.

Kaveh, your welcoming smile and genuine kindness always motivated me to visit you for a chat. Thank you, and I hope you enjoy the rest of your journey with **Sara**. **Amir Hossein** and **Reihaneh**, I am sincerely grateful for your genuine warmth, and it consistently brings joy to spend time with both of you. Thank you, and may the future bring nothing but the finest experiences and successes into your lives.

When reflecting on the first days of my life in the Netherlands, two names immediately come to mind: **Nima** and **Delaram**, the lovely couple who warmly supported me since my first day in Delft. **Nima**, I consider myself fortunate to have had you in the neighboring department, allowing me to approach you with my random questions anytime. Thank you for everything! Through you, I also forged several delightful friendships. **Farshid**, **Ali Amooz**, **Saleh**, **Hesam**, **Saman**, and **Ahmad**, every moment we spent together and the countless coffees we shared,

discussing our typically conflicting opinions about different matters, are treasured memories. Thank you all for making our small gatherings so engaging.

Beyond the network I established in Delft, residing in Rotterdam for a year allowed me to cultivate remarkable friendships. **Negin**, I believe getting to know you was a pivotal moment in my life, and I am truly thankful for all your support and kindness. To **Kaveh**, **Mahdi**, **Yasaman**, **Ata**, **Hamideh**, **Gijs**, and **Paniz**, spending time with all of you has been a pleasure. I wish nothing but the best for each of you. I miss our shared moments. Moreover, I discovered an incredible circle of friends in Zoetermeer. **Tino**, **Amir**, **Pouya**, and **Emad**, I appreciate being a part of this group. Thank you all! Spending time with you has added color to my life in Zoetermeer.

I am deeply grateful for my old friendships. To **Abuzar**, **Mostafa**, **Moein**, **Hamid**, and **Sadra**, I have known you since as long as I can remember, and I can write a whole book about our friendship including all those near-death experiences that **Abuzar** made for all of us. I am waiting for the next time we explore the amazing nature around Shahrood together! To **Elham** and **Amir J**, thank you too for adding charm to my life in Shahrood. I eagerly look forward to hanging out with you both again. **Milad** and **Mahsa**, not being able to see you regularly was one of my primary concerns when leaving the country. Wishing you both an abundance of happiness as you welcome your baby (my lovely God-daughter)!

During my bachelor studies in Mashhad, Iran, I met two legends, **Hossein G** and **Armin**. Honestly, if it were not for you guys, I would probably still be deciphering my first-year syllabus. Thank you for all the support and motivation you provided. **Shima**, your warm vibes made you a wonderful addition to our small circle of friends. I wish you all the best in your life with **Hossein**. **Armin**, here I had some space to mention your partner's name, but his/her/their existence is still unclear.

The first thing I started missing after leaving MSE, was not the high-tech equipment or groundbreaking research - it was our lunches and coffee breaks with the PhD squad. **Elsa**, **Gautham**, **Philipp**, **Joep**, **Tim**, **Mohammed**, **Hussein F**, **Luís**, **Camila**, **Can**, **Jose**, **Jasper**, **Gesa**, and **Alfonso** thank you for turning those breaks into the highlights of my MSE life. You guys made it more than just caffeine and calories; you made it an experience. I also had micro-breaks within the office with the MVP for turning work into a comedy show: **Daniel**. No wonder I only finished my thesis after escaping that office. I miss sharing the office with you, amigo! Next, hats off to the MSE veteran, our Greek goddess of chaos, after meeting whom, I learned why our ancestors had years of Greco-Persian wars! Thank you, **Konstantina**, for having such a welcoming spirit and -surprisingly- wise pieces of advice for me. I only wish I could access your settings and adjust your speed to x0.75.

PhD life is usually isolated, but the friendly group of fellow PhDs I had around me made my life much easier. **Jithin** and **Jhon**, thank you for all the fun times during and after work. Doing sports, BBQ, King's Days, and partying was way more enjoyable with you guys around. We should also thank the noisy Brazilian girl who made all these moments happen. **Vitória**, you have proven that having a

little sister remains annoying, even though she was born 12,000 kilometers away from me. I miss the moments when you used to enter our office with a muffin in your hand, tears in your eyes, and share your non-stop complaints about work. Working is not the same without you. **Marco**, I am thankful for your presence in this group as well. Otherwise, it would be very difficult for me to be surrounded only by smart people of MSE! Thank you for providing me with good help whenever I needed it. I truly appreciate your persistence in life, which is reflected in the football teams you support.

Mohamad Reza, thank you for making life more real when you are around. What you taught me is beyond anything I picked up in my not-so-brief academic journey. Our friendship feels like reading a never-ending interesting book. I am forever thankful for what you have shared, and though I will not say I miss you (because your wisdom sticks with me), I do miss hearing you. It was always on point, and I never had to question the content!

Apart from the numerous friendships I formed, I was also lucky to discover a family here in Europe. **Ferenc** and **Krisztina**, your kind hearts made me feel as if I had a second set of parents just as wonderful as the first ones. Additionally, it allowed me to meet a Gen Z Bayern Munich fan. A heartfelt thank you to **Zita** for your invaluable live translations and for bringing joy to any setting you are placed in.

This Persian paragraph is for my beloved family in Iran:

می‌خواهم از خانواده‌ی عزیزم به خاطر همه‌ی حمایت‌هاشون در این سی و اندی سال تشکر کنم. ستاره، سعید و سارای عزیز، به دنیا اومدن توی این خانواده و داشتن برادر خواهرهایی مثل شما شانسیه که بابت داشتنش خدارو شکر می‌کنم. ازتون ممنونم بابت تک‌تک از خود گذشتگی‌هایی که برای داداش کوچیکتون کردید. مامان و بابای نازنینم، مرسی که در کنار همدیگه، هم راه عشق ورزیدن و هم تعقّل رو بهم نشون دادید تا امروز حس کنم هر دو بال عشق و عقل رو در کنار هم دارم. ساسان عزیز، ازت ممنونم که به عنوان جدیدترین عضو خونواده، همیشه همراه و همدل کنارمون بودی. پارسای نازنین، بابت همه‌ی چیزهایی که لابلای سوال‌هات بهم یاد دادی ازت تشکر می‌کنم و دوست دارم که بدونی از صمیم قلب به قلب بزرگی که داری افتخار می‌کنم و بی‌صبرانه منتظر دورانی هستم که بتونیم توی دنیای مادی هم نزدیک به همدیگه زندگی کنیم.

Lastly, I want to thank **Eszter**. Meeting you has given meaning to everything I have experienced in the last 5 years. Envisioning a scenario in my life that could bring more happiness is now incredibly challenging, thanks to you. Your extraordinary flexibility and patience have amazed me, making it effortless to love you. My sole wish for our future is to continue having love for each other and everyone around us in every moment.

I want to finish with a piece of poem from **Rumi**, which wraps up what I gained from my years of being in academia:

عقل خود را می‌نماید رنگ‌ها چون پری دورست از آن فرسنگ‌ها
از مَلَک بالاست چه جایِ پری؟ تو مگس پرّی به پستی می‌پری
گر چه عقلت سویِ بالا می پرد مرغ تقلیدت به پستی می‌چرد
علمِ تقلیدی وبال جان ماست عاریه ست و ما نشسته کآنِ ماست
زین خِرَد جاهل همی باید شدن دست در دیوانگی باید زدن
هر چه بینی سود خود، زآن می گریز زهر نوش و آبِ حیوان را بریز
هر که بستاید تو را دشنام دِه سود و سرمایه به مُفلس وام ده
ایمنی بگذار و جایِ خوف باش بگذر از ناموس و رسوا باش و فاش

آزمودم عقل دوراندیش را بعد از این دیوانه سازم خویش را

Soroush Aghaeian
Delft, February 2024

List of Publications

Journal papers

1. **S. Aghaeian**, W.G. Sloof, J.M.C. Mol, and A.J. Böttger. "Initial High-Temperature Oxidation Behavior of Fe–Mn Binaries in Air: The Kinetics and Mechanism of Oxidation." Oxidation of Metals, 2022, vol 98, 1-2, pp. 217-237;

2. **S. Aghaeian**, J.C. Brouwer, W.G. Sloof, J.M.C. Mol, and A.J. Böttger. "Numerical Model For Short-Time High-Temperature Isothermal Oxidation of Fe–Mn Binaries at High Oxygen Partial Pressure." High Temperature Corrosion of Materials, 2023, vol 99, 3-4, pp. 201-218.

3. **S. Aghaeian**, F. Nourouzi, W.G. Sloof, J.M.C. Mol, and A.J. Böttger. "Predicting the parabolic growth rate constant for high-temperature oxidation of steels using machine learning models." Corrosion Science, p.111309.

4. **S. Aghaeian**, W.G. Sloof, J.M.C. Mol, and A.J. Böttger. "A Review on Kinetic Models for High-Temperature Oxidation of Iron, Iron-based Alloys, and Steels." In preparation.

Conference papers

1. **S. Aghaeian**, W. Melfo, W.G. Sloof, A.J. Böttger. "Kinetics of Oxide Scale Formation in Short Time on Pure Iron in CO_2+CO or H_2O+H_2 Gas Mixture." 12th International Conference on Zinc and Zinc Alloy Coated Steel Sheet (GALVATECH), 2021, pp. 1225-1235;

2. **S. Aghaeian**, W.G. Sloof, J.M.C. Mol, A.J. Böttger. "Initial High-Temperature Oxidation Behavior of Iron Binary Alloys in Air." 241st ECS meeting, 2022;

3. **S. Aghaeian**, J.C. Brouwer, W.G. Sloof, J.M.C. Mol, A.J. Böttger. "Combining Experimental and Numerical Modeling Approaches for Predicting Short-Time High-Temperature Surface Oxidation Behavior of Iron Alloys." European Oxide Scale Conference (OXI), 2022.

Biography

Soroush AGHAEIAN

I was born in 1991 in Shahrood, Iran. I completed my primary and secondary education in the same city. In 2009, I was admitted to Ferdowsi University, Mashhad, through the national exam to do my Bachelor in Materials Engineering - Industrial Metallurgy. After completing my Bachelor's degree in Materials Engineering in 2014, I immediately started my Master's in Materials Engineering-Metals Extraction at Sharif University of Technology, Tehran, Iran. From 2019 to 2023, I have been working toward a Ph.D. in the field of oxidation kinetics in steels in the Department of Materials Science and Engineering at Delft University of Technology, the Netherlands. In May 2023, I joined the Department of Sustainable Design Engineering in the Faculty of Industrial Design Engineering at Delft University of Technology as a postdoc to work on next-generation circular design guidelines.